UNIVERSITY OF CALGARY

Application of Near-Surface Seismic Characterization to Sparsely Sampled Data Sets

by

Andrew John Mills

A THESIS

SUBMITTED TO THE FACULTY OF GRADUATE STUDIES

IN PARTIAL FULFILMENT OF THE REQUIREMENTS FOR THE

DEGREE OF MASTER OF SCIENCE

GRADUATE PROGRAM IN GEOLOGY AND GEOPHYSICS

CALGARY, ALBERTA

DECEMBER, 2017

Abstract

The unconsolidated, attenuative, relatively low velocity near surface layers of the Earth cause recording and imaging problems in seismic exploration surveys. Surface waves, recorded as ground roll, have propagated through these near surface layers, and therefore have been affected by these properties of interest. Multichannel analysis of surface waves, or MASW, uses these ground roll amplitudes and the dispersive character of surface waves to estimate near surface shear wave velocities. MASW techniques are applied in this study to synthetic and field data acquired at up to exploration survey scale, to estimate the near surface geometries and velocities. Two field datasets (from the Priddis thumper experiment and Hussar low frequency experiment) are interpolated and filtered to increase dispersion curve resolution. Least squares inversion is applied to the dispersion curve, and 1D near surface velocity profiles are estimated and combined to form 2D velocity profiles over the survey lines. The depth and shear wave velocity of near surface layers and bedrock is estimated to depths greater than 60 m.

Acknowledgements

I would like to thank my supervisor Dr. Kris Innanen for giving me the opportunity to work on this project, and for his guidance, suggestions, and supervision, I would like to also thank Laura Baird, Kevin Hall, and Kevin Bertram for their administrative and technical support throughout my studies.

I thank Dr. Raul Cova for his useful guidance and suggestions for beginning my research on these topics. Scott Keating deserves my gratitude for his assistance and instruction throughout my research.

I appreciate my fellow students, Bobby Gunning, Scott Keating, Eric Rops, Tyler Spackman, Adriana Gordon, Khalid Almuteri, Matt Eaid, Tim Cary, and all others for making my degree an enjoyable experience.

I would like to thank the industrial sponsors of CREWES, as well as NSERC, for their financial support of the consortium, and of this project.

Finally, I thank my family for their support during my education.

Table of Contents

List of Tables

List of Figures and Illustrations

List of Symbols, Abbreviations and Nomenclature

Symbol	Definition
β	Damping factor
C	Velocity
$\boldsymbol{d}_{obs}$	Observed dispersion curve
$\boldsymbol{d}_{syn}$	Synthetic modelled dispersion curve
$\boldsymbol{\delta}$	Parameter change vector
$\boldsymbol{\delta}_{\mathbf{R}}$	Regularized parameter change vector
$\mathbf{e}$	Error or residual
f	Frequency
$\mathbf{g}$	Discrepancy vector
H	Layer thickness
$\mathbf{I}$	Identity matrix
$\mathbf{J}$	Jacobian matrix
λ	Wavelength
n	Layer number
p	Slowness
Φ	Objective function
ρ	Density
R	Regularization
S	Cumulative squared error
$\boldsymbol{\theta}$	Model parameter vector
t	Time
τ	Tau intercept time
v	Velocity
V_s	Shear wave velocity
V_r	Rayleigh wave velocity
ω	Spatial frequency
x	Surface position
Δx	Receiver spacing
z	Depth
AGC	Automatic gain correction
DAS	Distributed Acoustic Sensing
FWI	Full Waveform Inversion
LNMO	Linear Normal Moveout
MASW	Multi-channel Analysis of Surface Waves
SASW	Spectral Analysis of Surface Waves
SP	Source point
VSP	Vertical seismic profile
3C	Three Component

Chapter One: Introduction

1.1 The near surface

In land seismic exploration, where both source and receiver are located at the surface of the Earth, all seismic energy must travel through the near surface layers, whether thereafter going into deeper layers of interest, or going directly from source to receiver along the surface of the Earth. A large part of the recorded energy is from the latter, seismic surface waves travelling with high amplitude, over relatively short distances compared to the former. The near surface of the earth is often not a single cohesive, homogeneous rock layer, but a mixture of rock types and geometries, with different properties affecting the propagation of seismic energy. The near surface begins at the surface of the Earth, or the free surface, and continues until the bedrock is reached, which is a package of higher velocity, consolidated sedimentary and crystalline rocks (Yilmaz, 2015). Within the near surface layer(s), the materials are composed of low velocity, unconsolidated, heterogeneous and incohesive fine-grained soils, silts, clays, and sands, as well as coarser grained gravels and glacial till. Surface waves are primarily influenced by the properties of these near surface materials, and can thus be used to deduce information about these layers.

The near surface poses challenges for exploration seismology, as it is highly attenuative to seismic signals, which are made up of body wave (P- and S- waves) energy. Since body waves must travel through this layer at least twice, typically at different locations which contain unique near surface conditions, seismic recordings can be significantly and in a complex manner influenced by its properties.

Land seismic acquisition and processing technology requires methods for dealing with the near surface, as it is not physically or financially feasible to bury all source and receiver points below the unconsolidated near surface. Near surface effects are dealt with in data processing, usually by performing statics corrections (Yilmaz, 2001). This can be accomplished with refraction statics, which use refracted arrivals associated with the base of the unconsolidated near surface. However, in elastic seismic data processing, which includes treatment of converted-wave seismic data, the problem of shear wave statics arises (Cova, 2017). Shear wave refraction arrivals cannot be used to compute the S-wave statics, as they are usually unavailable or unidentifiable in the data, unless a shear wave source is used. Additionally, due to the much slower S-wave near surface velocities, relatively larger statics corrections are required for the shear data (Cox, 1999). In other words, many of the assumptions underlying methods for dealing with the near surface are violated when the full elastic waveform is considered. This is an issue, because current research trends are suggestive that industry and academia are moving towards full waveform seismic methods (Virieux and Operto, 2009; Tarantola, 1986; Sears et al., 2008). Having accurate near surface shear wave velocity models is, therefore, important for characterizing amplitude, phase, and waveform aspects of seismic data, in addition to calculation of travel time delays through the near surface for shear waves. These models, once generated, can also be used for calculating P-wave traveltime delays, as the model geometry can be cross referenced with depths calculated from refraction data.

1.2 Surface waves

Seismic disturbances travelling along the surface of the Earth are called surface waves, which can arise when elastic solids (such as rock in the Earth) are bounded by a free surface (of air or water) (Yilmaz, 2015). These wave modes are easily detected by geophones and are referred to as ground roll. Commonly considered to be noise in exploration seismology, because they obscure reflection energy, surface waves are removed from seismic data and discarded. While inconvenient for reflection surveying, this apparent noise contains valuable information about the near surface (Nazarian et al., 1983). If this so-called noise can be used to characterize the near surface, additional value can be extracted from existing seismic data.

1.2.1 Rayleigh waves

At non-normal incidence at an interface, an incident compressional (P) wave is partitioned into four components; reflected P-wave and vertically polarized S-wave (SV-type), and transmitted P-wave and SV-type shear wave. When this partitioning occurs at the soil-bedrock interface, the P-P reflected and SV reflected waves become trapped in the soil column, and propagate along the free surface as horizontal planar waves with coupled P-SV particle motion (Yilmaz 2015). Surface waves of this type are known as Rayleigh waves. Rayleigh waves arise from the interference between compressional (P) waves and vertically polarized shear waves (SV) (Yilmaz, 2015), arising both from energy partitioning at the bedrock boundary, and in cases where the source generates both P and SV waves. Rayleigh waves propagate with retrograde elliptical particle motion, as shown in Figure 1-1. Particle motion can be seen to be in both the direction of and perpendicular to, the direction of wave propagation.

Due to the relative distances traveled, as well as the two-dimensional cylindrical character of surface waves compared to the three-dimensional spherical character of body waves (compressional and shear waves), recorded Rayleigh wave amplitudes are greater than body-wave amplitudes (Phillips et al., 2004). As can be seen in Figure 1-1, Rayleigh wave motion decreases with depth, which is dependent on the frequency of the waves. When a compressional wave source is used (e.g., dynamite, Vibroseis), more than two-thirds of total seismic energy generated takes the form of Rayleigh waves (Richart et al., 1970). This recorded ground roll appears in a "noise-cone" in shot records (Figure 1-2), which obscures the reflection energy that is of interest in most scenarios.

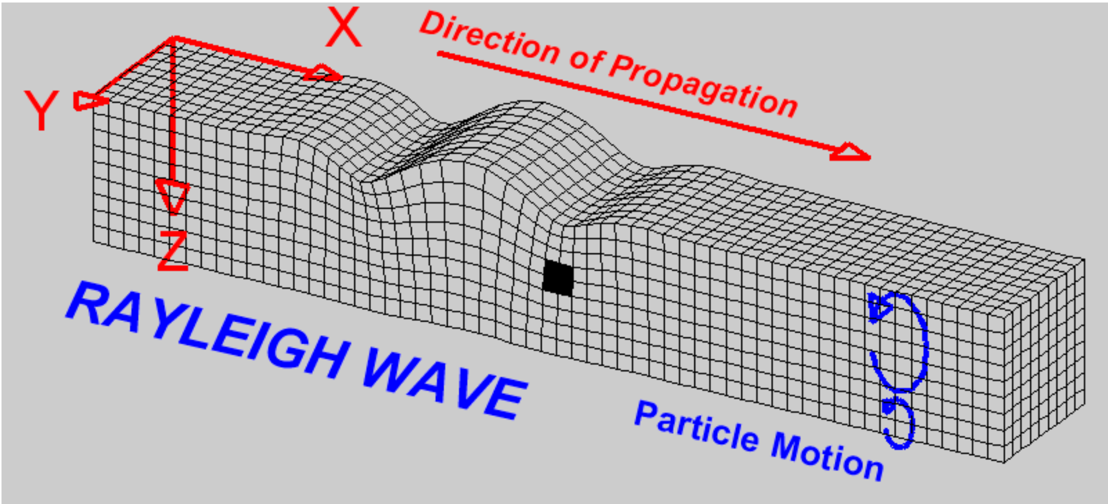

Figure 1-1 Rayleigh wave particle motion. Retrograde elliptical particle displacement, decreasing in amplitude with depth. (From http://web.ics.purdue.edu/~braile/edumod/waves/Rwave.htm).

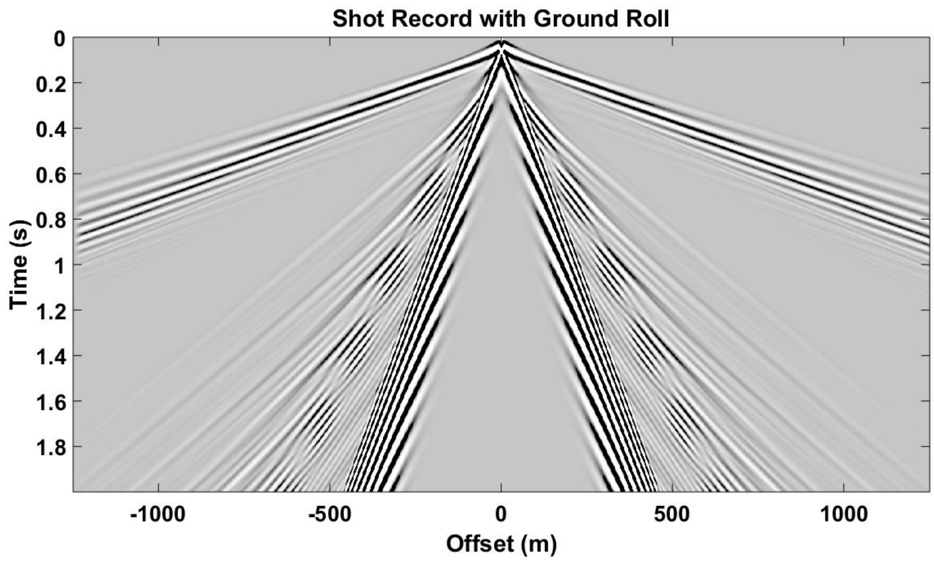

Figure 1-2 Shot record with a dominant ground roll noise cone.

Importantly for this study, Rayleigh waves are dispersive when travelling in layered media, meaning that each frequency component of the wave travels with a different phase velocity (Yilmaz, 2015). The dispersive properties of Rayleigh waves can be used to estimate shear wave velocities in the near surface (Nazarian et al., 1983; Stokoe et al., 1994; Park et al., 1998). This dispersion is visible in Figure 1-2, where discrete velocity dips are visible in the ground roll, indicating that the arrivals are travelling with different velocities.

1.2.2 Love waves

Love waves, which have a horizontally polarized shear (SH) type particle motion that is horizontal and transverse to the propagation direction, arise from an incident SH-wave being reflected as an SH wave which travels along the free surface (Yilmaz, 2015). These will not affect vertical component geophone recordings, and will not be considered in this thesis.

1.3 Near surface characterization

Currently, to support full-waveform inversion, which uses the full recorded wavefield to model the subsurface (Virieux and Operto, 2009), near surface attributes such as shear wave velocities, soil properties, and near surface geometries are usually assumed to either be known or to have negligible effect on the results, which must be expected to introduce inaccuracies into the results. The recorded body waves have travelled through the near surface at least twice, at different locations, and thus will have been affected by these materials and geometries (Mills et al., 2016; Mills and Innanen 2016a). Considering that a 2D seismic line or 3D seismic survey may cover many 10s or 100s of km^2 over varied terrain and environments, it is not reasonable to assume that the near surface layers of the earth have the same properties everywhere along these surveys.

Therefore, it is becoming increasingly important to know or at least approximate the near surface geometry and velocities. Through various near surface characterization methods, accurate velocity models can be estimated, which will lead to better shear statics corrections, and therefore better converted wave data. In addition, these models can be used to support P-wave statics corrections derived from refraction or other data.

Early methods of near surface characterization include spectral analysis of surface waves (SASW), introduced in the early 1980's as a method to generate the near surface v_s profile (Nazarian et al., 1983). SASW utilizes a single source and a single pair of receivers (single channel) whose separation is adjusted depending on the frequency and wavelength of surface wave to be measured. This requires many repeated shots at each survey location, altering the receiver spacing for each shot, in order to sample the frequency generated by the source. This increases acquisition time, and is necessary to recover data over the whole bandwidth of the surface waves.

Multichannel analysis of surface waves, or MASW, is a more recent advance, which uses a series of broadband geophones (similar to common midpoint (CMP) reflection surveys), with a source point at both ends of the array (Park et al., 1999). MASW is preferable over SASW because it allows all frequencies of surface waves to be measured simultaneously over a large area using a single shot. In MASW, a record is generated from the source at one end of the receiver line, and the repeated shot from the opposite end is used to confirm the results (Figure 1-3). This shot can also help detect lateral heterogeneities along the line by comparing the shot records, which would be identical for laterally homogeneous horizontally layered media.

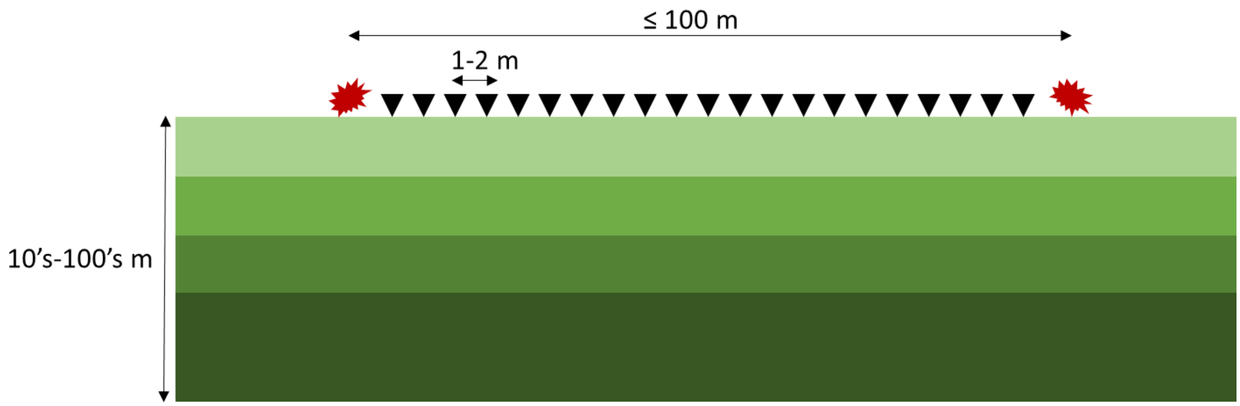

Figure 1-3 Typical field MASW acquisition.

Typical MASW surveys consist of relatively short receiver lines, usually under 100m long (Long and Donohue, 2007). Best results are achieved when receivers are deployed in closely spaced arrays, with 0.5m to 2m spacing typically (Long and Donohue, 2007). These parameters are favorable to recording planar Rayleigh waves, which become more difficult to record as receiver spacing and line length increases.

1.4 Applications of near surface characterization

Near surface characterization methods such as MASW are primarily used in geotechnical site evaluations (Yilmaz, 2015; Long and Donohue, 2007), to determine soil or sediment types and thicknesses. There are cases of using near surface characterization in monitoring applications, such as Dou et al. (2017). In that study, distributed acoustic sensing (DAS) is used to acquire near surface study data, using traffic noise as an ambient source. From the recorded DAS data, near surface shear-wave velocities are inverted for using interferometric and MASW techniques. The use of DAS to record ground roll is appealing because channel (receiver) spacing can be defined, thus limiting spatial aliasing from sparsely sampled data.

1.5 Software

Forward seismic modelling was conducted using Karlsruhe Institute of Technology's SOFI2D software. Data processing was done using Schlumberger's Vista, as well as MATLAB. Theoretical dispersion curves are calculated during the velocity inversion using MATLAB scripts mat_disperse.m and modal.m (Rix et al., 2003). Velocity inversion was performed in MATLAB, using original scripts.

1.6 Thesis objectives and overview

The main goal of this thesis is to propose, formulate, test, and apply a method to extract near surface velocity and geometry information from exploration scale seismic data. This work will apply multichannel analysis of surface waves (MASW) methods to data originally acquired for deeper subsurface exploration to produce near surface velocity profiles.

Chapter 2 covers the background of surface waves, and addresses the development, and state of the art in near surface characterization. The processing steps, including interpolation and dispersion measurement, required to apply these methods to non-ideal data, and the limitations of doing this are also covered.

Chapter 3 provides an overview of the forward and inverse modelling procedures and workflows used in this work. An important consideration in inversion, modelling error, is introduced.

Chapter 4 contains the first tests and validations of the above methods on synthetic data. Laterally homogeneous models are used to prove the 1D case, and laterally homogeneous models are used to extend the method's application to geological situations.

Chapter 5 is the first test of these methods on field seismic data, acquired at the University of Calgary's Priddis field test site. Data acquired over a 200 m long survey line using a thumper source, and recorded with non-ideal sampling, is processed using the previously developed workflow. 1D shear wave velocity profiles are inverted from the data, and used to build a 2D velocity profile over the survey line.

Chapter 6 is a second field data test, using the low frequency Hussar field data. Data was acquired using low frequency geophones, ideal for MASW surveys, and a low frequency vibrator source, with exploration scale receiver spacing. The data are processed using the developed workflow, and a 2D shear wave velocity profile is inverted for over a portion of the survey line.

Chapter 7 provides a summary of the work conducted in this thesis, and addresses further possible applications of these methods.

Chapter Two: Theoretical Background and Summary of Methodology

2.1 Introduction

Near surface characterization methods such as MASW have typically been developed for conducting geotechnical studies for environmental or civil applications, targeting the shallowest 10’s to 100’s of metres of the subsurface. These methods require specific acquisition techniques and parameters, which would add cost and time to exploration workflows. In this chapter, I review the state-of-the-art in near surface characterization methods, outlining the processes which I will be applying in later chapters. I will also describe the steps necessary to adapt these methods to exploration scale seismic data.

2.2 Multichannel analysis of surface waves (MASW)

Multichannel analysis of surface waves (MASW) methods can be used to detect ground roll amplitudes, calculate Rayleigh wave dispersion, and invert for near surface shear wave velocities. Through inversion of ground roll amplitudes and velocity dispersion, these near surface properties may be more accurately modelled. If this inversion could be applied in such a way that the recorded ground roll be used to model the near surface at every point in a survey area, then the subsequent data processing steps could be performed considering the attenuative effects of the near surface. This would result in data more representative of the actual wavefield, and thus, a more accurate interpretation could be made.

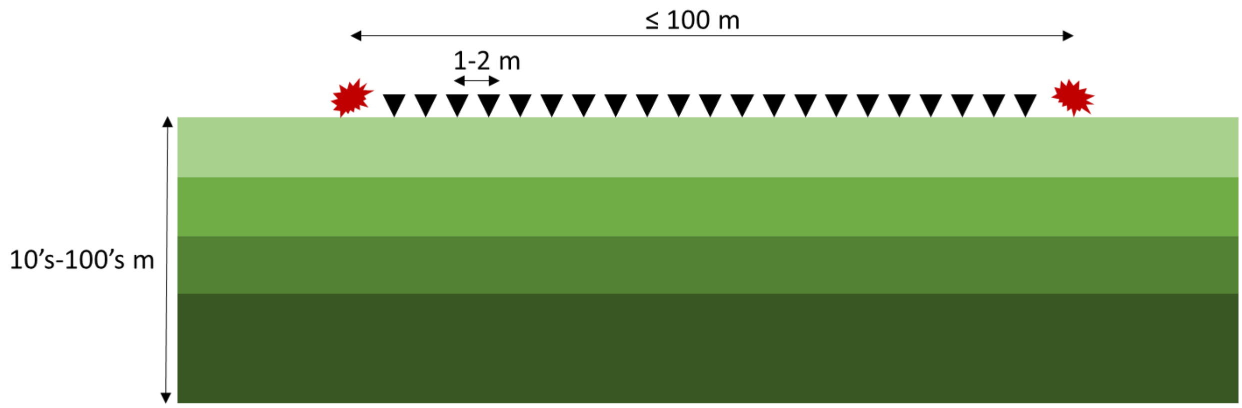

Figure 2-1 Typical field MASW acquisition.

The maximum penetration depth of ground roll is approximately equal to the ground roll wavelength (λ) (Richart el al., 1970). However, the maximum depth for which v_s can be calculated is about half the longest wavelength of ground roll measured (Rix and Leipski, 1991). The minimum definable thickness of the shallowest layer imaged is given by:

$$H_1 \geq 0.5\lambda_{min} = 0.5C_{min}/f_{max} \tag{2.1}$$

Where C_{min} and λ_{min} are the phase velocity and wavelength, respectively, and correspond to frequency f_{max} (Park et al., 1999).

After field acquisition or synthetic modelling, MASW involves generating a dispersion curve of phase velocity vs frequency for acquired Rayleigh waves, then building initial P-wave, S-wave, and density models for a horizontally layered, laterally homogeneous earth, using estimates for the region of the survey (Yilmaz, 2015). Next, the Rayleigh wave dispersion curve for the model is calculated and compared to the observed dispersion. Using the discrepancy, or residual between the modeled and observed curves, the model is adjusted and the process repeated until the difference is minimized (Yilmaz, 2015). This process is described in greater detail in Chapter Three, but laid out here (Figure 2-2) for context.

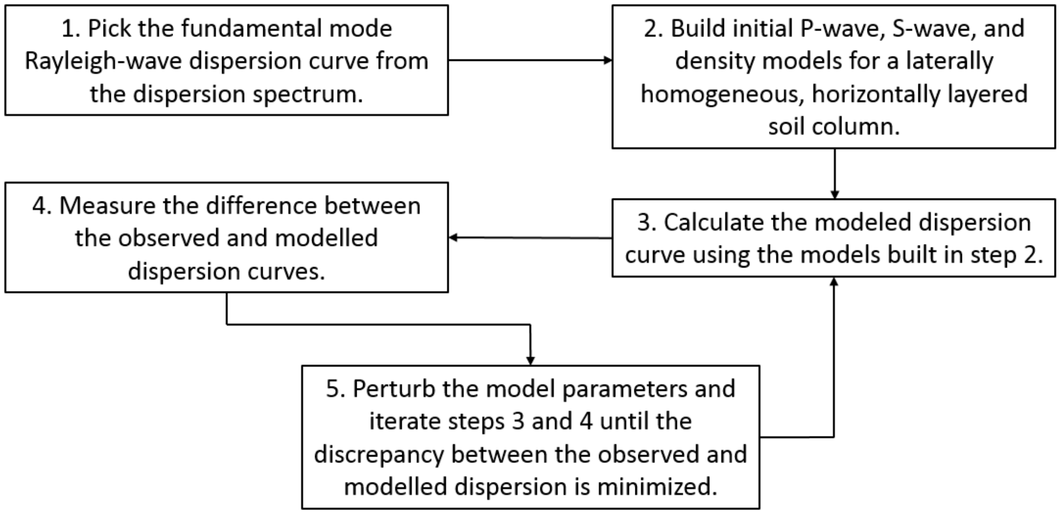

Figure 2-2 Workflow for Rayleigh wave inversion, as can be used in MASW. (Adapted from Yilmaz, 2015).

2.2.1 Dispersion spectrum

Generating accurate dispersion curves is essential for inverting for near surface shear wave velocity profiles. Dispersion means that each frequency component of the wave travels with a different horizontal phase velocity (Yilmaz, 2015). This is visualized on dispersion spectra, displayed as phase velocity versus frequency plots, and show how the phase velocity changes with frequency in the dispersion curve. A flat dispersion curve indicates that no dispersion is occurring.

In this study, dispersion curves are calculated using slant-stack processing and the tau-p transform (Figure 2-3, adapted from Yilmaz, 2015), the process of which follows:

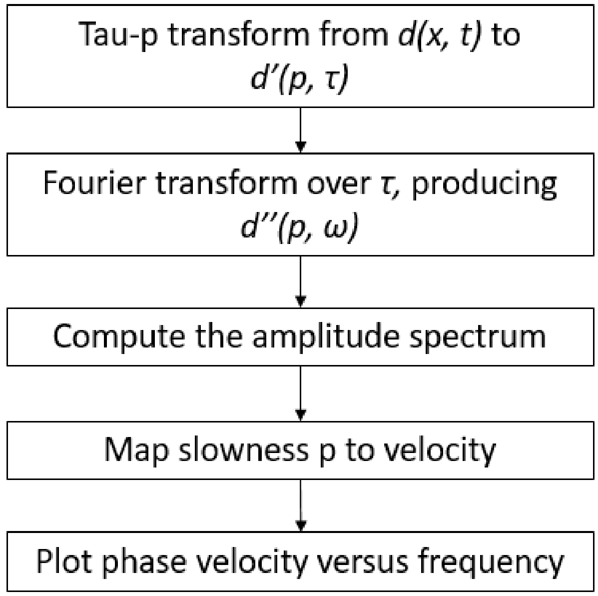

Figure 2-3 Workflow for generating a dispersion spectrum from a shot record. Adapted from Yilmaz, 2015.

1) First, the shot record, *d(x, t)*, is Fourier transformed over *t* to *d'(x, ω)*. These data are then tau-p transformed from *d'(x, ω)* to *u(p, τ)* (Figure 2-4). The discrete tau-*p* transform is described by equation 2.2 (Turner, 1989)

$$F(\tau, p) = \sum_{i=1}^{n} F(x_i, \tau + px_i) \tag{2.2}$$

Where:

n = number of seismic traces used in the transform,

x = horizontal space coordinate or position of the seismic trace,

t = two-way traveltime,

τ = zero offset intercept of event, following τ-*p* transform,

p = apparent slowness,

f = frequency,

F(x, t) = amplitude at *(x, t)* in the standard seismic section, and

F(τ, p) = amplitude at *(τ , p)* in the tau-*p* domain.

This tau-*p* transform is performed over a range of slowness values, producing tau-*p* data with twice as many *p* traces as there were x traces.

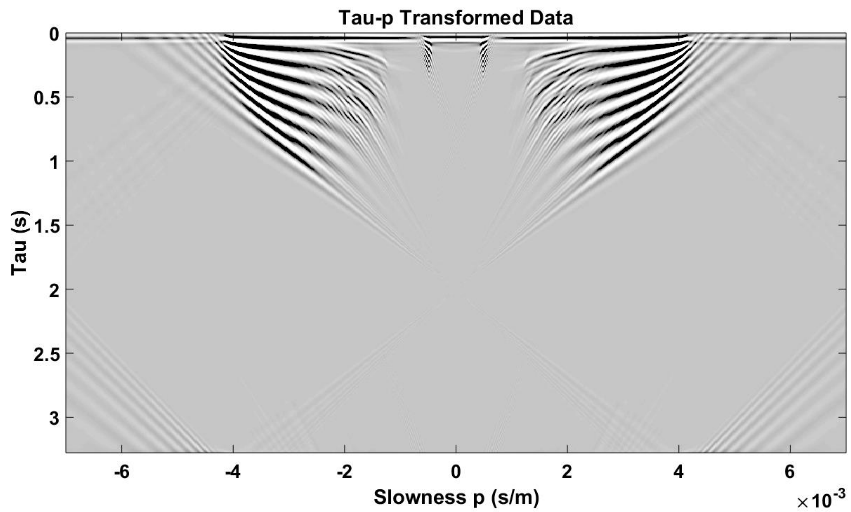

Figure 2-4 Shot record in tau-p domain. Large amplitude linear events are ground roll. Smaller events around 0 s/m are reflection or refraction events.

2) A Fourier transform is then applied to the tau-*p* data, over τ, producing *u'(p, ω)*.

3) The slowness, *p*, is converted to velocity, and the amplitude spectrum A(*v*, *ω*) is calculated, normalized and plotted (Figure 2-5).

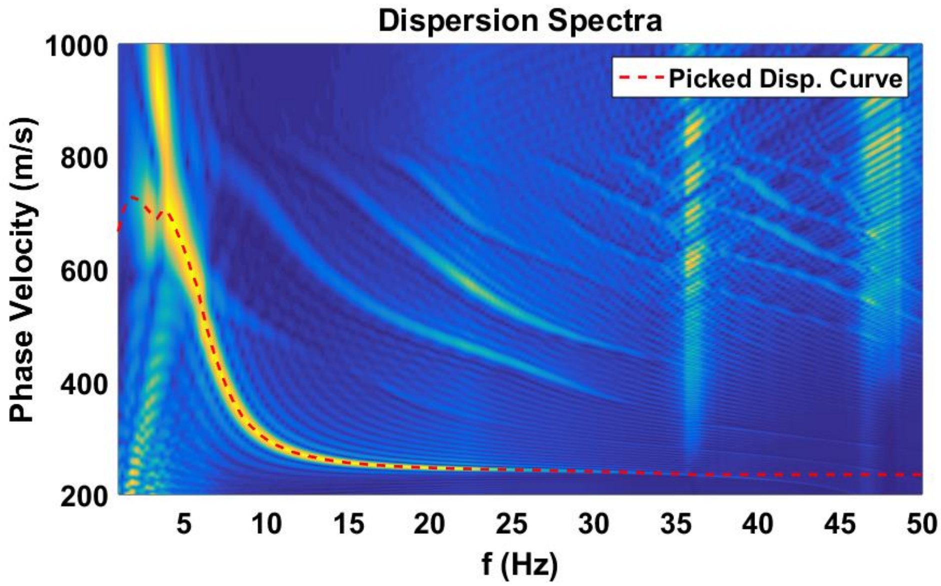

Figure 2-5 Dispersion spectra, with fundamental mode of dispersion picked. The curve appears to trend to higher velocities at low frequency, caused by mode interference and influence of P-wave particle motion.

In Figure 2-5, the fundamental mode of dispersion has been picked. The fundamental mode contains the majority of the surface wave energy, with higher modes (visible in Figure 2-5) containing smaller portions. The fundamental mode dispersion curve asymptotically approaches 92% of both the maximum and minimum shear wave velocities (Udias, 1999). In the case of the model used to generate the curve in Figure 2-5, the maximum Vs is 800 m/s, and the minimum Vs is 250 m/s, which are both approached by the dispersion curve above.

An important component of the dispersion spectra which can have implications for both picking the fundamental mode, and for Rayleigh wave inversion (section 3.3) is “mode-kissing” (Xia et al., 2012). This is mode interference where higher dispersion modes intersect the fundamental mode, and is primarily caused by the influence of P-wave particle motion (Yilmaz, 2015). This particulary causes problems at low frequencies, where most dispersion occurs, and causes the fundamental dispersion curve to appear to trend to much higher velocities than the highest shear wave velocity in the model (as can be seen in Figure 2-5). Higher order modes of dispersion are only detected using multi-channel acquisition, where a high energy source is used (Park et al., 2000), and can be separated from the fundamental mode (Park et al., 1998). The focus of this study is on the fundamental mode only. Higher modes are only considered as sources of noise via mode-kissing.

2.2.2 Theoretical dispersion curves

Theoretical dispersion curves can be generated for 1D geologic models, and are required to compare observed dispersion to dispersion calculated for a geologic model. At each iteration of the inversion (Figure 2-2), the theoretical dispersion curve for the inverted model must be calculated, and compared to the observed dispersion. The difference between these curves can be used to guide the next inversion iteration. These curves are calculated using MATLAB scripts mat_disperse.m and modal.m (Rix et al., 2003). A 1D model with Vp, Vs, ρ, and layer thicknesses is specified

2.2.3 Limitations of characterization methods

A limitation of MASW for reflection surveys, is that it requires the low frequencies of Rayleigh waves to be measured, ideally using low-frequency (4.5 Hz) geophones, while geophones used for reflection surveys generally have a minimum recording frequency of 10 Hz. However, 10Hz geophones have been shown by Bertram et al. (2010) to have recoverable signal down to 2 Hz at offsets up to 1500m, and this sensitivity is especially useful in the case of ground roll. In addition, if Vibroseis is used as the seismic source, sweeps typically begin at around 6 Hz, meaning low frequencies are not even generated (Harrison, 2011). The lack of very low frequencies only limits the depth of investigation, so shallower velocities can still be predicted using data acquired with 10 Hz geophones and a Vibroseis source.

A major limitation introduced when using exploration surveys, which focus on reflected seismic body waves, for near surface characterization focusing on ground roll, is that the spatial sampling requirements of the latter are much more stringent than those of the former. While in MASW specific surveys, the receivers are placed at ~2 m spacing over 10's to 100's of metres, in an exploration survey this same distance could be covered by five or fewer geophones. This can be partially dealt with using interpolation, but the data quality of tightly sampled surveys is unmatched.

If the MASW technique and procedure can be adapted for use with existing reflection data, then the possibilities for application to reflection surveys are greatly expanded. MASW methods produce 1D shear wave velocity profiles, so repeated surveys are necessary at different surface locations to build a 2D velocity profile.

2.3 Shot record processing and interpolation

Exploration seismic data are acquired using the sparse receiver intervals and long receiver line lengths necessary to adequately and economically illuminate and then image the deeper subsurface, which is targeted by these surveys. As a result, the data generated in these surveys are unsuitable in their raw form for use in MASW studies. At receiver spacing equal to those used in the 2011 experimental low frequency Hussar survey of 20 m (Margrave et al., 2011), the aliasing noise is severe enough to mask the dispersion trend at any frequency (Figure 2-6). In data with greater than ideal receiver spacing, such as at Hussar and in most cases, dispersion plots are found to consist almost entirely of noise. In cases such as these, aggressive noise attenuation and resampling methods are necessary to generate resolvable dispersion curves. The workflow shown in Figure 2-7 was designed as part of this thesis research to be applied to poorly sampled data before dispersion spectra are calculated. How this workflow was determined will be discussed in Chapter Four.

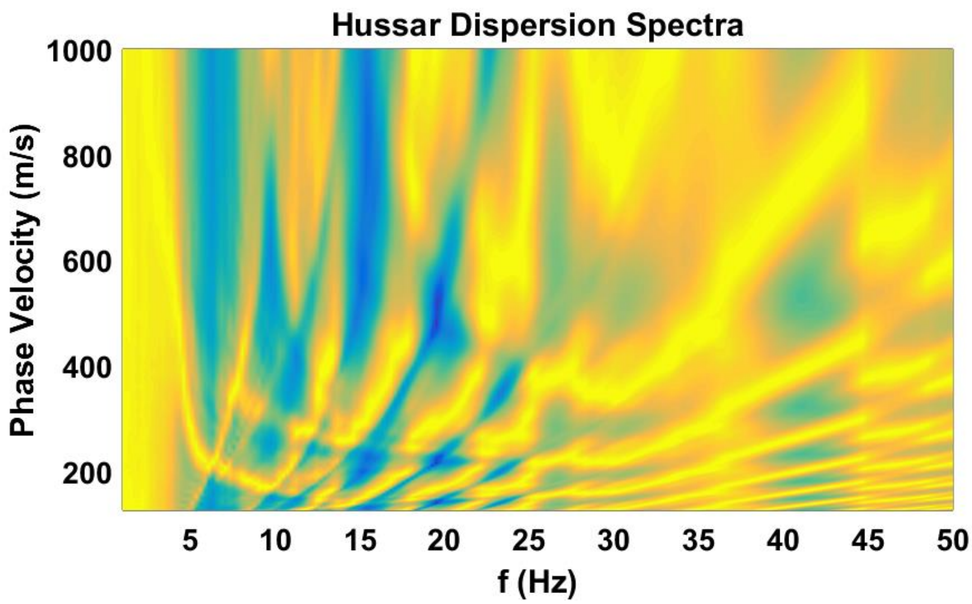

Figure 2-6 Dispersion spectrum generated from a raw Hussar shot record. Note high amplitude noise obscuring dispersion trends.

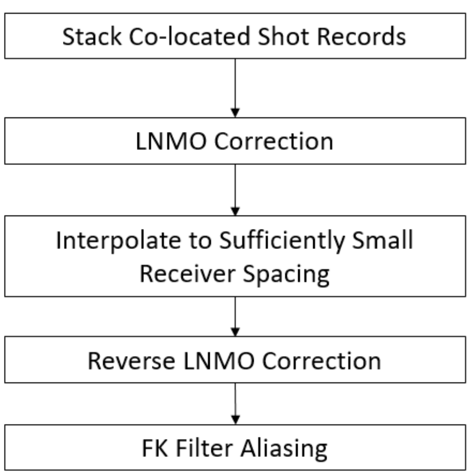

Figure 2-7 General processing flow for dispersion curve improvement.

2.3.1 Linear normal moveout correction

Linear normal moveout (LNMO) corrections apply a static shift to each trace, in order to flatten arrivals in shot records. The static shift is determined by the following,

$$LNMO\ Static\ Shift = \frac{Trace\ Offset}{LNMO\ Velocity} \tag{2.3}$$

For a laterally heterogeneous near surface, the positive and negative offsets will have different velocities and time-dips, resulting in different corrections being applied on either side of the source. A simpler and faster method which achieves similar results, is performing a single LNMO correction for an average LNMO velocity of the ground roll. This flattens the ground roll arrivals, which improves the 2D interpolation.

2.3.2 Interpolation

The interpolation used for this study is a 2D trace interpolation, 2DIntr in GEDCO Vista, which is an implementation of an iterative anti-leakage Fourier data regularization algorithm (GEDCO, 2013, Xu et al., 2005). The LNMO corrected shot records are input into the interpolation algorithm, which runs over the entire dataset. Initially in the interpolation, a new trace is added between every existing trace, estimated by the mean of the surrounding traces. This halves the receiver spacing for the interpolated data. After the initial approximation of the interpolated traces has been created, the process described next is iterated a set number of times. (Generally, for this study, 10 iterations are used, as further iterations fail to improve the result significantly.)

Data are Fourier transformed into the frequency-wave number (FK) domain. This FK spectrum is considered to be the result of convolution of the full data spectrum with the Fourier transform of the sampling operator (1 or 0 for existing or missing traces). The Fourier coefficient is calculated for each frequency, and plotted against wavenumber (Xu et al., 2005). Components of poorly interpolated data will plot with much higher Fourier coefficient values than other wavenumbers. This spectrum distortion is known as spectrum “leakage”, meaning that each original spectral component affects others and components with stronger amplitudes have more impact especially on their nearest neighbors (GEDCO, 2013).

At each iteration, spectrum values larger than a preset threshold (in our case 10%) are selected and values which are also local maxima are accumulated in the output spectrum. After an inverse FK transformation, the components from all previous iterations are subtracted from the input frequency spectrum, which will then be the input for the next iteration. Thus, by subtracting the strongest components, the strongest distortion of weaker components due to “leakage” is reduced.

The threshold is reduced at each step of the procedure from the defined value to zero, which also allows the updating of previously estimated components to reduce inaccuracy of the initial estimation of spectrum components at later iterations.

2.3.3 FK filtering

FK filtering is employed to attenuate aliasing noise, as well as to remove any reflections, refractions, or model boundary reflections. Since all events in the time domain (x, t) with the same phase velocity are represented by a single linear event in the frequency domain (k_x, f) (Margrave, 2006), FK transforming shot records containing several linear events produces plots with discrete events which can then be selectively filtered. In contrast to the most common use of the FK filter, here high FK dip events such as reflections, and events with opposing dips (aliasing) will be filtered from the data.

2.4 Conclusion

In this chapter, I have laid out the necessary background and theory behind surface waves, and how they are used in modern near surface characterization methods. The process of MASW, in ideal near surface study conditions was described, and the steps necessary to apply MASW to exploration scale data were introduced. These steps will be applied to synthetic and field data in later chapters.

Chapter Three: Forward Modelling and Inversion

3.1 Introduction

The process of MASW requires both forward and inverse modelling to predict near surface shear wave velocities. In addition, synthetic data tests and applications of the processes developed in this study, require synthetic geologic model building and forward seismic modelling to generate the study data. In this chapter, I describe the procedures used in model building, forward modelling, dispersion curve picking, the velocity inversion algorithm, and the errors which arise with modelling.

3.2 Forward modelling

Generally, forward modeling consists of predicting the measured data that would be obtained, given the properties of the physical system considered. In seismology, an example of a forward modelling procedure is the prediction of the vibration in the earth during and after an earthquake given a set of seismic velocities and details about the source. In exploration seismology, the analogous procedure is to predict the vibration after a charge of dynamite is exploded, or during and after a Vibroseis sweep. In forward modelling, a model of Earth properties and their spatial distribution must first be built, after which a response may be calculated. Here, I outline the methods used in the current research project to build these models, and simulate a seismic experiment being carried out over them.

3.2.1 Model building

Geologic models used for synthetic model tests were produced in MATLAB by defining the model geometry and rock property parameters (Adapted from Cova, 2015). The x and z dimensions of the model are specified, as well as the grid spacing. Layer or geologic unit vertices are chosen, and a P-wave, S-wave, and density are assigned to each polygon. The unit polygons are then superimposed, building a 2D velocity and density model. For example, Figure 3-1 shows a simple geologic model, 1000m wide by 100m deep, with layer boundaries at 20m, 40m, and 60m depth. This model building program allows the building of custom laterally homogeneous or heterogeneous models. Vp, Vs, and ρ models are saved in SOFI2D binary format for use in forward elastic modelling.

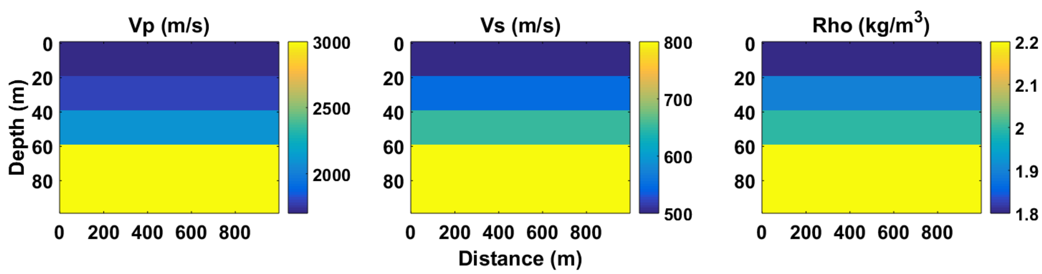

Figure 3-1 Simple laterally homogeneous geologic model.

3.2.2 Finite difference modelling

All forward wavefield propagation modelling in this study is conducted using SOFI2D, a 2D finite difference seismic modelling engine (Bohlen et al., 2016). The geologic models built in MATLAB (described in section 3.2.1) are used as input for SOFI2D. Finite difference methods are used to discretize and solve the wave equation, and thus approximate wave propagation in 2D elastic media. The finite difference software in SOFI2D is based on the work of Virieux (1986) and Levander (1988), using standard staggered grid distribution of wavefield and material parameters.

A fourth order finite difference operator is used in the modelling. SOFI2D allows the user to specify the x, z, and Δx of the receivers, which will typically be placed at 5m depth and at various spacings. An explosive point source is used, placed at the receiver depth. The source shape is given by a Fuchs-Muller wavelet, with a central frequency of 12 Hz (Figure 3-2).

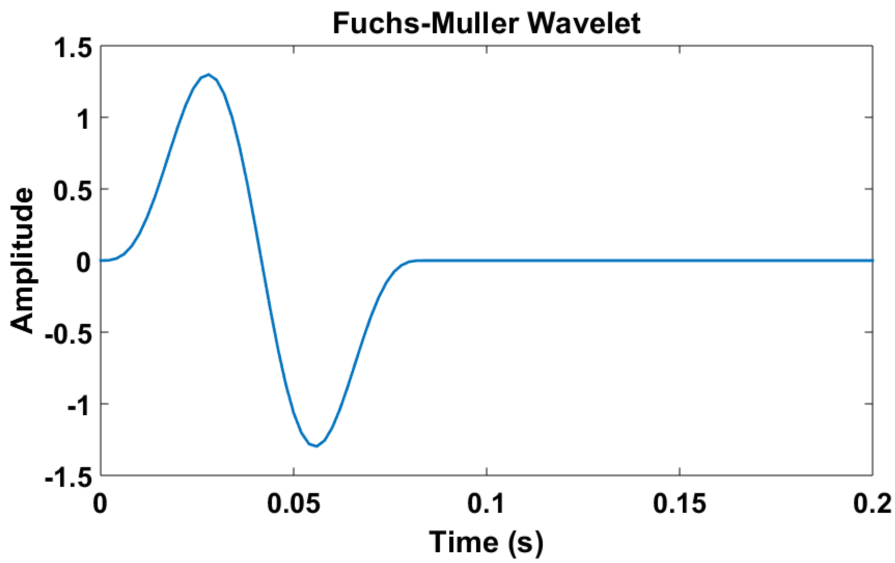

Figure 3-2 Fuchs-Müller wavelet, with a central frequency of 12 Hz.

3.2.3 Boundary conditions

As mentioned in section 2.2, elastic solids can only support the propagation of surface waves when they are bounded by a stress-free surface, called the free surface (Yilmaz, 2015). This requires that the top of the model exhibit free surface conditions, that is, vertical and horizontal stress equal to zero (Levander, 1988).

The sides and bottom of the model have convolutional perfectly matched layer (CPML) conditions applied (Komatitsch and Martin, 2009), with an absorbing frame width of 20 grid points, or 40 m. These limit the boundary reflections; however, low amplitude reflections still occur in some cases.

3.3 Inversion of dispersion curves

The inverse problem, in which I wish to re-create the earth model from a measured response, is the opposite of the forward problem, described in section 3.2. Using the inverse method in this study will allow the prediction of a plausible earth velocity model which could have produced the dispersion response which was measured in the field, or modelled using software.

Once dispersion spectra have been generated from a synthetic or field data set, the fundamental mode curve can be picked, and used to invert for near surface shear wave velocities. Since shear wave velocity controls changes in Rayleigh wave phase velocity (Xia et al., 1999), the shear velocities can be inverted for from Rayleigh wave dispersion curves. I will be utilizing a linear least-squares inversion workflow for the prediction of near surface shear wave velocities (following Lines and Treitel, 1984). The goal of this is to find the model that minimizes the sum of squares of the difference between a synthetically modelled response, and the observed response. For this study, I am minimizing the error between the synthetic modelled dispersion curve (equation 3.1a), and an observed dispersion curve (equation 3.1b), generated from field data or synthetic data. Let the f (number of frequencies) observations of phase velocity be represented by the vector

$$\boldsymbol{d}_{obs} = \begin{bmatrix} y_1 \\ y_2 \\ \vdots \\ y_f \end{bmatrix} \tag{3.1a}$$

and let the synthetic model phase velocity response be the vector

$$\boldsymbol{d}_{syn} = \begin{bmatrix} s_1 \\ s_2 \\ \vdots \\ s_f \end{bmatrix} \tag{3.1b}$$

where n is the number of layers.

The inversion procedure involves four steps (similar to Figure 2-2):

1. The fundamental mode dispersion curve is picked from the observed field or synthetic dispersion spectra.
2. An initial geologic model is estimated from the observed dispersion curve, and a synthetic theoretical dispersion curve is calculated from this model.
3. A least-squares inversion is used to calculate a parameter change vector δ, which will update the initial velocity model.
4. Step 3 is iterated until the error between the observed dispersion curve and predicted dispersion curve is minimized.

The model, and thus the dispersion curve, is a function of several parameters, including Vp, Vs, ρ, number of layers, and layer thickness, which are represented in the model vector $\boldsymbol{\theta}$.

$$\boldsymbol{\theta} = \begin{bmatrix} \boldsymbol{\theta}_1 \\ \boldsymbol{\theta}_2 \\ \vdots \\ \boldsymbol{\theta}_n \end{bmatrix} \tag{3.2}$$

where n is the number of layers.

3.3.1 Inversion initialization

To initialize the inversion, an initial model must be built, whose properties are compared to those in estimated (inverted) models. Dispersion spectra have limited sensitivity to rock density (Xia et al., 1999), so are assumed known. In the case of synthetic tests, the true densities of the model are assigned to the model. In the case of field data tests where density is unknown, densities are assigned to each layer, increasing uniformly with depth. The number of layers for the initial model are chosen based on the shape and spread of the dispersion curve (Figure 3-3). Dispersion frequencies are chosen where there is a change in phase velocity visible. The high and low frequencies are picked approximately where the curve asymptotically approaches the maximum and minimum velocities. The rest of the points are picked where changes are visible, and where the different frequencies are likely to predict sufficiently thick layers. For example, picking 10, 11, 12 Hz will likely predict three very thin layers, which are unlikely to have been sufficiently resolved in the data. Here, picking 10 and 13 Hz is sufficient.

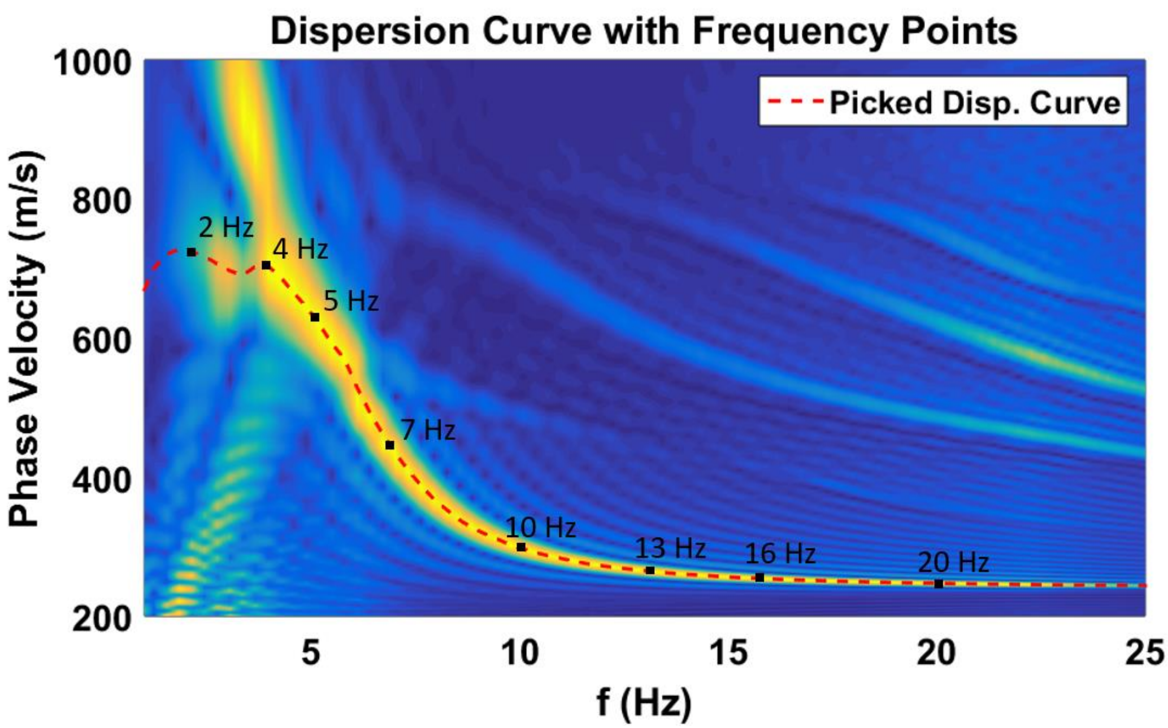

Figure 3-3 Dispersion curve with picked frequency points to be used in initial model estimation.

Layer velocities, thicknesses, and depths are calculated using relationships derived in Xia et al. (1999), as follows:

$$Vs_1 = \frac{V_r(high)}{0.88} \text{ (for the first layer)}$$

$$Vs_n = \frac{V_r(low)}{0.88} \text{ (for the half-space, n}^{\text{th}}\text{ layer)} \quad (3.3)$$

$$Vs_i = \frac{V_r(f_i)}{0.88} \; (i = 2, 3, \ldots, n\text{-}1)$$

where 0.88 is a constant based on Poisson's ratio (Stokoe et al., 1994), as well as modelling trials in Xia et al. (1999). V_r(high) is the dispersion phase velocity where the curve approaches the high frequency asymptote, V_r(low) is the velocity where the curve approaches the low frequency asymptote, and $V_r(f_i)$ are the velocities from selected frequencies in between. A Vp/Vs ratio of 2 is assumed, allowing simple calculation of P-wave velocities from initial estimated S-wave velocities.

Depths are calculated based on the fact that each wavelength of Rayleigh wave has a different maximum penetration depth, and thus samples a different point in depth. The same frequencies used in velocity calculations, and the calculated shear velocities, are used in equation 3.4 (Xia et al., 1999) to calculate depth being sampled.

$$\mathrm{z_n} = 0.63\,\lambda = 0.63\,\frac{\mathrm{Vs_n}}{\mathrm{f_n}} \tag{3.4}$$

Note that the inversion initialization isn't predicting the layer boundary depths, rather it is predicting the velocity at a point in depth. The layer boundary would lie at an unknown point between adjacent points with different velocities. Once the velocities, depths and thicknesses have been calculated, an initial theoretical dispersion curve can be calculated, as in section 2.2.2.

3.3.2 Least-squares inversion

Recalling that *s* represents the synthetic model phase velocity, a perturbation of this model can be represented by:

$$\boldsymbol{d_{syn}} = \boldsymbol{d^{0}_{syn}} + \mathbf{J\delta} \tag{3.5}$$

where $\boldsymbol{d_{syn}}$ is the updated model's phase velocity vector, $\boldsymbol{d_{syn}^0}$ is the initial model's phase velocity vector, **J** is the *f* x *n* Jacobian matrix of partial derivatives (equation 3.6, 3.7), and $\boldsymbol{\delta} = \boldsymbol{\theta} - \boldsymbol{\theta}^{\mathbf{0}}$ is the parameter change vector with elements δ_f representing the changes or perturbations to the S-wave velocity in the model.

$$\mathbf{J}_{\mathrm{fn}} = \frac{\partial d_{syn_f}}{\partial \theta_{\mathrm{n}}} = \frac{d_{syn_f}(\theta_n + \delta\theta) - d_{syn_f}(\theta_n)}{\delta\theta} \tag{3.6}$$

$$\mathbf{J}_{\mathrm{fn}} = \begin{bmatrix} \frac{\partial d_{syn_1}}{\partial \theta_1} & \cdots & \frac{\partial d_{syn_1}}{\partial \theta_n} \\ \vdots & \ddots & \vdots \\ \frac{\partial d_{syn_f}}{\partial \theta_1} & \cdots & \frac{\partial d_{syn_f}}{\partial \theta_n} \end{bmatrix} \tag{3.7}$$

Since Vs is the only parameter being inverted for, that is the only model parameter which will be perturbed in $\boldsymbol{\delta}$. In equation 3.6, the $\delta\theta$ term is some small change in Vs. The error, or residual between the synthetic response **s** and the observed data **y** is represented by vector **e**:

$$\mathbf{e} = \mathbf{d_{obs}} - \mathbf{d_{syn}} \tag{3.8}$$

Combining equations 3.5 and 3.8 gives:

$$\mathbf{d_{obs}} - (\mathbf{d_{syn}^0} + \mathbf{J}\boldsymbol{\delta}) = \mathbf{e} \tag{3.9a}$$

$$\mathbf{d_{obs}} - \mathbf{d_{syn}^0} = \mathbf{J}\boldsymbol{\delta} + \mathbf{e} \tag{3.9b}$$

the left-hand side of 3.9b gives:

$$\mathbf{g} = \mathbf{d_{obs}} - \mathbf{d_{syn}^0} \tag{3.10}$$

where the vector **g** is the discrepancy, or residual, vector, the difference between the initial synthetic model's dispersion and the observed dispersion. The cumulative squared error will be defined as:

$$S = \mathbf{e^T e} \tag{3.11}$$

In the Gauss-Newton inversion, the normal equations are derived (Lines and Treitel, 1984):

$$\mathbf{J^T J \delta = J^T g} \tag{3.12}$$

from which a solution for **δ**, the parameter change vector which minimizes a local approximation of the objective function, can be calculated. However, instabilities in Gauss-Newton inversion arise when $\mathbf{J^T J}$ is nearly singular. When this occurs, the elements of **δ** grow without bound, causing the solution to diverge sharply.

3.3.2.1 Regularization

A common, essentially unavoidable issue in geophysical inverse problems is non-uniqueness, i.e., the fact that many models produce the same data (Virieux and Operto, 2009). Regularization is an inversion preconditioning technique used to make the inversion better-posed. Generally, a regularization scheme is one in which additional criteria are used to select one of the infinite number of models honouring the data.

In this research, I regularize the problem using the Marquardt-Levenberg method, also known as damped least-squares. In this method, a constraining condition is imposed on the parameter change vector **δ**. This constraint prevents the unbounded oscillations in the solution observed with the Gauss-Newton method. A modified form of the normal equations arises from the Marquardt-Levenberg method, yielding

$$\boldsymbol{\delta} = (\mathbf{J^T J} + \beta \mathbf{I})^{-1} \mathbf{J^T g} \tag{3.13}$$

where β is a Lagrange multiplier, which can be considered a “damping factor” (Levenberg, 1944), and **I** is the identity matrix. Through limiting the energy of the parameter change vector **δ**, large changes in the model vector **θ** are penalized and the tendency will be to converge on a model. This is a hybrid method, as it strikes a balance between the method of steepest descent and the method of Gauss-Newton least-squares, as shown in Figure 3-4. A β value of 0 in equation 3.13 is equivalent to Gauss-Newton least-squares. It is recommended by Lines and Treitel (1984) to set β initially as a large positive value, taking advantage of the good initial convergence properties of the steepest descent method. Absolute numerical values of β, which depend on the units used in the data and model parameters, number of data, number of model parameters, etc., are difficult to gain insight from, nevertheless it was found in this study that setting the β value at 5 produced stable results over enough iterations for the solutions to converge. At each iteration, β is multiplied by 0.8, until it reaches a minimum of 0.5, so that the inversion is weighted towards linear least-squares convergence closer to a solution. With β below 0.5, the instability witnessed originally with the Gauss-Newton method is empirically found to re-emerge.

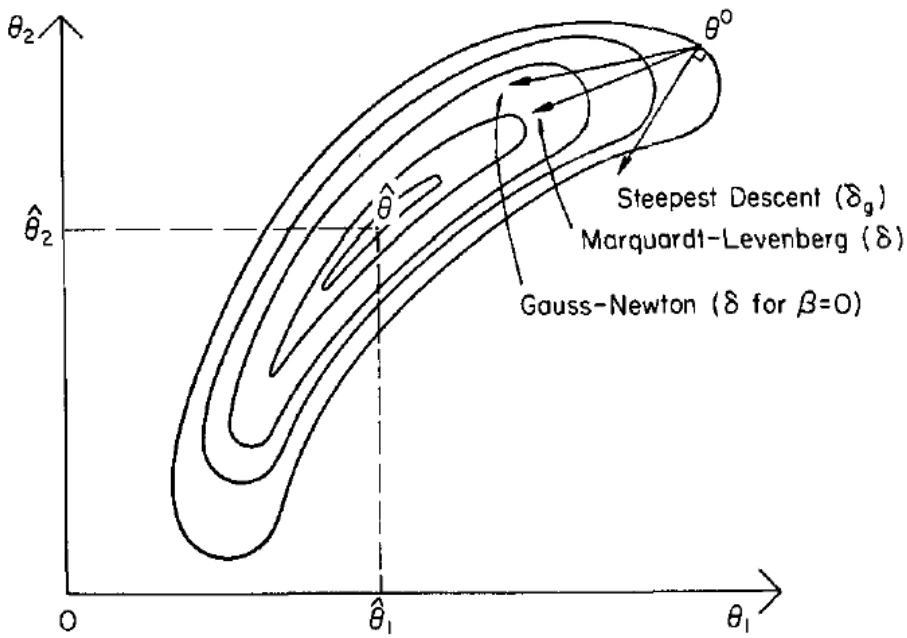

Figure 3-4 Geometric relation between the Gauss-Newton, Marquardt-Levenberg, and Steepest Descent solutions, converging towards θ̂ (From Lines and Treitel, 1984).

Gauss-Newton and Marquardt-Levenberg least squares inversion are empirically found to yet be insufficient on their own to accurately predict a plausible earth model; the inversion was found to converge towards models with implausibly high variability between adjacent layers. An additional regularization is added to equation 3.13 to help constrain and guide the inversion to a more realistic result than would otherwise be found. This regularization, **R**, minimizes the velocity change from one layer to the surrounding layers, reducing extreme velocity variations, and this was found to limit spurious inversion results.

R is defined here to minimize the velocity change between subsequent layers,

$$\mathbf{R} = \frac{1}{2}\sum_{i=1}^{n-1}(\mathrm{Vs}_n - \mathrm{Vs}_{n-1})^2 \tag{3.14}$$

Taking the first and second derivatives, the R terms to be inserted into the objective function are found:

$$\frac{\partial \mathbf{R}}{\partial \mathbf{Vs_n}} = 2\mathrm{Vs}_n - \mathrm{Vs}_{n+1} - \mathrm{Vs}_{n-1} \tag{3.15}$$

$$\frac{\partial^2 \mathbf{R}}{\partial \mathbf{Vs_{n1}} \partial \mathbf{Vs_{n2}}} = 2\,\delta(n_1,n_2) - \delta(n_1+1,n_2) - \delta(n_1-1,n_2) \tag{3.16}$$

By taking the derivative of the objective function with the regularization, Φ, it can be seen where the R terms should be added.

$$\Phi = \frac{1}{2}\left\|\mathrm{d_{obs}} - \mathrm{d_{syn}}\right\|^2 + \mathrm{R} \tag{3.17}$$

$$\frac{\partial \Phi}{\mathbf{Vs_n}} = \left(\mathrm{d_{obs}} - \mathrm{d_{syn}}\right)\frac{\partial \mathrm{d_{obs}}}{\partial \mathrm{Vs_n}} + \frac{\partial \mathrm{R}}{\partial \mathrm{Vs_n}} \tag{3.18}$$

This will replace the second term of equation 3.13:

$$\frac{\partial \Phi}{\mathrm{Vs_n}} = \mathbf{J}^{\mathrm{T}}\mathbf{g} + \frac{\partial \mathrm{R}}{\partial \mathrm{Vs_n}} \tag{3.19}$$

Taking the second derivative of Φ (equation 3.20), it is seen that the solution (equation 3.21) will replace the first term of equation 3.13:

$$\frac{\partial^2 \Phi}{\mathbf{\partial Vs_{n1} \partial Vs_{n2}}} = \frac{\partial \mathrm{d_{obs}}}{\partial \mathrm{Vs_{n1}}}\frac{\partial \mathrm{d_{obs}}}{\partial \mathrm{Vs_{n2}}} + \frac{\partial^2 \mathrm{R}}{\partial \mathrm{Vs_{n1}}\, \partial \mathrm{Vs_{n2}}} \tag{3.20}$$

$$\frac{\partial^2 \Phi}{\partial \mathbf{Vs_{n1}} \partial \mathbf{Vs_{n2}}} = \mathbf{J^T J} + \frac{\partial^2 \mathrm{R}}{\partial \mathrm{Vs_{n1}}\, \partial \mathrm{Vs_{n2}}} \tag{3.21}$$

The velocity update vector $\boldsymbol{\delta}$ (equation 3.13) with the regularization (equations 3.15, 3.16) added is:

$$\boldsymbol{\delta}_{\mathbf{R}} = ((\mathbf{J^T J} + \lambda \frac{\partial^2 \mathbf{R}}{\partial \mathbf{Vs_{n1}} \partial \mathbf{Vs_{n2}}} + \beta \mathbf{I})^{-1} (\mathbf{J^T g} - \lambda \frac{\partial \mathbf{R}}{\partial \mathbf{Vs_n}}) \tag{3.22}$$

The value λ is the weight applied to the regularization. A higher value will reduce the velocity differences from layer to layer, where a smaller value will give a result closer to the Marquardt-Levenberg $\boldsymbol{\delta}$.

At the end of each iteration, $\boldsymbol{\delta}_{\mathbf{R}}$ is calculated, which is a velocity change vector with each component representing an update to the velocity for a single layer. This $\boldsymbol{\delta}_{\mathbf{R}}$ added to the initial model Vs vector, providing a new starting model for the next inversion iteration. The inversion iterates until the error (equation 3.11) is minimized.

3.4 Modelling error

Despite best efforts to properly formulate an inversion experiment and process, the inverted model is unlikely to perfectly match the original model measured. Multiple issues could cause this mismatch in data. In this study, the ill-posedness of the inversion, addressed in 3.3.2.1, is observed in non-unique solutions, where several models produce equal dispersion curves. A major source of uncertainty in this study arises from using different processes to generate the dispersion curves themselves. Another contributor to the residual is the difference between dispersion curves at very low frequencies, where mode interference causes the picked dispersion curve to trend to higher velocities than exist in the model, as shown in Figure 2-5. In this study, the error, or residual is calculated using equation 3.11, taking the difference between the observed dispersion curve, and the inverted or predicted dispersion curve. This residual is calculated at the end of each iteration, to track the inverted model improvements.

Modelling error can be illustrated with a simple two-layer synthetic example. For this example, Marquardt-Levenberg inversion will run without the regularization to illustrate the matching of dispersion curves. The model shown in Figure 3-5, has a near surface layer in the top 50m, with half-space below. The dispersion spectra generated from a survey with 10m receiver spacing is shown in Figure 3-6, with the fundamental mode of dispersion picked. Note, while the near surface layer Vs is 500m/s, the dispersion curve trends towards higher velocities, and doesn't asymptotically approach any velocity. Proceeding with the inversion, the result from the first iteration is shown in Figure 3-7. The depth to the half-space is assumed for this example. The result after six inversion iterations is shown in Figure 3-8, where the predicted model has now converged to the true model. The dispersion curve generated from this inverted model is compared to the observed dispersion curve in Figure 3-9. The dispersion curves are a good match from 5 Hz onwards, with errors between them at lower frequencies. This is caused by the higher-than-realistic velocities at low frequencies in the picked dispersion curve.

The dispersion in Figure 3-6 was generated from modelled finite-difference data, while the synthetic curves generated during the inversion, to which the modelled curve is compared, were calculated using search techniques. Because of the difference in the way the curves were generated, modelling errors in the inversion results are observed.

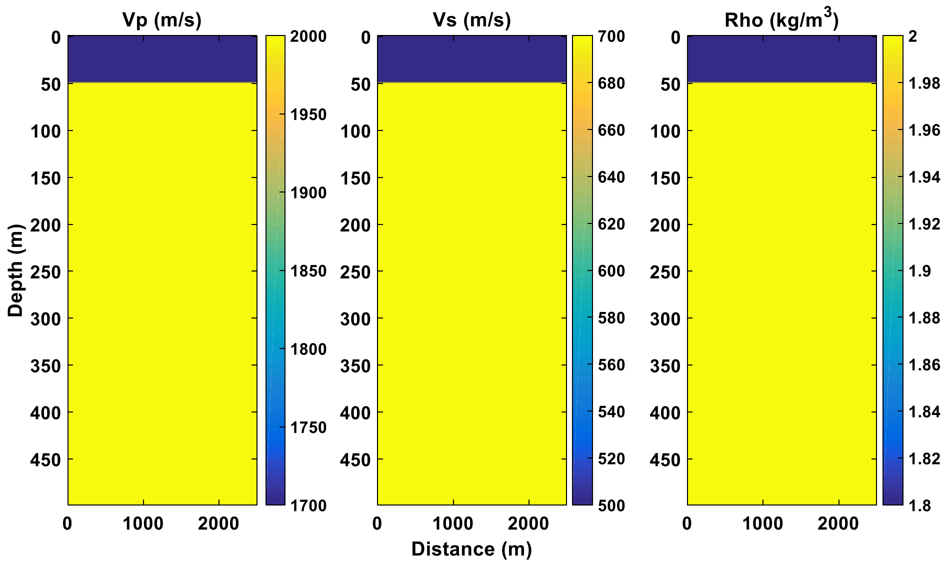

Figure 3-5 Two layer synthetic model.

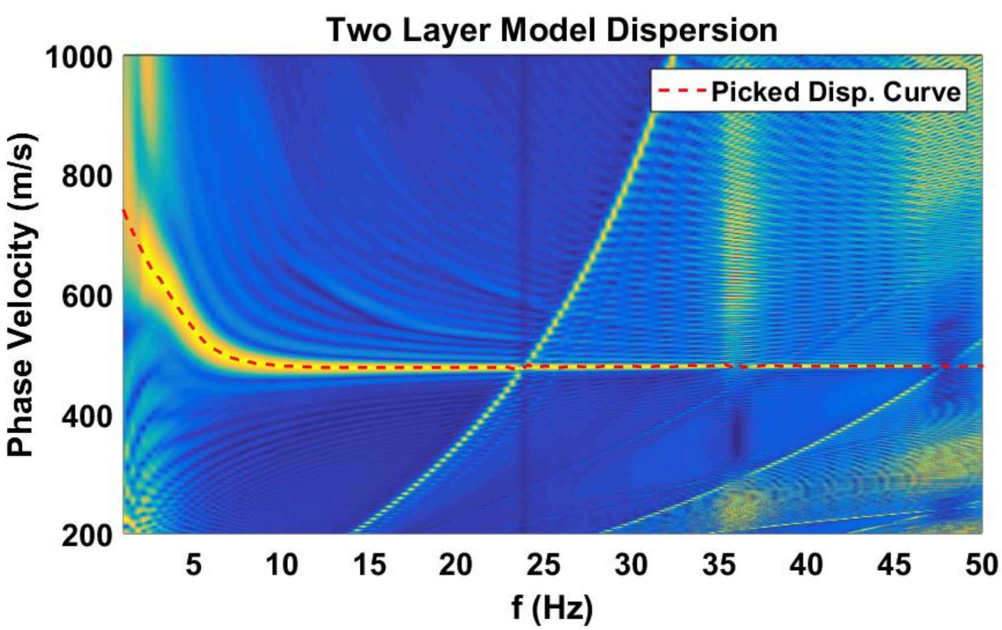

Figure 3-6 Dispersion spectra from the above two layer model.

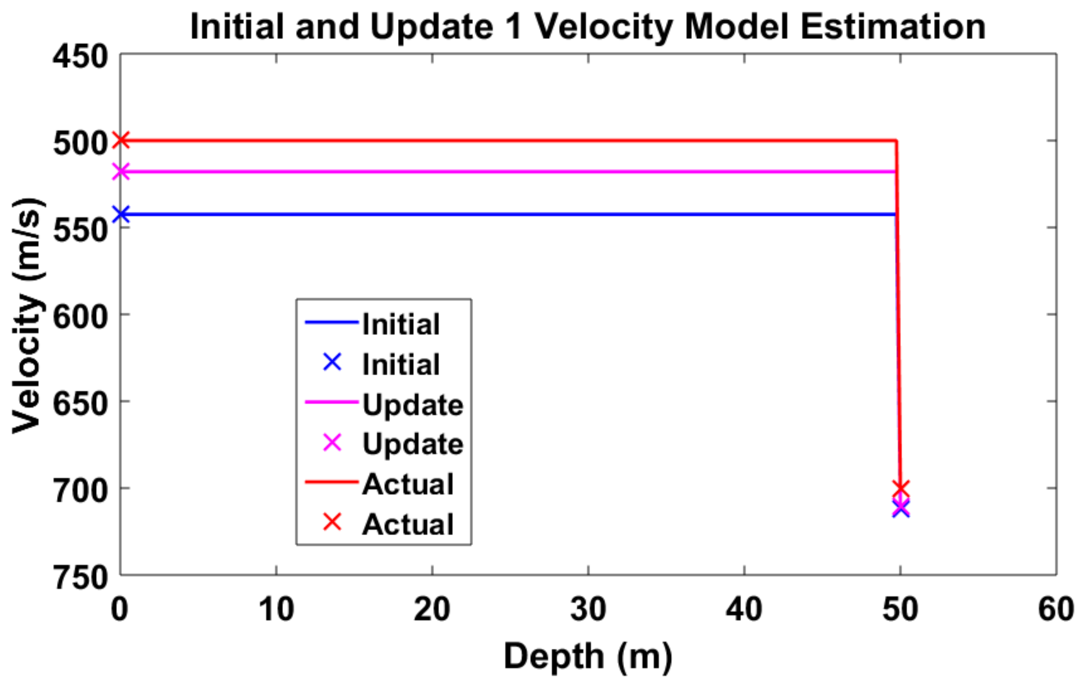

Figure 3-7 Initial model estimate, actual model, and first iteration inversion prediction.

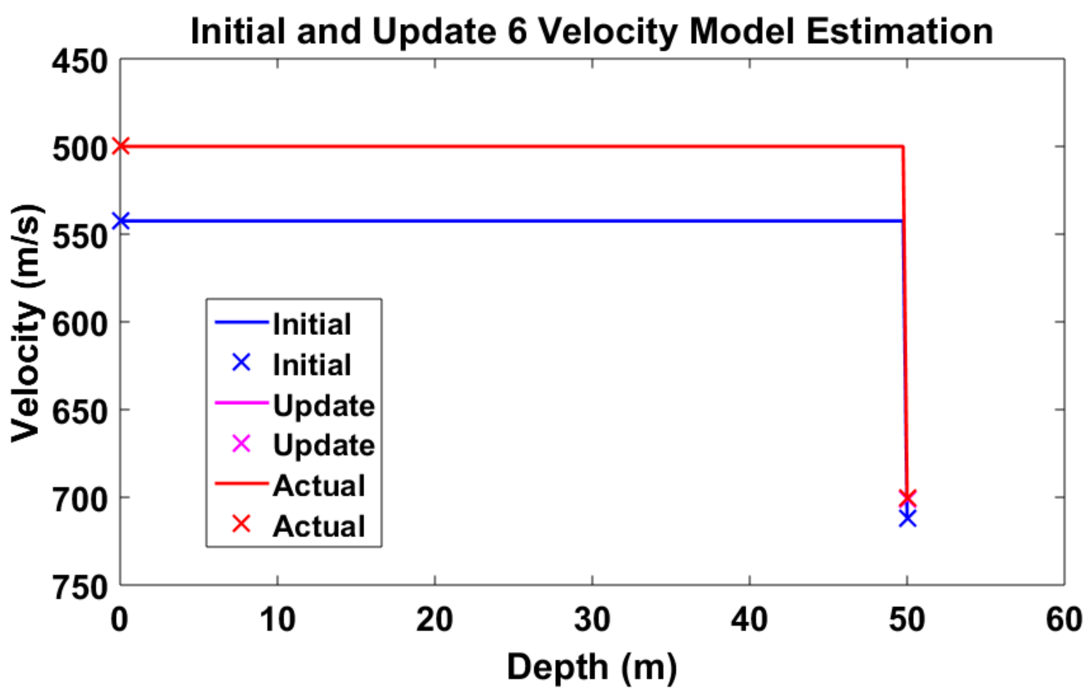

Figure 3-8 Inversion results after six iterations. The inversion has converged with the true model.

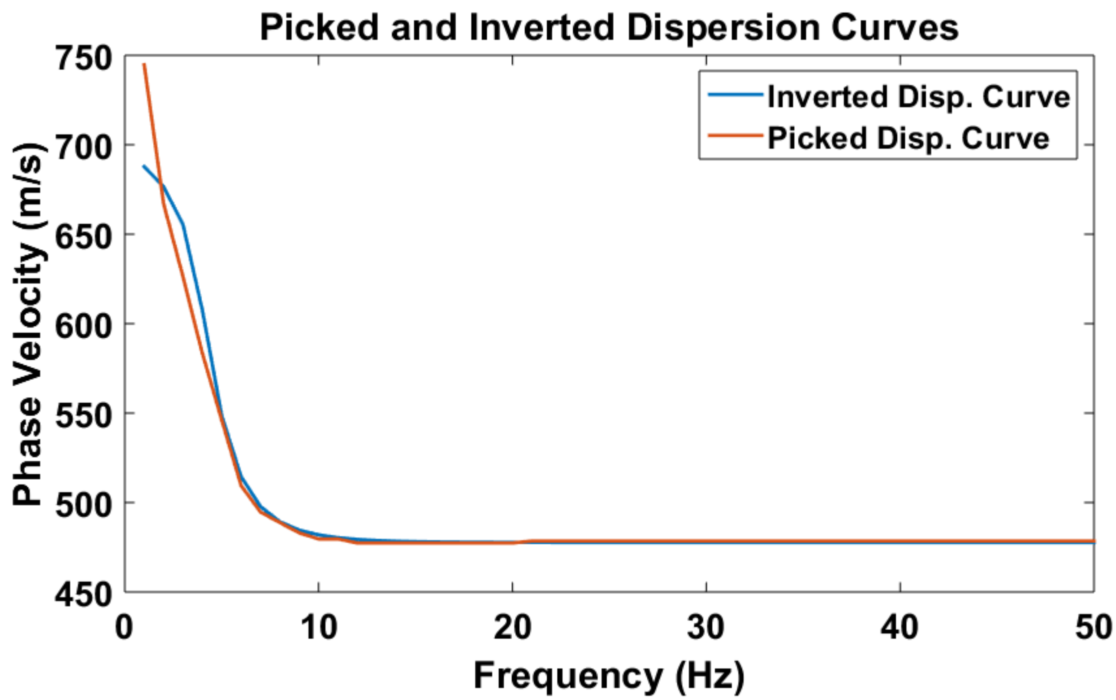

Figure 3-9 Inversion results, compared to observed dispersion curve. RMS error is 4.86 x 10^3.

Eliminating the low frequencies, where mode interference is occurring, is a good method for reducing the modelling error, and improving the inversion results. With the same two-layer model as above, if I eliminate the 1 Hz phase velocity from the observed dispersion curve, the inversion results are shown in Figure 3-10, reducing the RMS error to 380.5. The observed dispersion curve is still influenced by the mode-interference-caused higher velocities, but the highest of these is removed, limiting the influence on the inverted model.

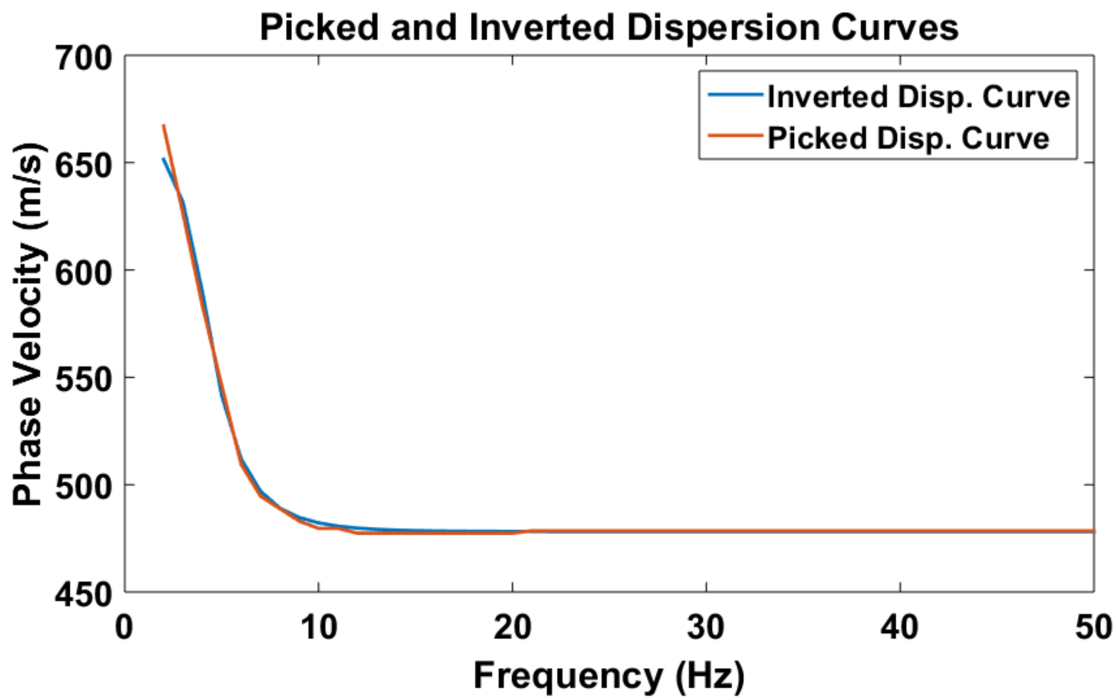

Figure 3-10 Inversion result when 1 Hz is eliminated from the observed curve. RMS error is reduced to 380.5.

To quantify the extent of the modelling error, I can run a simple test. Rather than inverting for velocity from the SOFI2D modelling generated dispersion curve (Figure 3-6), I invert from the modal.m generated dispersion curve. In this method, the inversion should be able to re-create the curve for the actual model with high accuracy. The steps are as follows:

1. Predict synthetic dispersion curve for the velocity model.
2. Estimate an initial velocity model from this dispersion curve, using two frequencies on the curve.
3. Calculate the dispersion curve for this model.
4. Invert for velocity from this curve and the “measured” curve from step 1.

The results of this experiment are shown in Figure 3-11, with an RMS error is 0.0042.

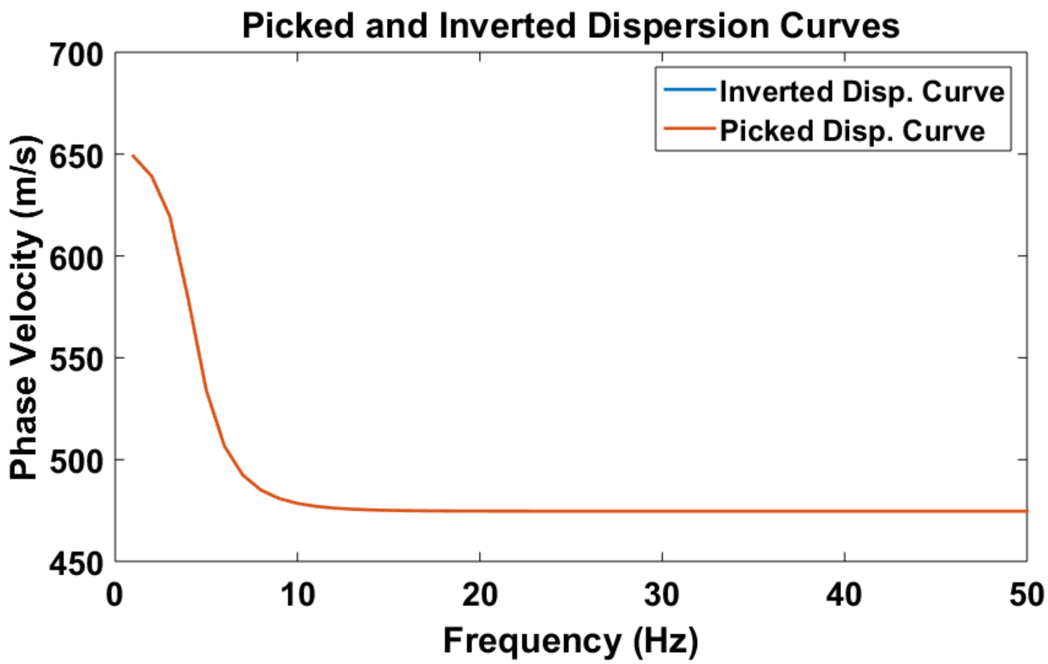

Figure 3-11 Inversion result for the modelling error experiment. Curves are perfectly overlain by one another. RMS error is 0.0042.

This experiment shows that by using two different methods to generate dispersion curves, errors in the inversion are to be expected. Modelling error is to be expected, especially with field data, as the data are acquired over real geology in real conditions. These errors can be mitigated slightly, but are still present.

3.5 Conclusion

In this chapter, I have introduced the forward and inverse modelling techniques that will be utilized throughout the rest of this thesis. The Marquardt-Levenberg least-squares inversion procedure was described. Modelling error, which arises because the forward modelling of dispersion curves is conducted in different ways such as field vs calculation vs finite-difference, was described and quantified with a simple experiment.

Chapter Four: Synthetic Data Tests and Validation

4.1 Introduction

Once a method or process is proposed and devised, the first step in testing and validating it should be applying it to synthetic data generated over a known model. In this chapter, the methods for characterizing the near surface proposed in the previous chapters will be tested on synthetic data. The shear wave velocity inversion will be tested on synthetic layered models, both laterally homogeneous and with lateral heterogeneities. The development of the processing workflow for poorly sampled data will be discussed and applied to a synthetic data set.

4.2 Layered model

The first test will consist of simulating wave propagation over a laterally homogeneous, vertically layered near surface model. A very simple two-layer model was tested in section 3.4, and the inversion was proven to converge to the true model. Here, more layers will be added to the model to test the resolution of the method, and its capability to handle multiple layers. The model parameters are listed in Table 4-1, and the model is shown in Figure 4-1.

Table 4-1 Layered model parameters.

	Thickness (m)	Depth (m)	Vp (m/s)	Vs (m/s)	ρ (g/cc)
Layer 1	10	0	1300	250	1.7
Layer 2	6	10	1400	300	1.8
Layer 3	4	16	1500	400	1.8
Layer 4	10	20	1600	500	1.8
Layer 5	10	30	1900	600	1.9
Layer 6	10	40	2000	650	2.0
Layer 7	10	50	2100	725	2.1
Halfspace	∞	60	2200	800	2.2

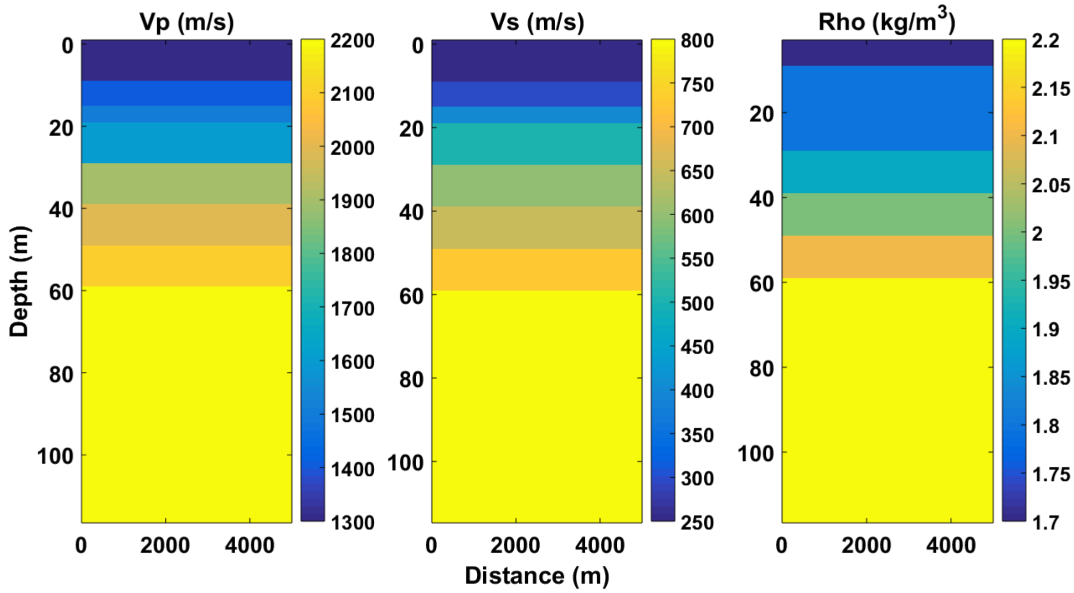

Figure 4-1 Layered model.

Wavefield propagation is simulated over this model using SOFI2D, after which the dispersion caused by the near surface layers may be examined. Receivers are placed at 2 m intervals, buried at 5 m depth. An explosive point source is placed at receiver depth at the centre of the model. The generated shot record is shown in Figure 4-2. With a 2 m receiver spacing, there are no aliasing or sampling issues in the data, allowing direct calculation of the dispersion spectra, which is shown in Figure 4-3. I can observe the <5 Hz frequencies of the dispersion curve trending to much higher velocities than are included in the model. This is due to mode interference of body waves at low frequency. By picking the curve so that it intersects the high amplitude energy at ~700 m/s, the dispersion curve is representative of the model used to generate it.

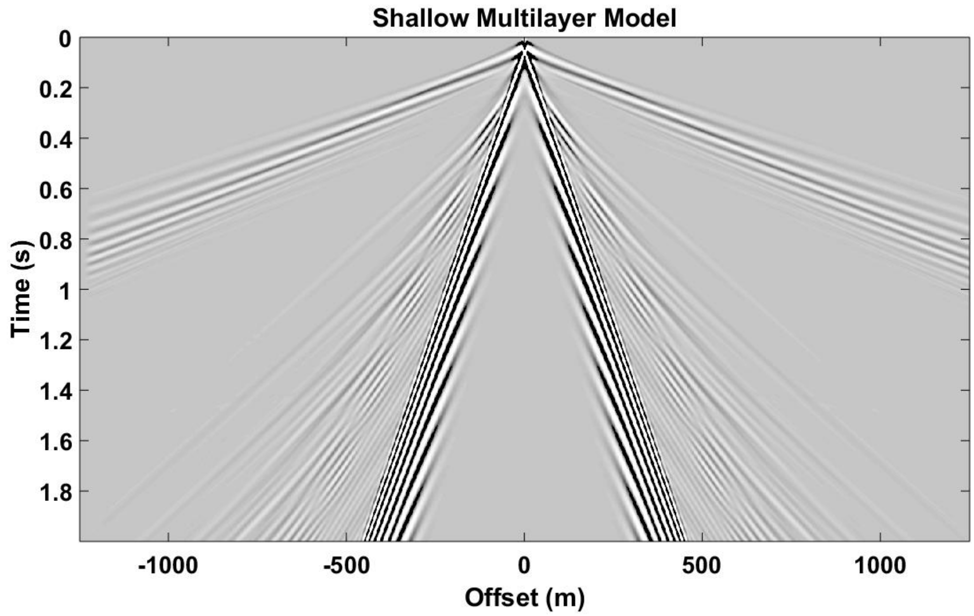

Figure 4-2 Shot record generated over the near surface layered model.

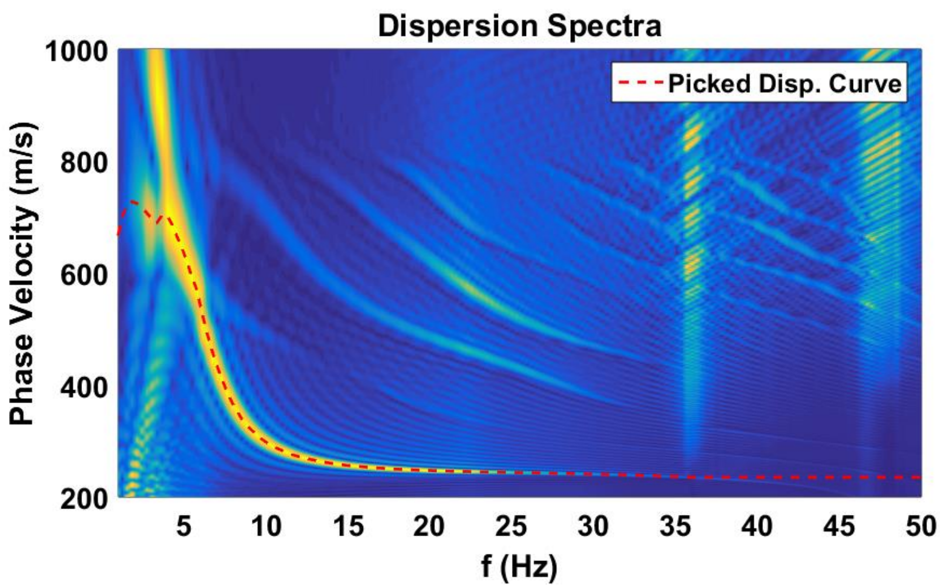

Figure 4-3 Dispersion spectra generated from the above shot record.

4.2.1 Shear wave velocity inversion

From the dispersion curve, near surface shear wave velocities can be inverted for, as discussed in Chapter 3. For the first test, layer depths will be assumed known. Initial model velocities will be predicted from the dispersion curve, as per 3.3.1. The residual is minimized after 5 inversion iterations. The observed and inverted dispersion curves are shown in Figure 4-4a. Note the very good match, except at <5 Hz due to uncertain pick. The velocity inversion results are shown in Figure 4-4b, showing a very close velocity inversion result at most layers. The 60 m depth layer predicts a lower than real velocity, again due to error in the low frequency dispersion curve pick.

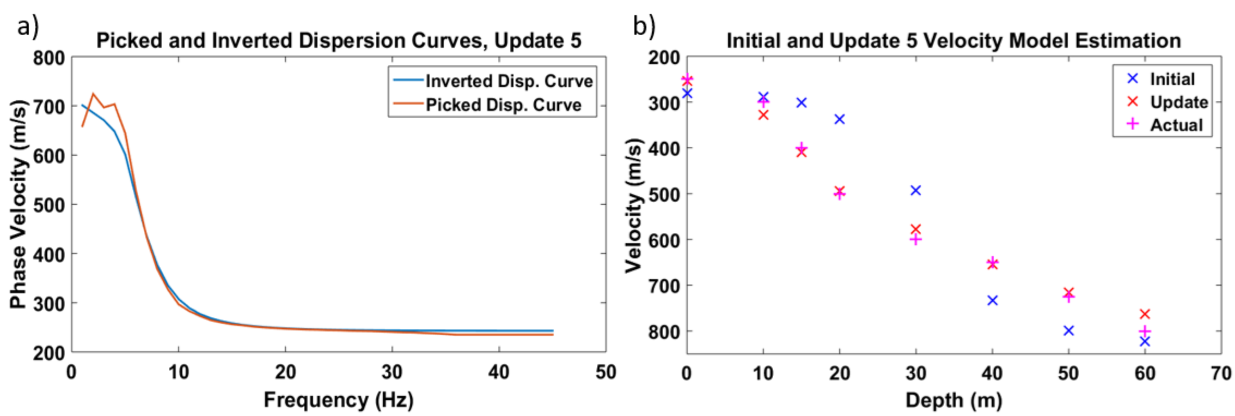

Figure 4-4 Inversion results for layered model. a) Observed and inverted dispersion curves. b) Velocity inversion results.

In this case, since it is known that the model is laterally homogeneous, the inversion will not be repeated using shot records from different surface locations. The above 1D velocity profile is extended to 2D, and linearly interpolated in depth between points to produce a 2D velocity profile, shown in Figure 4-5.

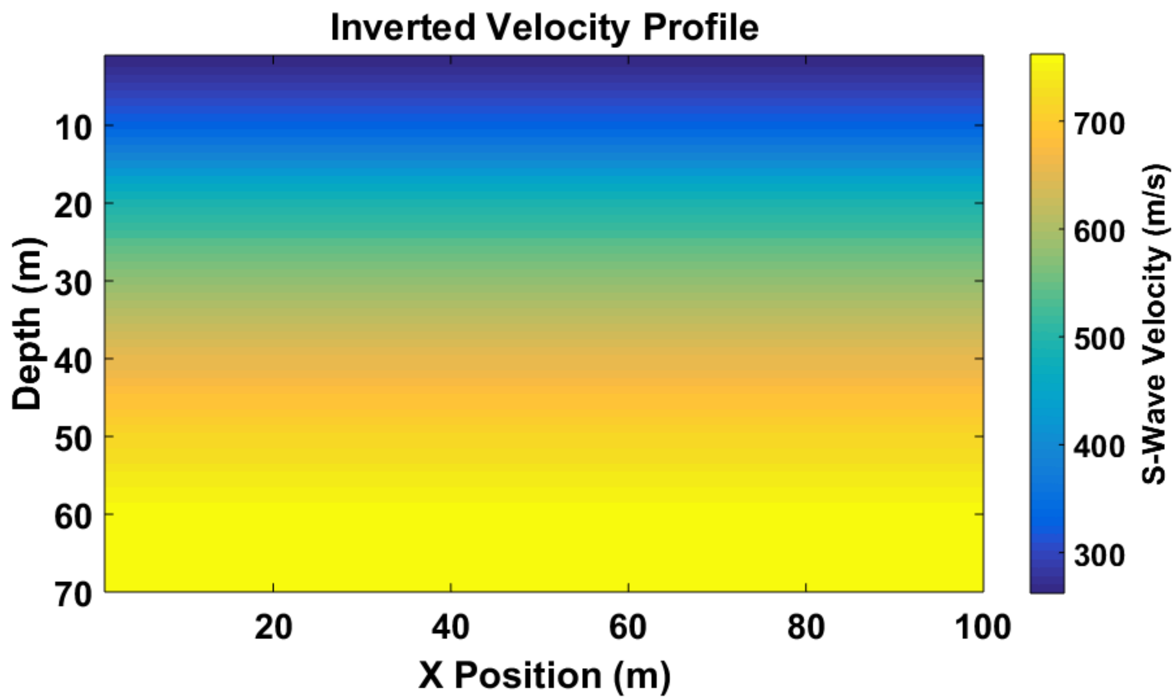

Figure 4-5 2D Shear wave velocity model from inversion.

For the second test, layer depths will be treated as unknown, and depths will be predicted from the dispersion curve. Recall that the inversion initialization is not predicting the layer boundary depths, rather it is predicting the velocity at a point in depth. The dispersion curve match resulting from the inversion is not as close as observed above, particularly at low frequencies, but still reasonable (Figure 4-6a). Because of the rapid change in phase velocity over few frequency points at low frequencies, it is difficult to predict accurate depths in the deeper section. As a result of this, the inversion struggles to match the dispersion curves in this interval.

Due to the depth prediction differences, the velocity inversion points will not lie at the same depths as the actual layer velocities. Rather, a depth window around each point should be considered, to gauge the accuracy of the inversion result. The predicted layer velocities are not exactly correct (Figure 4-6b), but most lie within an acceptable range. Points at 20 to 40 m depths overpredict the velocity, but the halfspace velocity is predicted correctly (albeit at a greater depth). Due to the rapid increase in phase velocity at low frequency, some depths (40-80 m) are unsampled in the inversion.

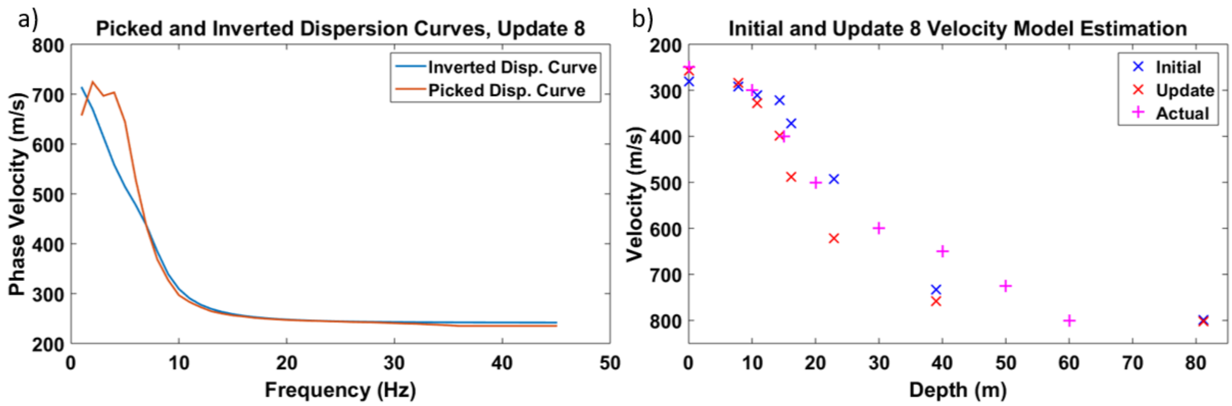

Figure 4-6 Inversion results for layered model, unknown depths. a) Observed and inverted dispersion curves. b) Velocity inversion results.

Again, this 1D profile can be extrapolated to 2D, shown in Figure 4-7, and compare it to the actual velocity model (Figure 4-1) and the known depths inversion result (Figure 4-4). In this case, velocities are slightly under-predicted at each depth, giving the effect that the velocity model as a whole was shifted upwards to shallower depths compared to the original model.

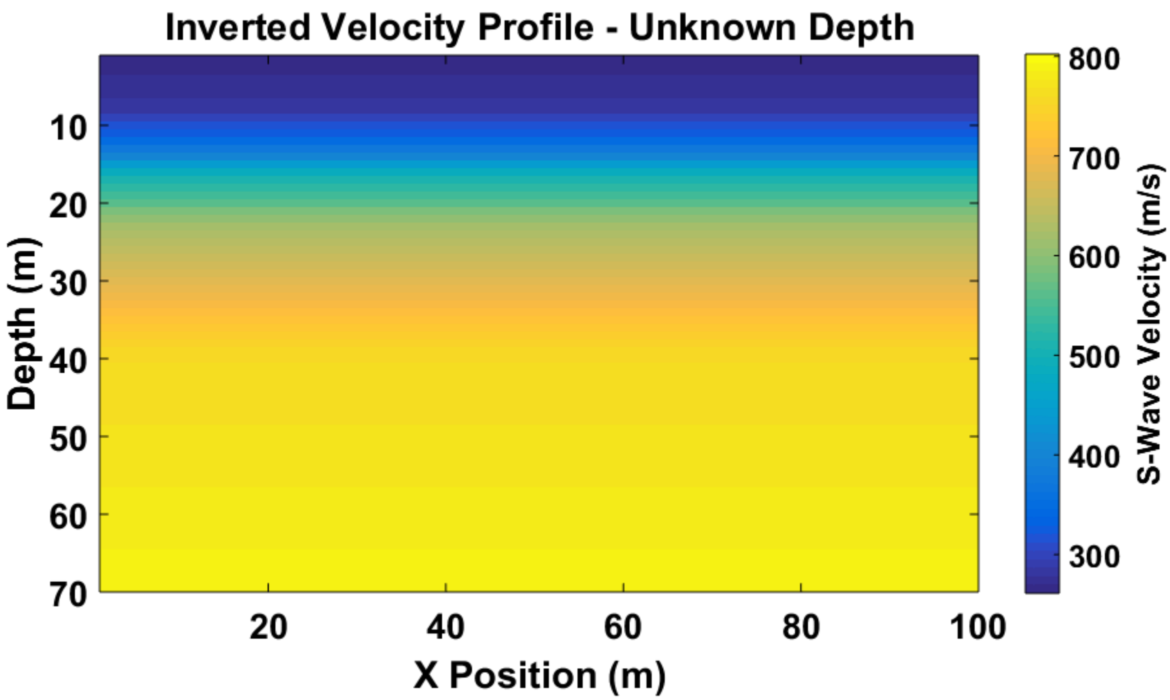

Figure 4-7 2D Shear wave velocity model from inversion, with unknown depths.

From this example, the benefit that knowing layer depths provides can be clearly seen. When depths are known, velocity inversion results are very good. When depths are unknown, the inversion suffers from non-unique solution issues, where multiple depth and velocity models may be valid solution. Reducing the uncertainties going into the inversion allows greater accuracy of the result which are of the most interest, shear wave velocities.

4.3 Laterally heterogeneous model

Now the effect that lateral heterogeneity has on dispersion curve generation and shear wave velocity inversion will be investigated. The model used (Figure 4-8) consists of a layered near surface, with a vertical discontinuity at the centre of the model, at x = 1000 m. The model parameters on the left had side of the model are the same as the homogeneous model above. On the right had side, velocities are 100 m/s faster than the layer to the left.

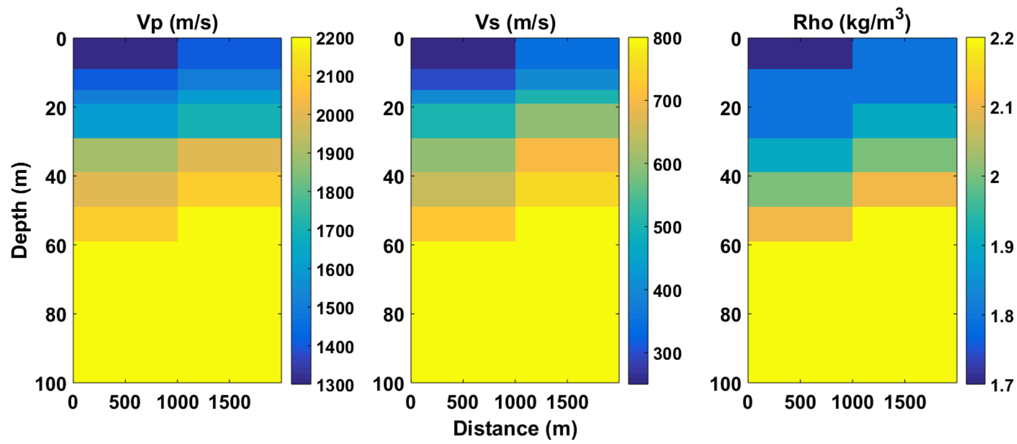

Figure 4-8 Layered model with lateral heterogeneity.

Sources are modelled at various locations along this model, using the same parameters as in 4.2. Source points at regular intervals along this model will be analyzed to determine the influence of the discontinuity on the dispersion curves. The shot record modelled at x=1000m, on the discontinuity, is shown in Figure 4-9. Note the asymmetry due to different velocities either side of the source. Because of this, dispersion curves generated from positive and negative offset data are different (Figure 4-10). The difference in minimum shear wave velocity is immediately obvious when comparing these two curves. Curiously, the low frequency portion of the curves are very different, when they both share a maximum Vs of 800 m/s. This could be due to mode-kissing interference, which has different patterns on each of these plots. These plots show how an "uncontaminated" dispersion spectra look for each side of this model.

These spectra can now be compared to those generated from source points on either side of the discontinuity. Source points were modelled every 100 m along the model, and dispersion spectra were generated from positive and negative offset data at each of these points. How the discontinuity affects dispersion is observed by looking at how the spectra change as the source approaches the boundary (Figure 4-11).

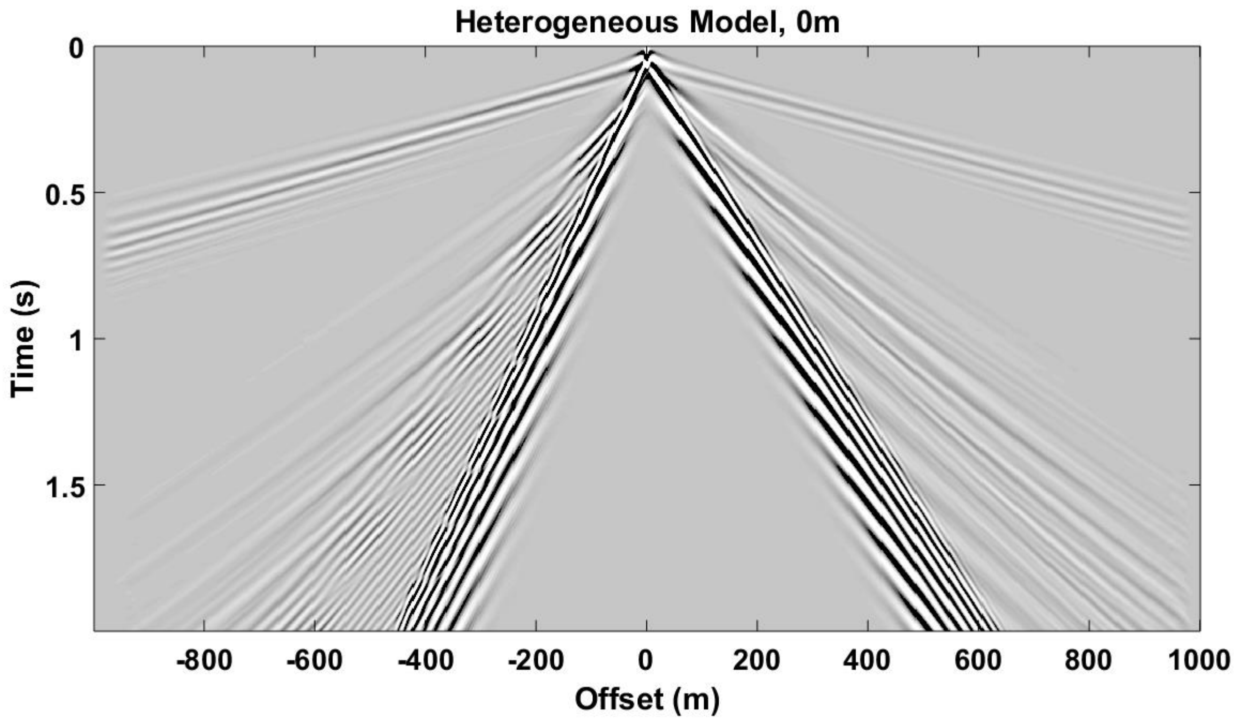

Figure 4-9 Shot record generated over heterogeneous model. Source at 0m, on the discontinuity. Note the asymmetry in ground roll arrivals.

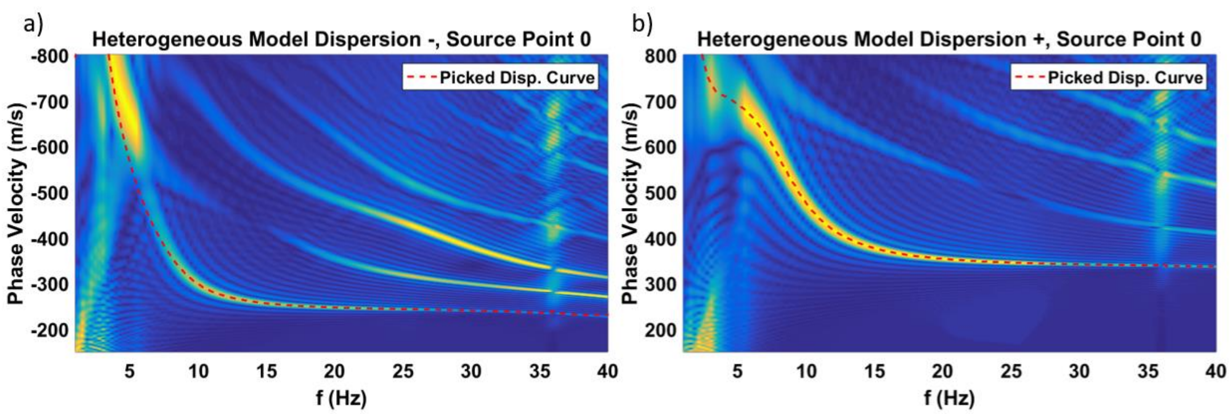

Figure 4-10 Dispersion spectra for 0m source point. a) Negative offsets. b) Positive offsets.

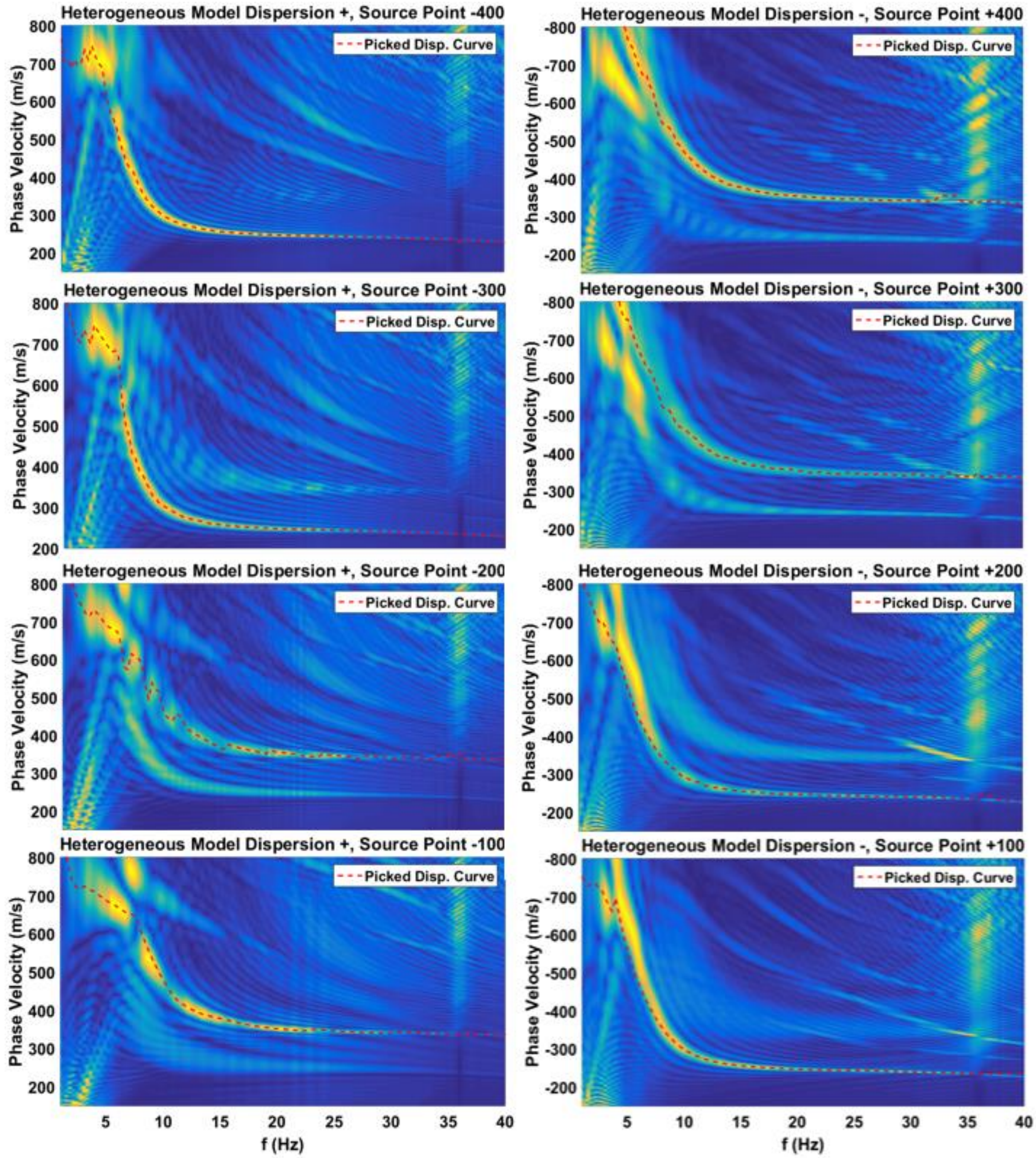

Figure 4-11 Dispersion spectra for source points approaching the discontinuity. Left: sources on the left-hand side of the model. Right: Sources on the right-hand side of the model. Top: Sources offset 400m from the centre. Bottom: Sources offset 100m from the centre.

In the above Figure 4-11, the far side of the model causes a "ghost" dispersion curve, beginning at 300 m offset. At 200 m offset from the discontinuity, this "ghost" curve is the higher amplitude event, and is therefore picked as the dispersion curve for that shot record. This means that any velocity inversion performed using these ≤ 200 m offset curves will produce a 1D velocity profile characterizing geology over 200 m away. This is not unreasonable since the dispersion curve is created from, and representative of, a window of ground roll data covering hundreds of metres. Interference of the two dispersion curves at low frequencies is also observed, particularly at 200 to 300 m offset from the discontinuity. This will cause inversion errors for deeper layers. It must be kept in mind, however, that this is noise free synthetic data, exhibiting only geometric attenuation, so the useful window of ground roll in field data will likely be much smaller. Park et al. (1999) discusses the far offset effect, where body waves begin to contaminate high frequency components of the spectrum at high offsets. This isn't observed in this data due to the nature of the modelling. When this method is applied to field data, considerations of what offset ranges are represented in the dispersion curves will need to be made.

4.3.1 Shear wave velocity inversion

In all the examples in this section, I will assume that layer depths are known. The inversion accurately predicted velocities for geology 200 m away from the source point. Due to the sharp contrast at x = 1000 m, there was limited blending of dispersion curves, which could be expected for a smoother transition. An example of this is shown in Figure 4-12, where the x = 800 m source point inversion results are shown. Here it can be seen that the inverted velocities in the left-hand panes are converging on the velocities from the left side of the model, as expected, and the right-hand pane velocities are converging on the velocities from the right-hand side of the model, 200 m away from the source. Based on this determination, that observed dispersion curves are representative of geology over 200 m away from the source, inverted 1D shear wave velocity profiles will be place 215 m away from the source for which they are generated.

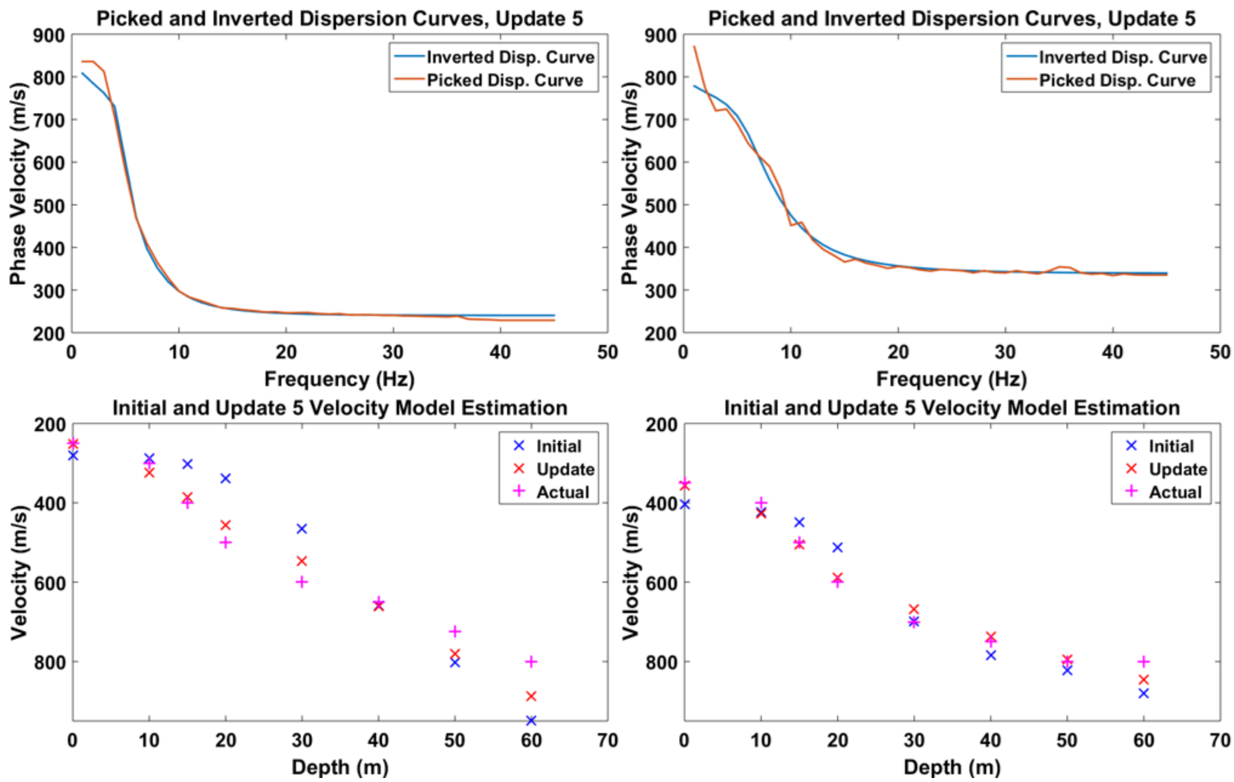

Figure 4-12 Inversion results for the source point at x=800m. Left: Negative offset results. True velocities from left side of model. Right: Positive offset results. True velocities from right side of model.

Performing the shear wave velocity inversion for positive and negative offset data generated at every source point, a 2D velocity profile over the model can be generated, shown in Figure 4-13. In this profile, vertical high velocity bands are visible at regular intervals. These are caused by dispersion curve picking uncertainties at low frequency, again likely due to mode-kissing interference. An example is visible in the top-right window of Figure 4-11. More precise curve picking would remove these bands, however there would still be uncertainty about the true velocities, unless the true model is known, as in this case.

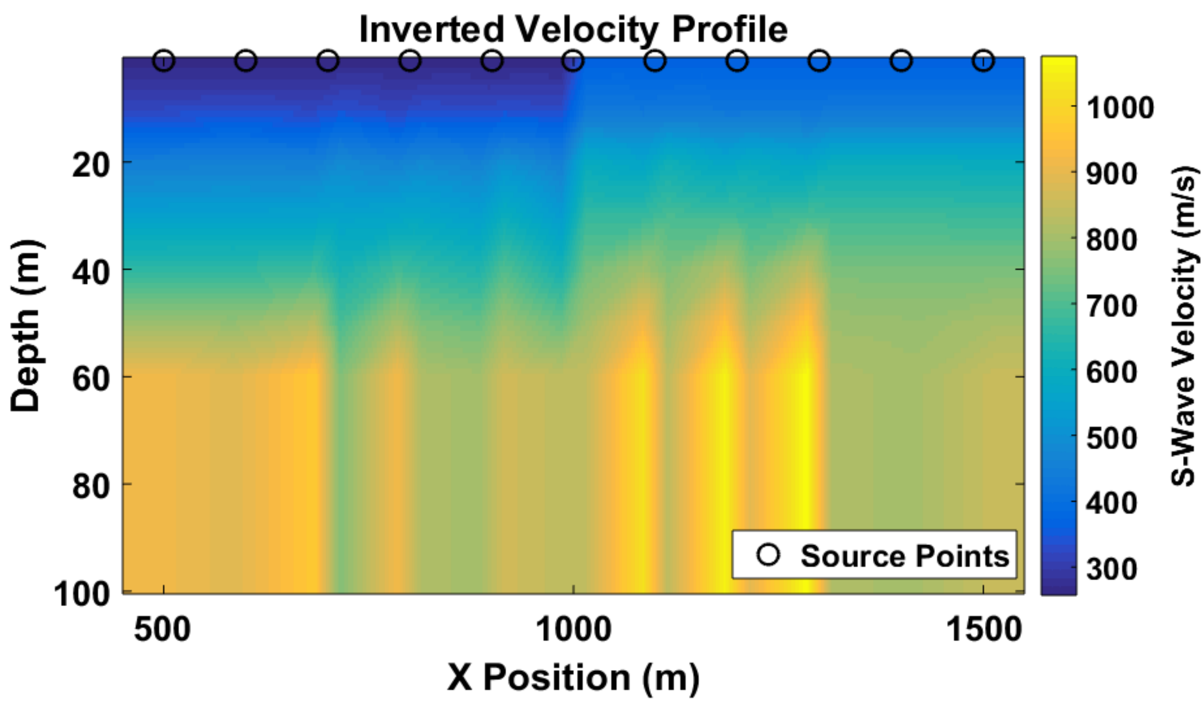

Figure 4-13 2D inverted shear wave velocity model. Discontinuity at x=1000m is clearly visible.

In this example, a known geologic model was examined, and because it's exact parameters are known, an accurate velocity inversion was produced. In cases where the geology is unknown, like most field data, it would not be possible to draw the same conclusions about what offset is most represented by generated dispersion curves. In these cases, much more uncertainty would be present in the inverted model.

4.4 Processing workflow

For data sampled at greater distances than a typical MASW survey (~2 m receiver spacing), additional processing is required to produce resolvable dispersion curves. To develop the processing workflow introduced in Chapter 2, trials were conducted using synthetic data sampled at exploration seismic survey scale. A more detailed description of the procedure is covered in Mills and Innanen (2016b).

The model used for this test is shown in Figure 4-14. The model consists of a complex near surface in the shallowest 100m, including a vertical discontinuity at the centre of the model, offsetting the three near surface layers, with three deeper layers to a maximum reflector depth of 1510 m. Receivers were spaced at 20 m over long offsets, to test the interpolation and filtering techniques discussed. The source is located at receiver depth, on the discontinuity. Because of this, asymmetry can be expected in both the shot record and in the dispersion curves at positive and negative offsets. This shot record generated from this model, shown in Figure 4-15, contains reflection events, which are dimly visible, direct arrivals and refractions, and high amplitude ground roll as the most steeply dipping arrivals. It is from the tau-p data that the dispersion spectra are created, so it is beneficial to have clear data in the tau-p domain. There are a number of details obfuscating the ground roll components of this data, as shown in Figure 4-16. The events labelled “noise” are caused by aliasing in the ground roll. The aliasing arises due to the low sampling rate, and the tau-p transform views the aliasing as events in the seismic. Through interpolation and FK filtering, I will attempt to filter and remove these parts of the data, enhancing the signal from the ground roll.

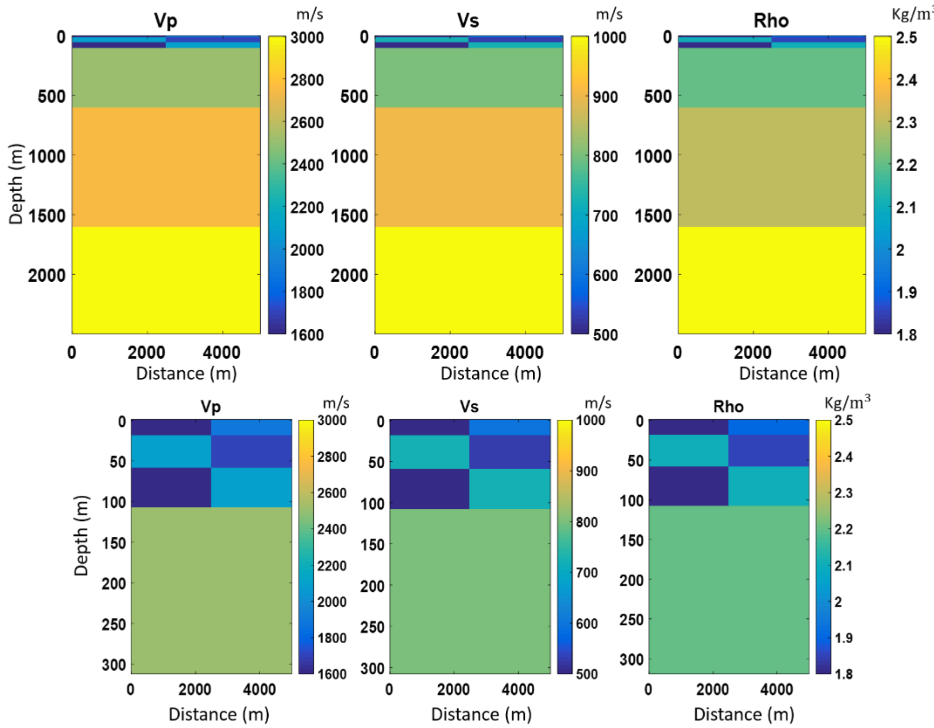

Figure 4-14 Geologic model used to test processing flow. Top: Full model. Bottom: Near surface zoom.

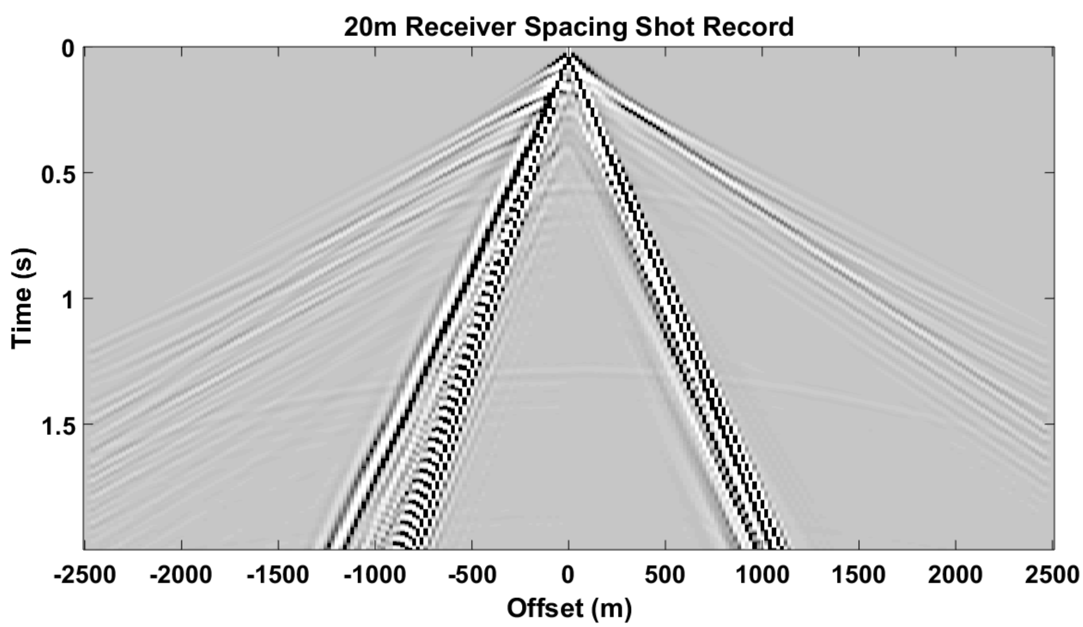

Figure 4-15 Shot record generated over above model.

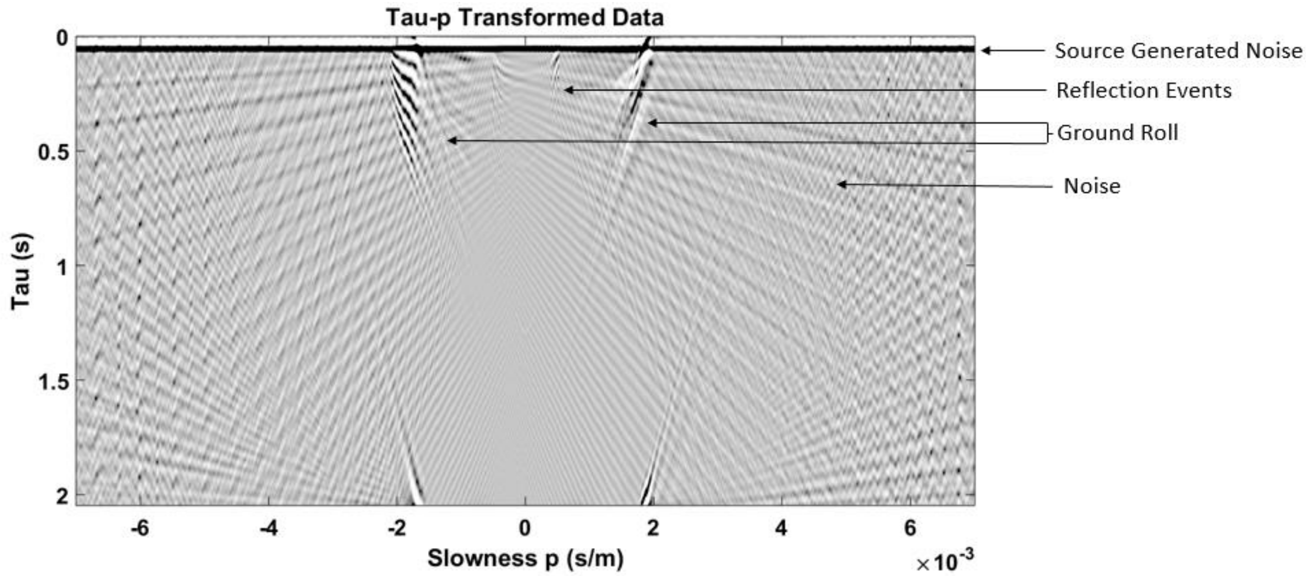

Figure 4-16 Shot record in Tau-p domain, with events labelled.

Because the shot is in the centre of the asymmetric model, with different model properties on either side of the shot, the dispersion spectra consists of two different components. These are shown in Figure 4-17, where the top curve represents positive offset data (Positive phase velocity) and the bottom curve represents negative offset data (Negative phase velocities. Velocity is positive, but in the negative x direction). In these dispersion spectra, the fundamental mode is quite visible to 30 Hz, however there is substantial noise crossing the curve, possibly interfering with our ability to pick it accurately. The most dispersive portion of the curve is clearly visible for this example, but the noise could be an issue for other models.

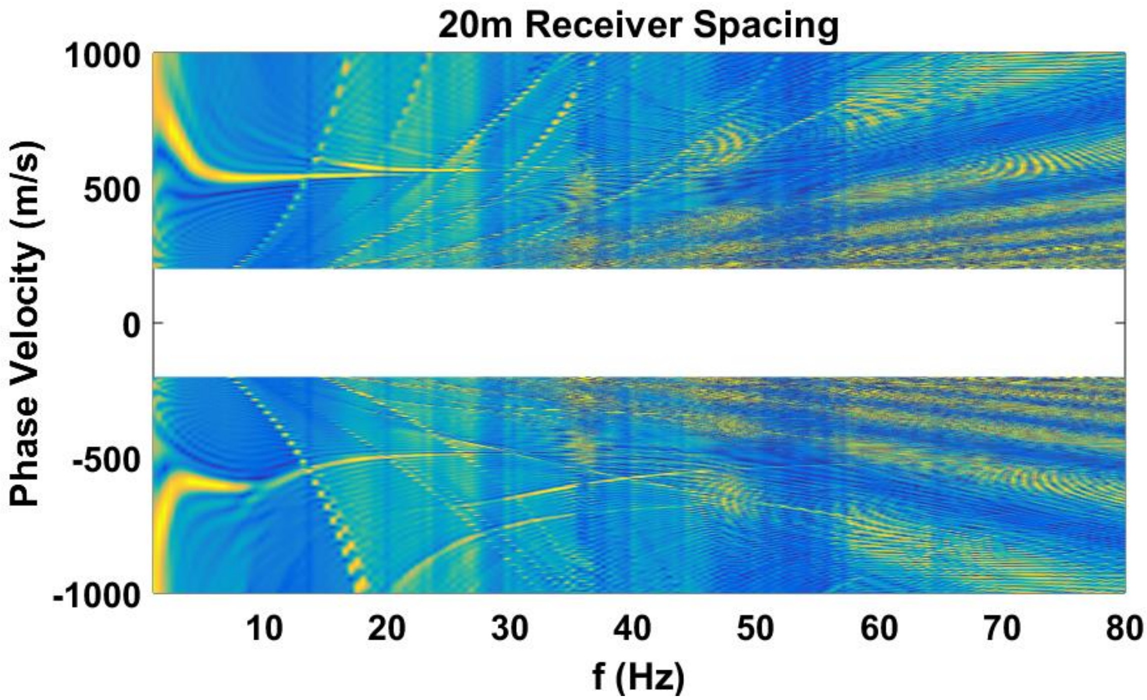

Figure 4-17 Dispersion spectra generated from the above data. Top: Positive offset dispersion. Bottom: Negative offset dispersion.

Since I am interpolating to a smaller receiver spacing sampling rate, above figures (shot record, tau-p data, and dispersion spectra) will be re-generated at an equivalent 10 m receiver spacing to have a standard to compare to. The shot record and tau-p data are shown in Figure 4-18. Note the reduction in aliasing related noise relative the ground roll components in this tau-p plot. As a result of this aliasing reduction, a reduction in noise in the dispersion spectra is also observed, shown in Figure 4-19.

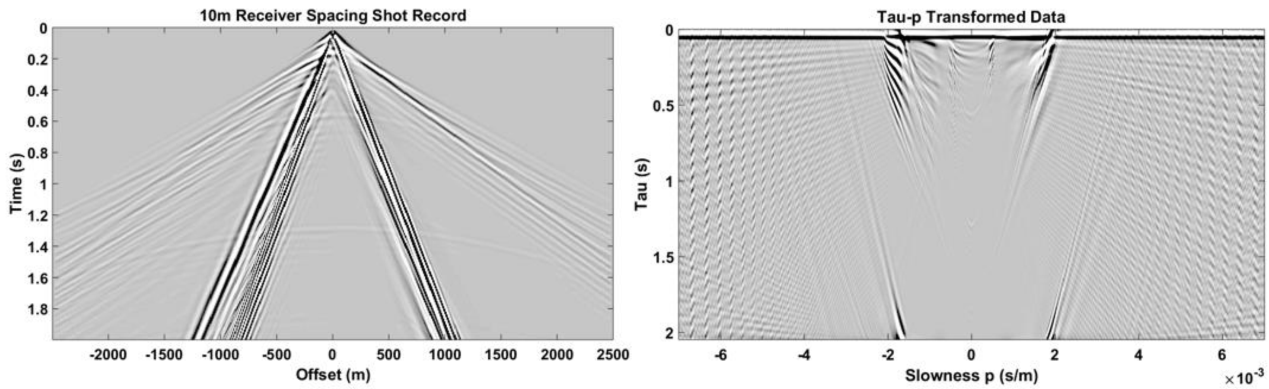

Figure 4-18 Left: 10m receiver spacing shot record. Right: Tau-p data.

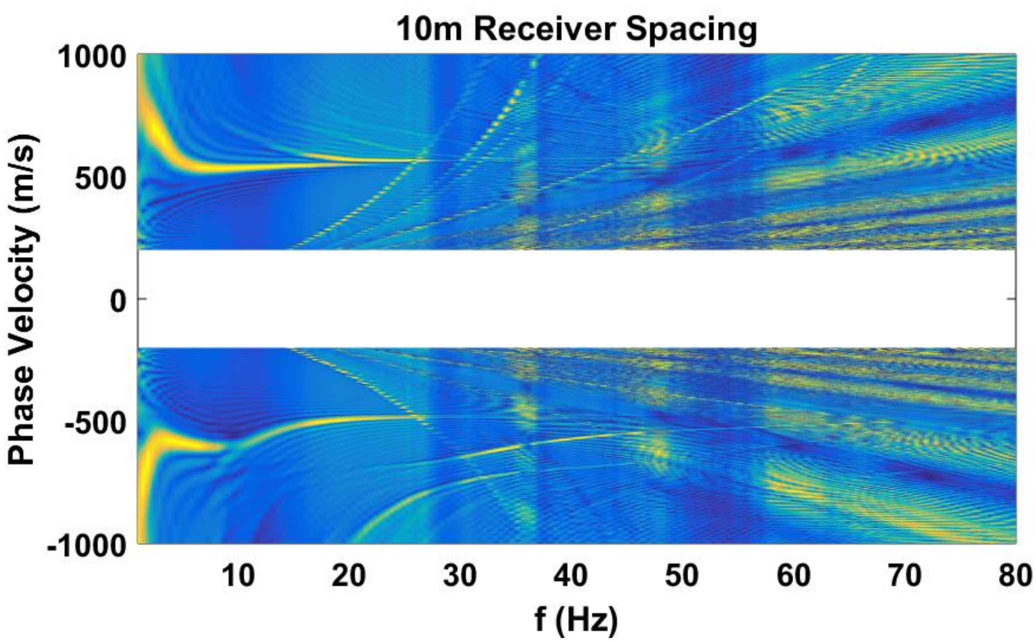

Figure 4-19 Dispersion spectra generated from the above data. Top: Positive offset dispersion. Bottom: Negative offset dispersion.

4.4.1 Processing

In the original development of these methods, two workflows were tested. In the first, FK filtering was applied, followed by interpolation. The purpose of FK filtering was to reduce aliasing, and remove reflections and refractions in the data. The resulting dispersion spectra from this method was found to be improved over the original 20 m receiver spacing dispersion, however data was obscured by a high amplitude noise band from 20-35 Hz, where it wasn't originally (Mills and Innanen, 2016). This was determined to be caused by the FK filtering, which filtered aliased data that also contained ground roll dispersion information. This reduced the amplitude of the ground roll at these frequencies relative to remaining noise in the data. Because of this, it was proposed to interpolate to 10 m receiver spacing first, then FK filter the resulting data.

With this method, the interpolated ground roll signals (Figure 4-21) are nearly a perfect match to the original (Figure 4-20), with only slight amplitude differences. The main issue is the incorrect interpolation of reflection events in the centre of the shot record. This is due to these events not being flattened by the LNMO shift before interpolation, resulting in a time shift and amplitude error after interpolation and reverse LNMO correction.

This shot record is then FK filtered, removing remaining aliasing, as well as most of the reflections and their poor interpolations, shown in Figure 4-22. From this, I can generate the dispersion spectra, which are shown in Figure 4-23. I can compare this spectrum to the original 10 m sampled data spectra in Figure 4-19, and see that the fundamental mode curves are equally resolvable below 35 Hz. Below 35 Hz, the dispersion curve is clear, unobstructed, and uncrossed by other events. The curves are continuous and traceable to 35 Hz, and are even brighter from 30-35 Hz than in the original.

This demonstrates that with the above processing, the quality of dispersion spectra produced from data with twice as dense receiver spacing can be met, and even exceeded. With further interpolation and filtering, it is likely these spectra can be improved even further to match those generated with tighter receiver spacing.

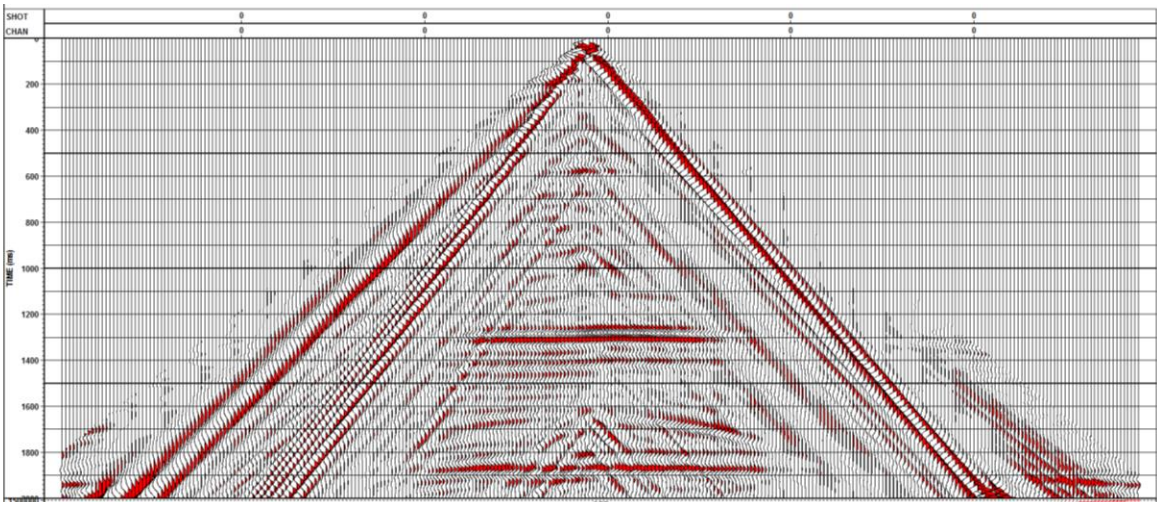

Figure 4-20 Original 10m receiver spacing shot record. Generated in Vista

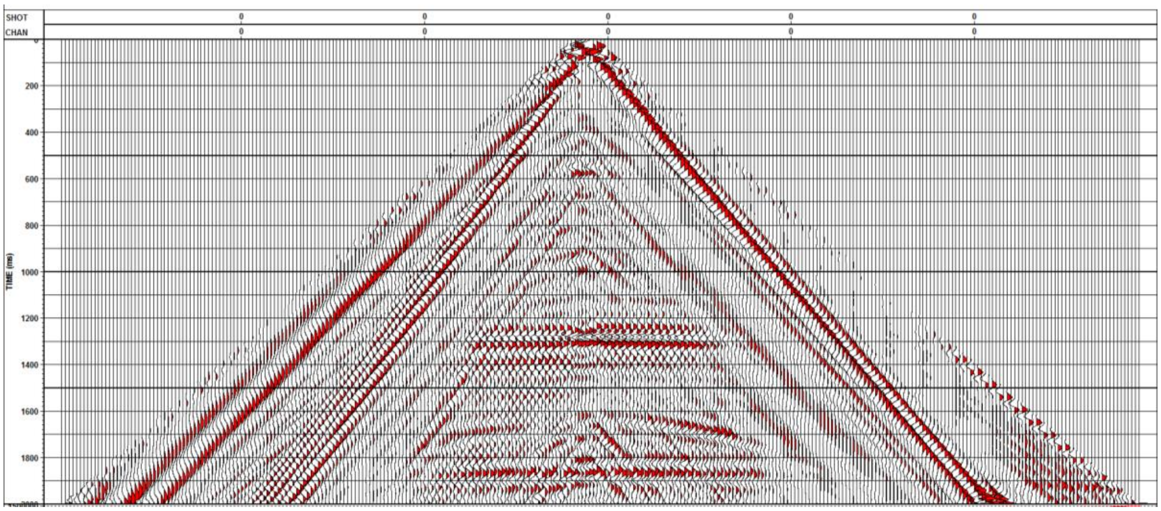

Figure 4-21 20m receiver spacing data interpolated to 10m. Note similarities in ground roll character to the original 10m sampled data in Figure 4-20. Generated in Vista.

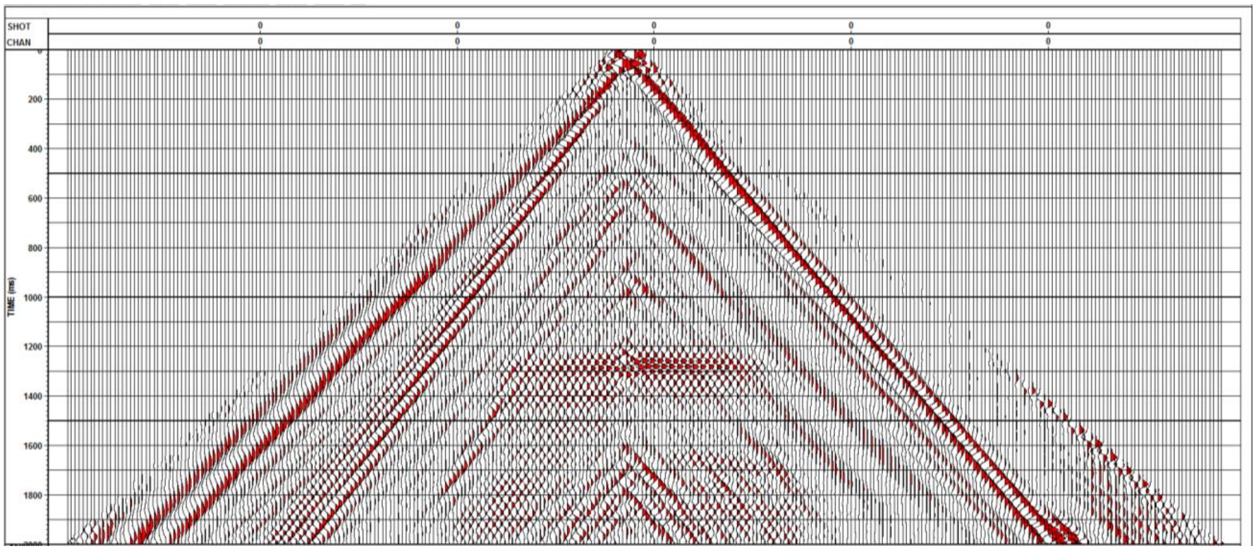

Figure 4-22 Interpolated data after FK filtering. Generated in Vista.

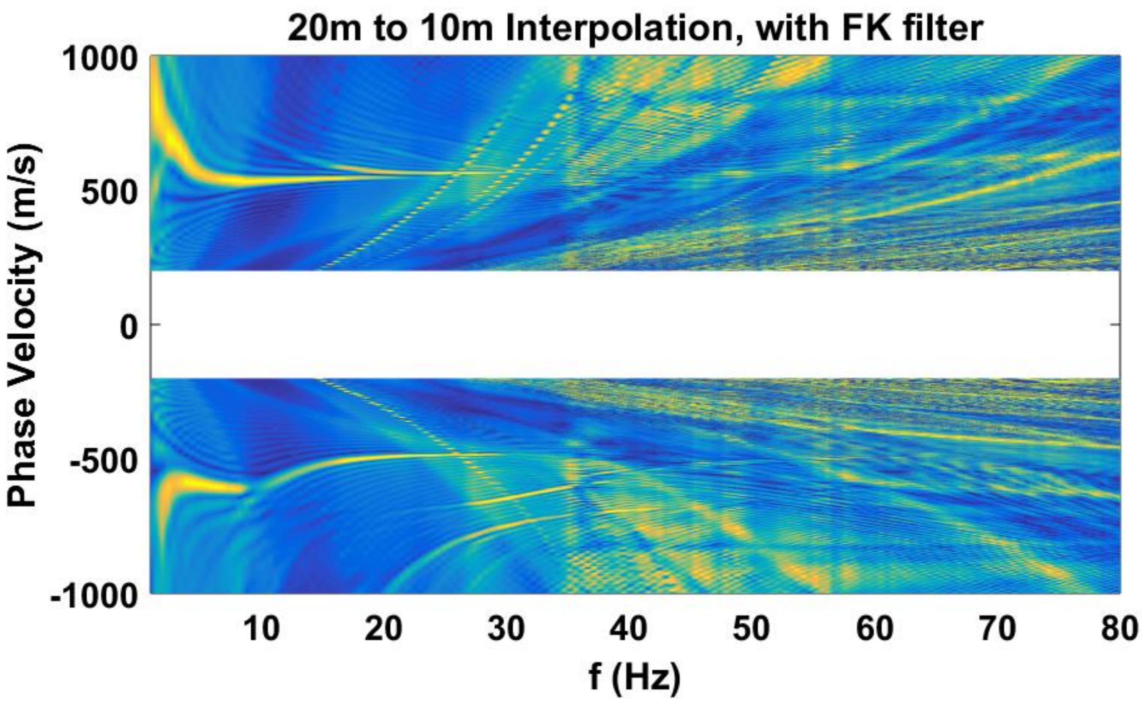

Figure 4-23 Dispersion spectra for interpolated and FK filtered data.

4.5 Conclusion

In this chapter, the shear wave velocity inversion was tested on synthetic data generated over layered models. In cases where layer depths are known, the inversion converges to the correct velocities. In cases where depths are unknown, depths are predicted from the dispersion curve. Velocities inverted at these depths are within range of true values, but some depths may be unsampled. A model with a vertical discontinuity at the centre was tested, and it was found that dispersion curves were representative of model parameters at distances over 200 m away from the source point. Placing the 1D inverted velocity profiles at these offsets produced accurate velocity models. The processing workflow for data acquired with large receiver spacing was discussed and tested on a synthetic data set. Correct application of this workflow was found to produce dispersion spectra with similar resolution to those produced from data with tighter receiver spacing.

Chapter Five: Case Study 1 – Priddis Thumper Experiment

5.1 Introduction

Once a method has been tested and validated on synthetic data, it must be proven to work on field data. In fall 2016, CREWES conducted a thumper seismic experiment at the University of Calgary's field research location, on the property of the Rothney Astrophysical Observatory 25 km SW of downtown Calgary. In this chapter, I will be testing the methods developed in earlier chapters on this field data set. Due to the acquisition parameters, which are on a slightly larger scale than a typical MASW survey, this is a good first test of the method.

5.2 Thumper experiment

The purpose of this field experiment was to test the remote controls for the thumper source, and to acquire multicomponent VSP data, along with near-offset seismic data. It was not designed with near surface characterization in mind. The source used is the CREWES thumper, a multi-component accelerated weight drop source (Lawton et al., 2013). A 100 kg hammer is accelerated by compressed nitrogen, with pressures adjustable from 500 to 2000 psi. The hammer can impact the ground at vertical incidence as a P-wave source, or at ± 45 degrees for generating P and S-waves simultaneously, shown in Figure 5-1. Data was recorded using all three source orientations, however only the vertical incidence records are used in the research summarized in this chapter.

Data are recorded over a 200 m long seismic line, with 40 10 Hz, 3 component geophones spaced at 5 m (Figure 5-2). Data are also recorded in a vertical well at the South end of the line, but this is not used in this study. Unfortunately, the shallowest 30 m of sonic well log measurements in this well are inaccurate due to poor cement in this interval. 2 shots are taken at each source location, which are 2 m to the East of the receiver positions. Compared to an ideal

MASW survey, this experiment is over a receiver line twice as long (100m typical), with more than double the receiver spacing (2m typical), using 10 Hz geophones rather than lower frequency (4.5 Hz or lower) receivers. The length of the receiver line shouldn't be an issue for applying MASW techniques, and the receiver spacing can be handled using interpolation as described in section 2.4.2. The geophone frequency will limit the depth of investigation; however, the data will still yield information about the shallow near surface.

Figure 5-1 CREWES Thumper source. Shown in S-wave generating mode, at 45° incidence.

Figure 5-2 Field location map. Source locations marked with X and source point number.

The shot records from the source points at the ends of the receiver lines are shown in Figure 5-3 (145, South end) and Figure 5-4 (139, North end). AGC has been applied to these shot records for viewing. The ground roll is the dominant high amplitude signal. In both plots, the average velocity of the Rayleigh waves is ~215 m/s. Slight asymmetry is visible in the records, particularly at near offsets in Figure 5-3, indicating lateral heterogeneities in the near surface.

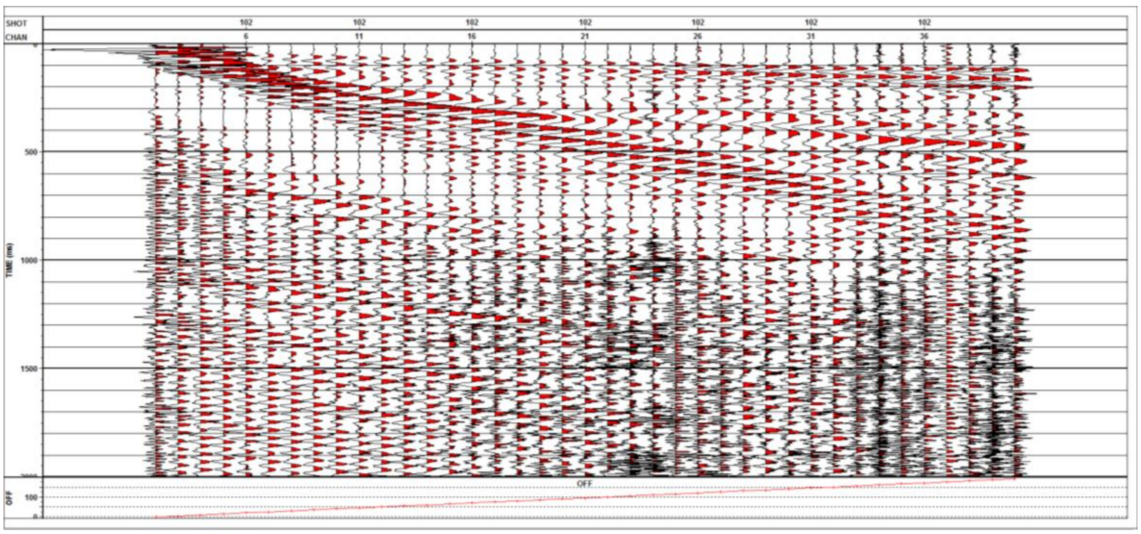

Figure 5-3 Shot 145, Source Point 101 at the South end of the line. AGC applied. Generated in Vista.

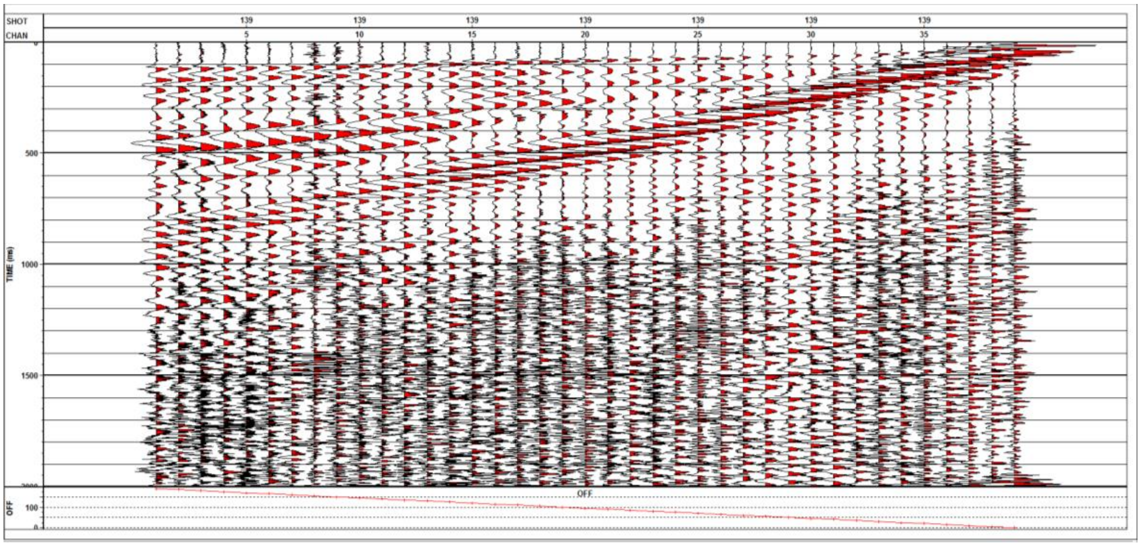

Figure 5-4 Shot 139, Source Point 139 at the North end of the line. AGC applied. Generated in Vista.

5.3 Data Processing and Dispersion Analysis.

Individual shot records are used for the analysis of the Priddis thumper data. Data are evaluated at five source locations, with 2 shots at each. The processing flow follows that described in section 2.3, Figure 2-7. Shot records generated at the same source point are stacked to reduce noise relative to the ground roll signal. The shot record is then LNMO corrected to flatten the ground roll events before interpolation. Interpolation is preformed twice in this case, resampling the data from 5 m to 1.25 m receiver spacing. The LNMO correction is then reversed, and the data are FK filtered to remove any remaining aliasing.

Once the shot records have been processed, dispersion curves can be generated for the positive and negative offset components of each record. The offset ranges available from each shot record are displayed in

Table 5-1. Offsets to the North of the source are denoted as positive. Despite up to 50 m of offset being available to the North of source point 131, and South of source point 111, it was found that this was insufficient for generating pickable, usable dispersion curves. Park et al. (1999) states that Rayleigh waves can only be treated as horizontally travelling plane waves after they have propagated at least half of their maximum wavelength (λ_{max}). Below this distance, lower frequencies lack linear coherency. This is observed in the dispersion spectra for the South offsets of source point 111 Figure 5-5, where the fundamental mode dispersion curve loses coherence below 20 Hz. For this reason, only data with ≥~100 m of offset will be used to generate dispersion curves from which Vs will be inverted for.

Table 5-1 Offset ranges for each station seismic record.

Station #	Shot #	Positive (N) Offset (m)	Negative (S) Offset (m)
139	139, 140	5	195
131	115, 116	45	155
121	85, 86	95	105
111	55, 56	150	50
102	145, 146	195	5

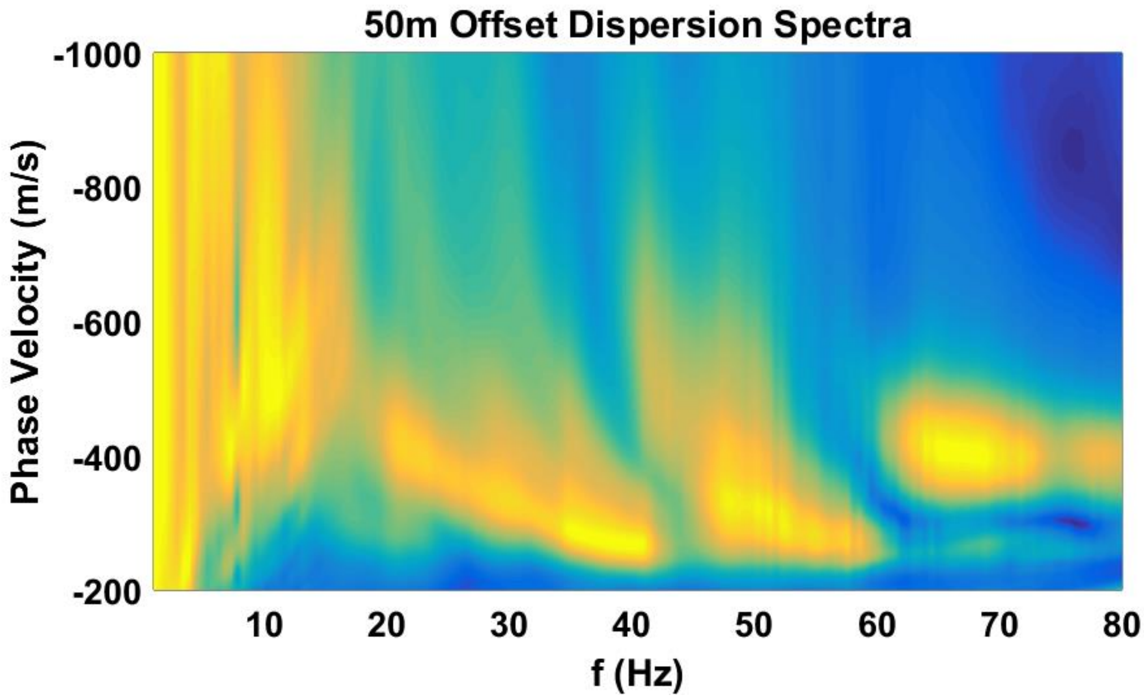

Figure 5-5 Dispersion Spectra generated from near offset (<50m) from station 111 (S). Observe the loss of coherency below 25Hz due to the near offset effect.

5.3.1 Source point 139

I will proceed with the dispersion analysis starting from the North end of the survey line. The shot record for shot 139 is shown above in Figure 5-4. The dispersion spectra generated from this raw record is shown in Figure 5-6. Here the fundamental mode curve can be seen clearly, however, there is a discontinuity in the curve at 40 Hz. Following the process outlined above, the interpolated and filtered record is shown in Figure 5-7, and from this, a better dispersion curve result can be achieved, shown in Figure 5-8. The curve is now continuous from 10-60 Hz. Dispersion information is unreliable below 10Hz, due to the bandwidth of the receivers used. Because of this, this inversion is limited to data above 10 Hz. Similar restrictions will be placed on the data at other source points, depending on their quality.

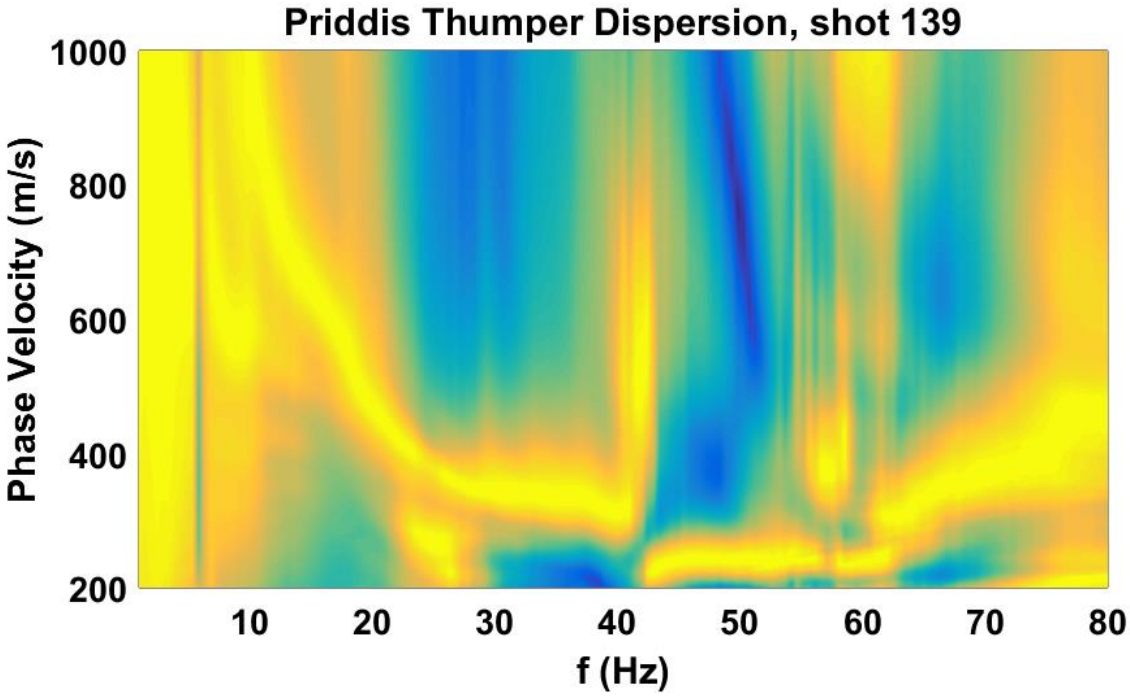

Figure 5-6 Dispersion spectra from shot 139. Note discontinuity in dispersion curve at 40Hz.

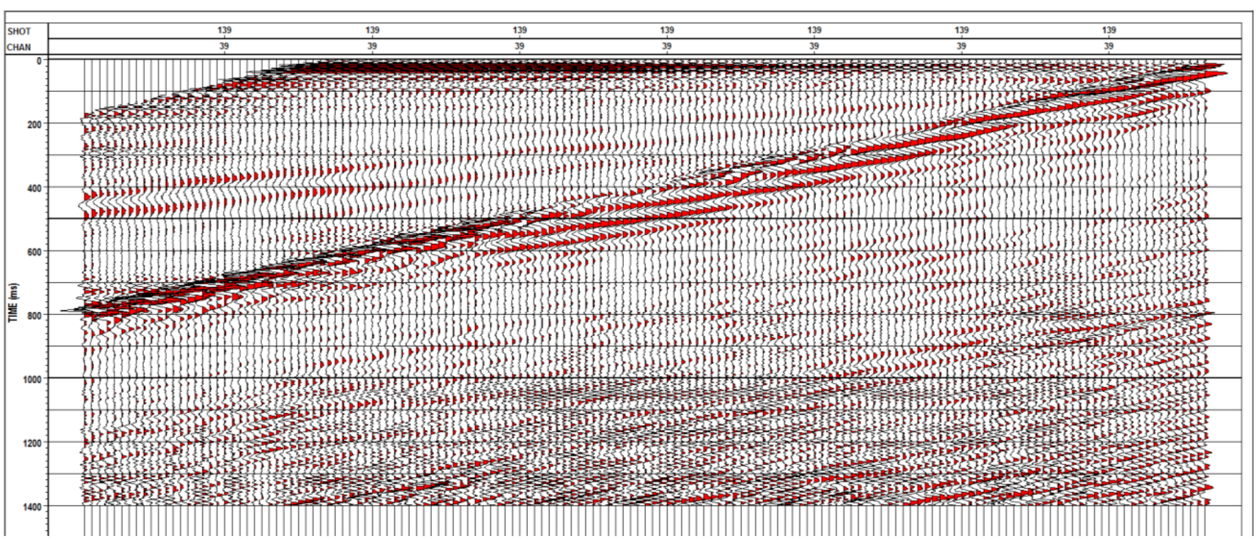

Figure 5-7 Source point 139 data interpolated to 1.25m receiver spacing. AGC applied. Generated in Vista.

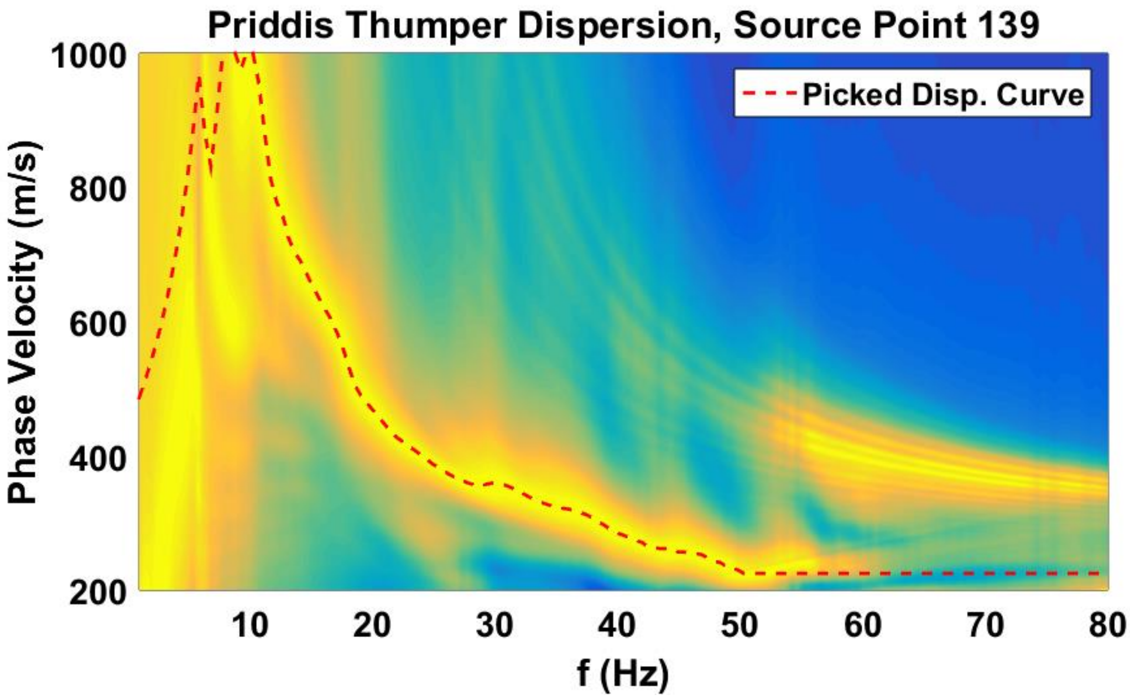

Figure 5-8 Dispersion spectra after processing. Picks are erroneous below 10Hz.

Proceeding with the shear wave velocity inversion, a 1D Vs profile can be generated from this dispersion curve, shown in Figure 5-9. 15 inversion iterations were run, at which point only marginal reductions in the residual were observed (Figure 5-11). An arbitrary number of layers (9) was chosen for the velocity model, based on the length of the dispersion curve. The half-space, or bedrock appears to be sampled at 22m depth, where the velocity profile flattens, showing only minor velocity variations. There is a roughly linear increase in Vs with depth from surface down to the bedrock. The measured and inverted dispersion curves are shown in Figure 5-10. Note the separation between 10-20 Hz, which is caused by several factors. First, the measured dispersion curve does not asymptotically approach an upper limit velocity due to the non-measurement of <10 Hz signal. Because of this, the inversion is attempting to match artificially high velocities at low frequencies. Second, the regularization is placing a priority on limiting the change in velocity from layer to layer. Without the regularization, the inversion predicts unreasonably high velocities at these deeper points. Third, the inversion predicts a smooth dispersion curve, so will try to match the curve as closely as possible at all points.

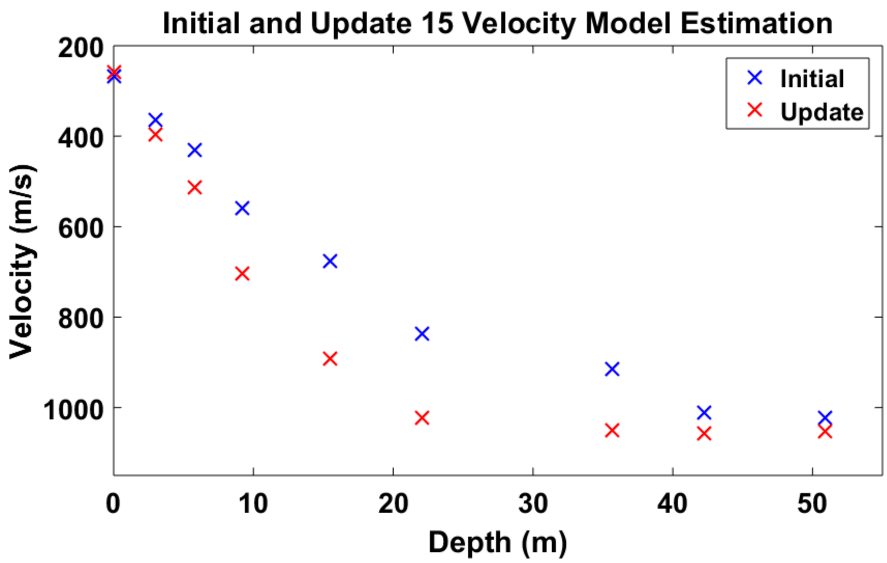

Figure 5-9 1D Shear wave velocity inversion results for source point 139.

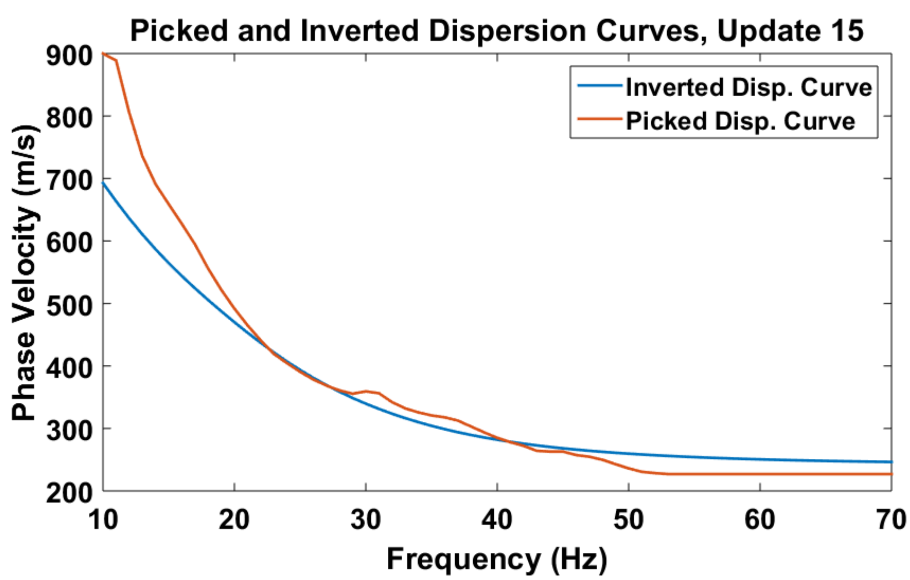

Figure 5-10 Dispersion curve inversion results for source point 139.

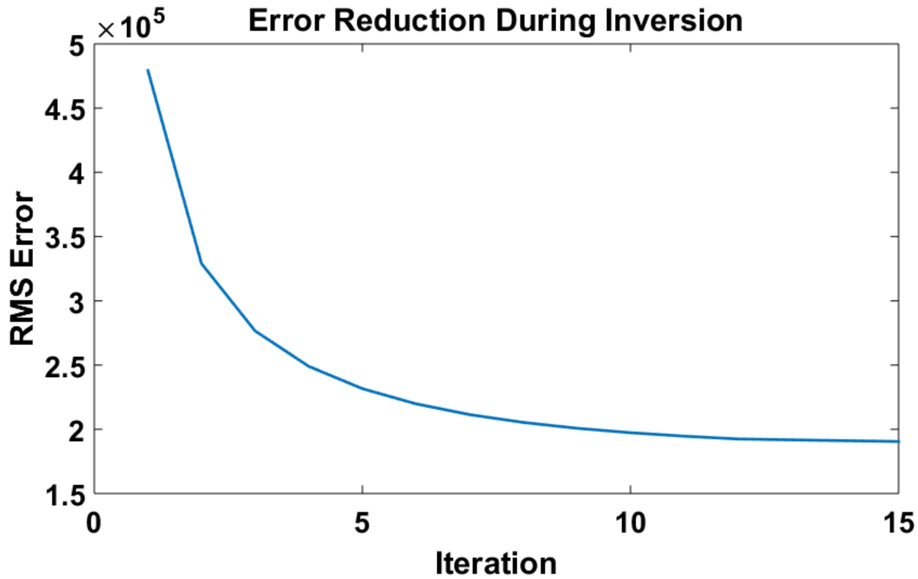

Figure 5-11 Residual reduction curve for source point 139.

5.3.2 Source point 131

Located approximately 50 m South of source point 139 is Source point 131. The same process applied to the source point 139 data is applied to the data acquired here, and the resulting shot record is shown in Figure 5-12. Note that only the data to the left of the source point (negative offsets) will be used for this location, due to the limited positive offsets. The dispersion spectra generated from the processed source point 131 records is shown in Figure 5-12. Similar to source point 139, dispersion trends are not visible below 10 Hz, and any dispersion curve picks below this are erroneous and excluded from the inversion.

Again, 15 inversion iterations were run to produce a 1D Vs profile at this location, shown in Figure 5-14c. Like source point 139, at 22 m depth the velocity model flattens at ~1020 m/s, suggesting this is the depth and shear wave velocity of the bedrock. Differences between the picked and inverted dispersion curves in Figure 5-14a arise from the same causes identified in section 5.3.1.

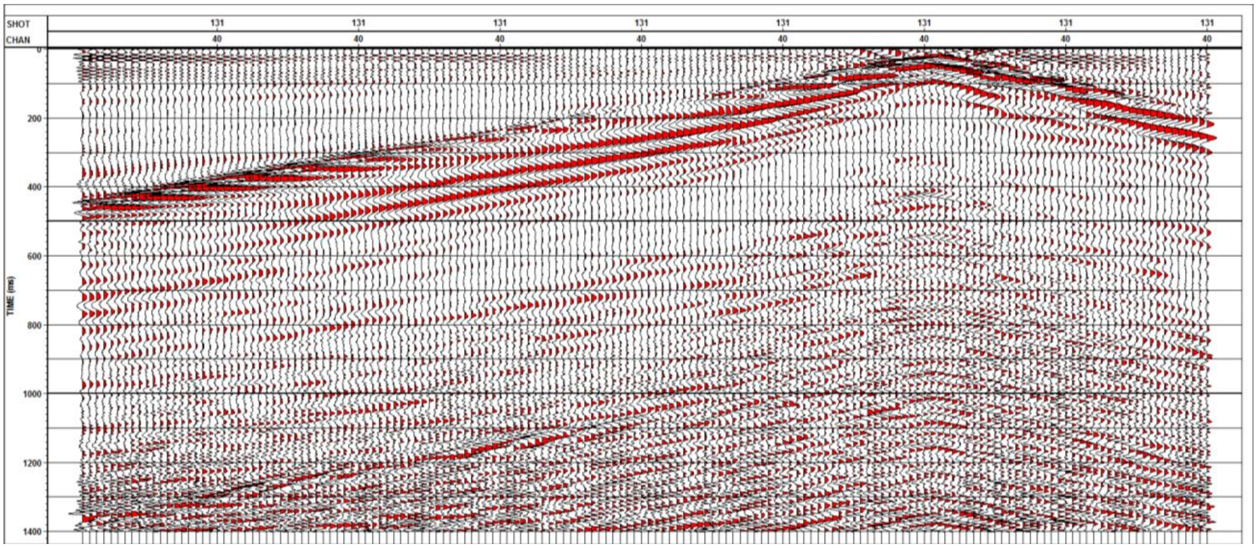

Figure 5-12 Source point 131 data interpolated to 1.25m receiver spacing. AGC applied. Generated in Vista.

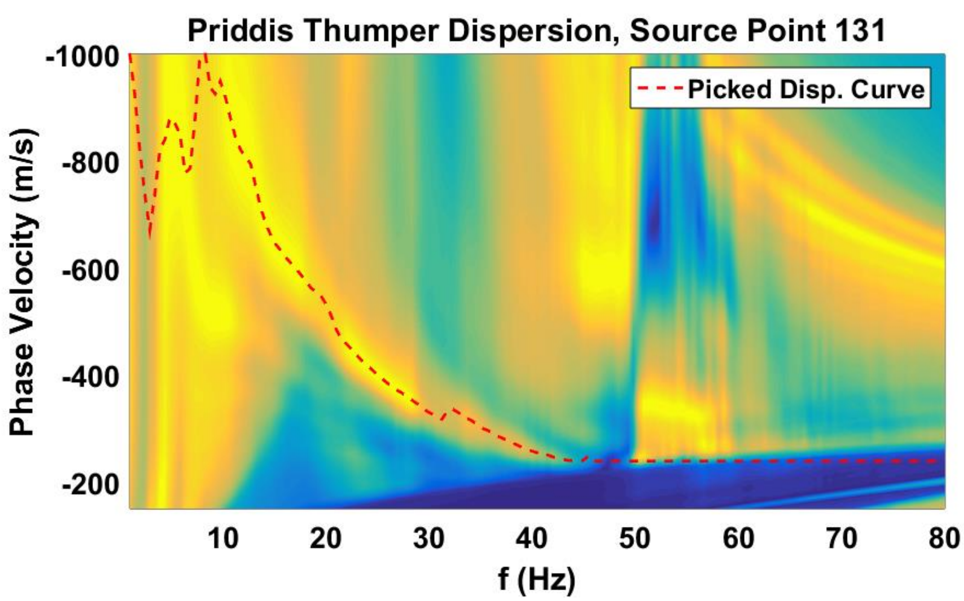

Figure 5-13 Dispersion spectra after processing. Picks below 10 Hz are erroneous.

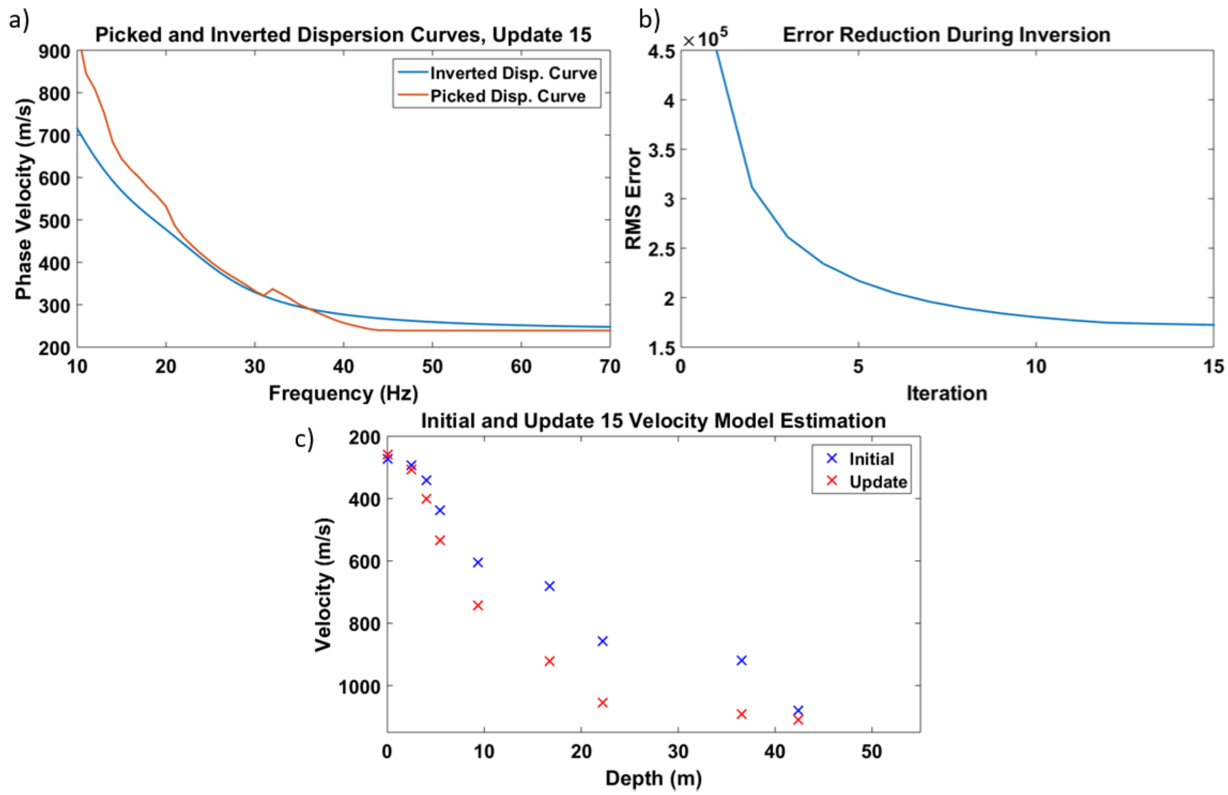

Figure 5-14 Inversion results for source point 131. a) Dispersion curve comparison. b) Residual reduction. c) Shear wave velocity model.

5.3.3 Source point 121

Source point 121 lies roughly at the centre of the survey line, with ~100 m offset of available data on both sides of the source. This station will contribute two velocity profiles, one from the positive offset data, and one from the negative offset data. The processed and interpolated data are shown in Figure 5-15. Analysis of this source point is split into positive and negative offset dispersion analysis. As can be seen in Figure 5-16, the dispersion spectra generated from the positive (b) and negative (a) offsets are quite different. At high (>50 Hz) frequencies in Figure 5-16a, the dispersion curve is interrupted, so is extrapolated straight out from the its value at 50 Hz, whereas in Figure 5-16b, the curve continues to decline past 50 Hz. This discrepancy will only affect the velocity prediction for the shallowest layers. For positive offsets, frequencies below 12 Hz are unsampled, versus 10 Hz for the negative offset data. Low frequency phase velocities are also much higher at positive offsets. For example, at 12 Hz, the phase velocity is 944 m/s at positive offset, while at the same frequency it is 687 m/s at negative offsets. As a result, it is likely velocities will be higher to the North of the source point.

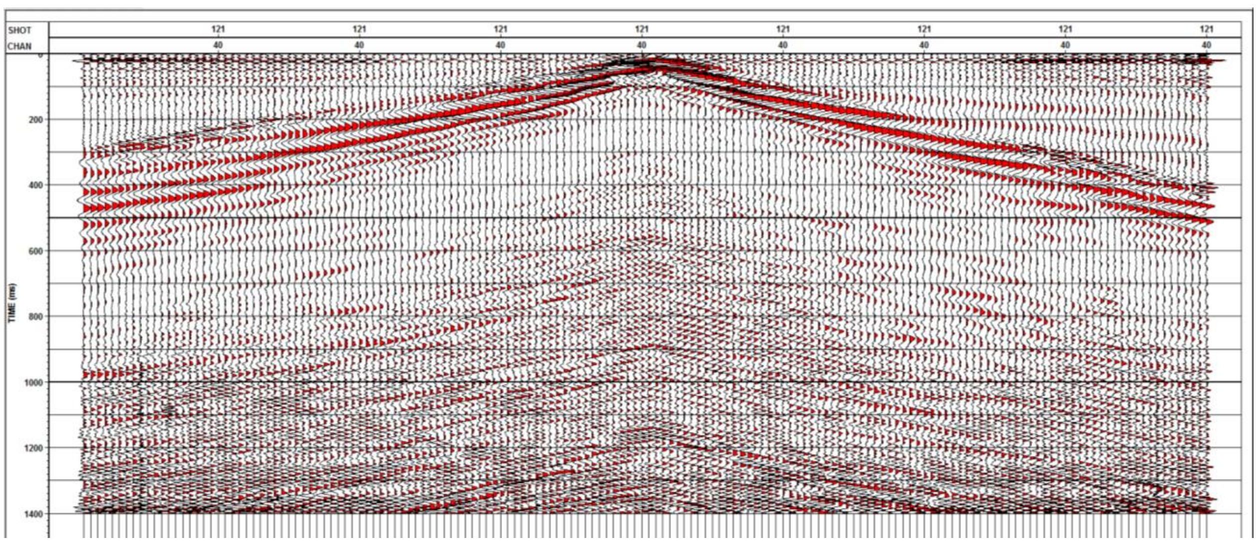

Figure 5-15 Source point 121 data interpolated to 1.25m receiver spacing. AGC applied. Generated in Vista.

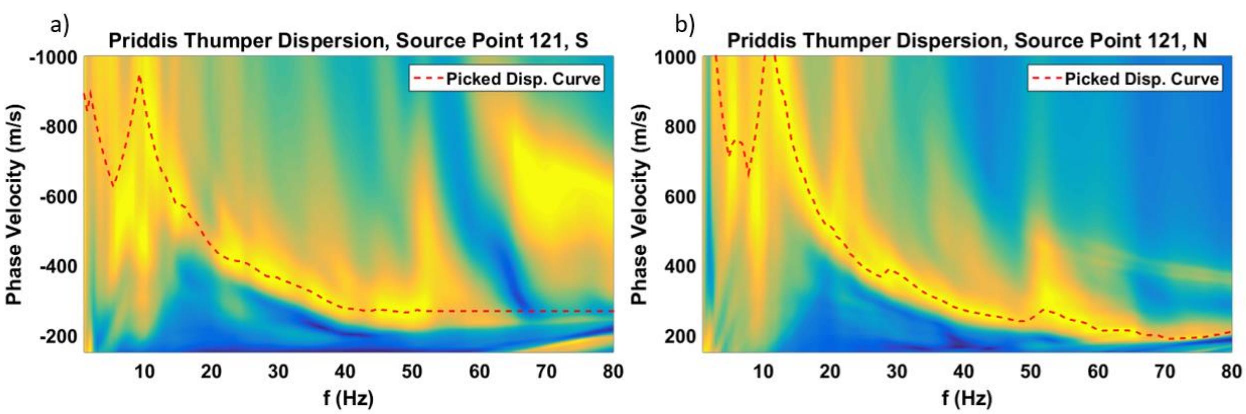

Figure 5-16 a) Dispersion spectra for negative offset data. b) Dispersion spectra for positive offset data.

For both the positive and negative offset data, 15 velocity inversion iterations were run. Positive offset data was limited to frequencies >12 Hz, and deeper velocities were unsampled as a result. However, below 20 m depth the velocity profile again flattens (Figure 5-17c), indicating that deeper strata is bedrock. Again, there is a gradational increase in velocity with depth in the shallower section.

The negative offset data was limited to frequencies >10 Hz, and again shows layers deeper than 20 m depth have approximately equal shear wave velocity (Figure 5-18b). As predicted from dispersion curves before the inversion, shallower layers have higher velocities to the North of the source point. At 10 m depth, the predicted Vs is ~750m/s to the North, while in the South the predicted velocity is ~100 m/s slower.

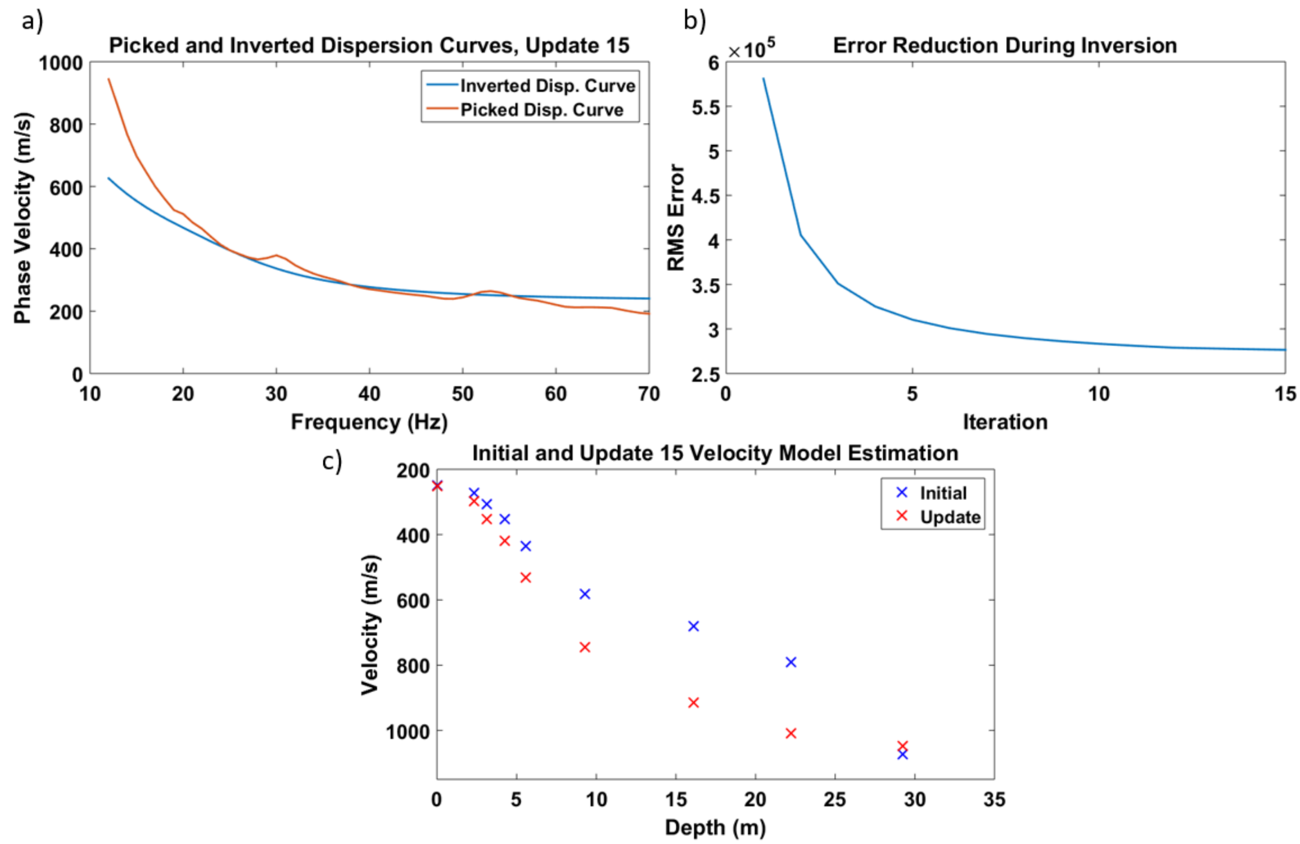

Figure 5-17 Inversion results for source point 121, North (positive) offsets. a) Dispersion curve comparison. b) Residual reduction. c) Shear wave velocity model.

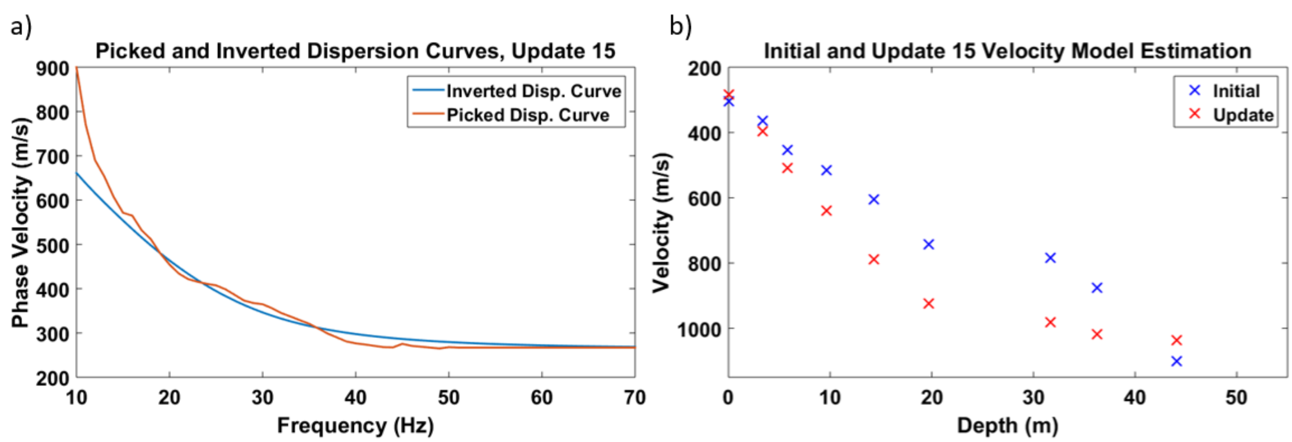

Figure 5-18 Inversion results for source point 121, South (negative) offsets. a) Dispersion curve comparison. b) Shear wave velocity model.

5.3.4 Source point 111

Source point 111 is 50 m North of the South end of the survey line, and will be used in the North offset velocity profile. The stacked and interpolated shot record is shown in Figure 5-19. Note that beyond ~100 m offset from the source, ground roll is incohesive. The dispersion spectra generated from this record is shown in Figure 5-20. The inversion results are shown in Figure 5-21, where again I observe a relatively linear increase in velocity with depth down to 20 m, where the profile flattens.

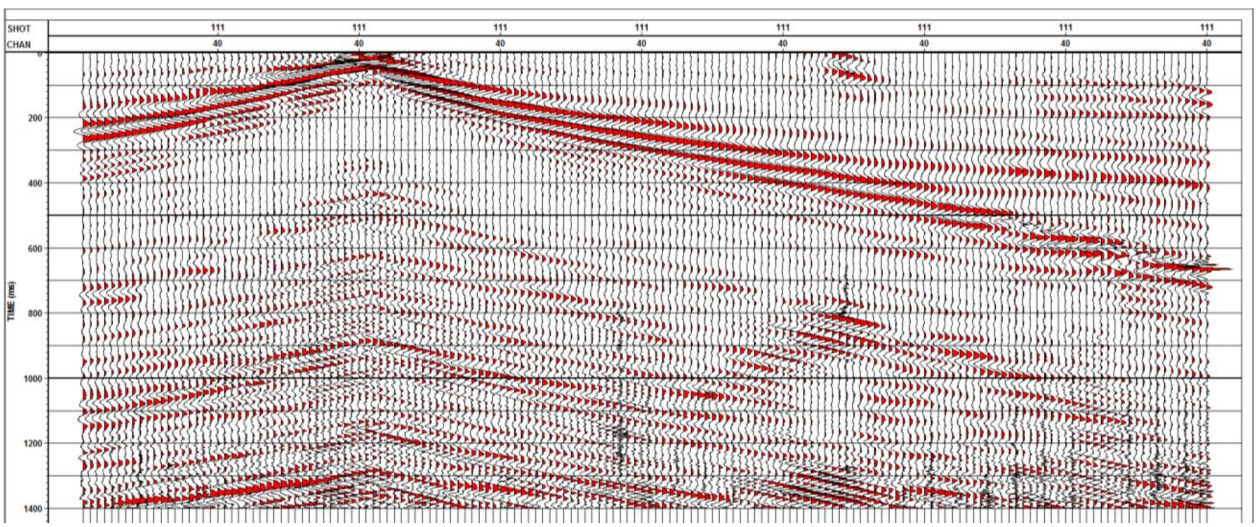

Figure 5-19 Source point 111 data interpolated to 1.25m receiver spacing. AGC applied. Generated in Vista.

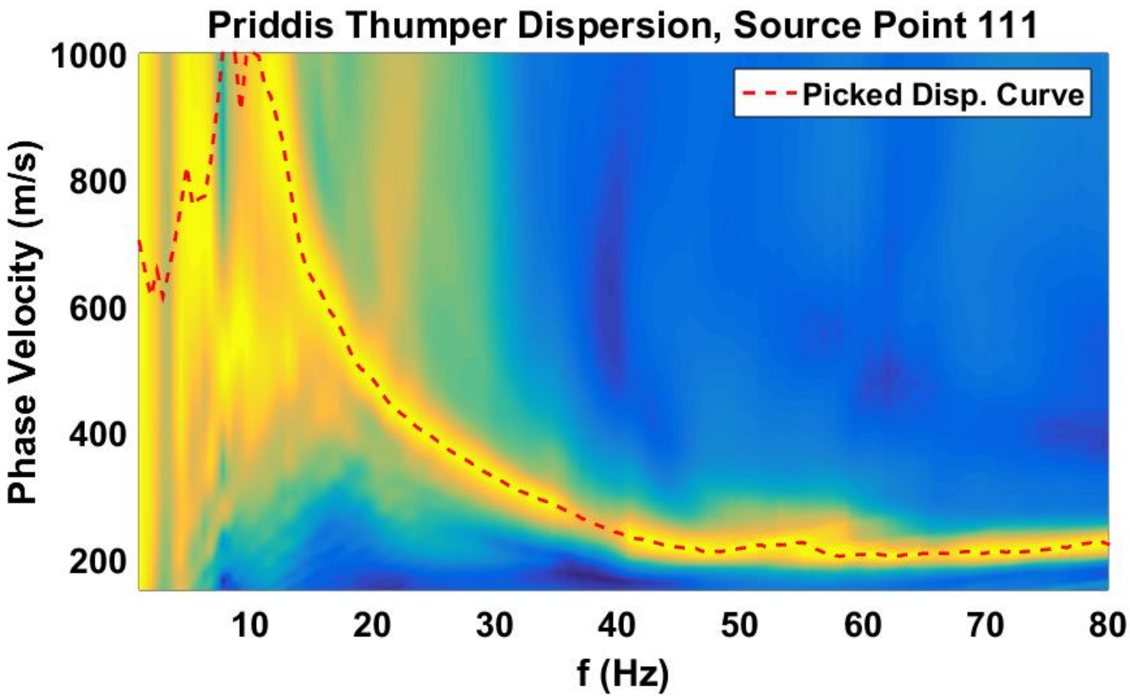

Figure 5-20 Dispersion spectra after processing. Picks below 11 Hz are erroneous.

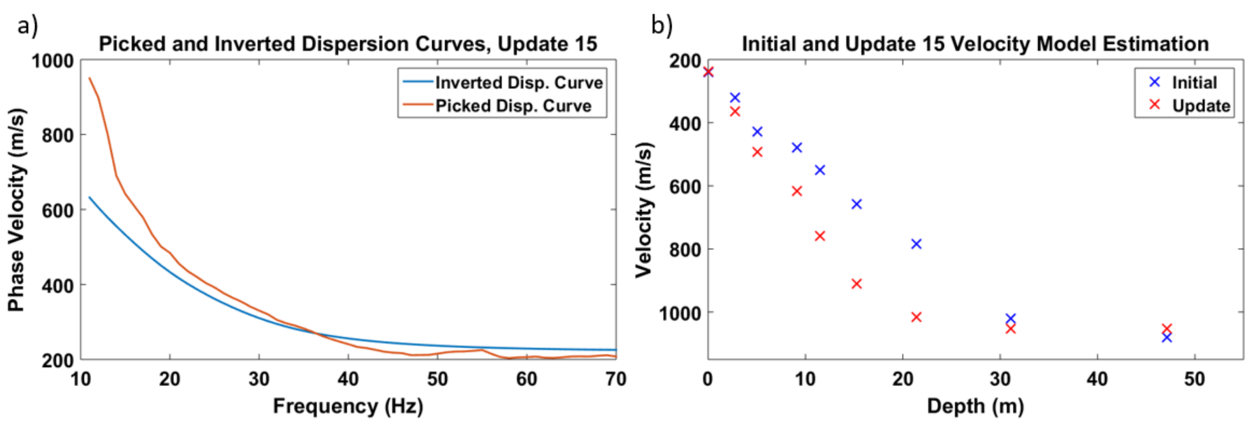

Figure 5-21 Inversion results for source point 111. a) Dispersion curve comparison. b) Shear wave velocity model.

5.3.5 Source point 102

Source point 102 is the Southern-most point on the survey line, adjacent to the vertical well at the research site. The stacked and interpolated shot record is shown in Figure 5-22. Again, at offsets greater than ~100 m, dispersion energy is incoherent. The dispersion spectra with picked fundamental mode curve is shown in Figure 5-23. The inversion results in Figure 5-24 are very similar to the results at other source points, again indicating a base of near surface or top bedrock at around 20 m depth.

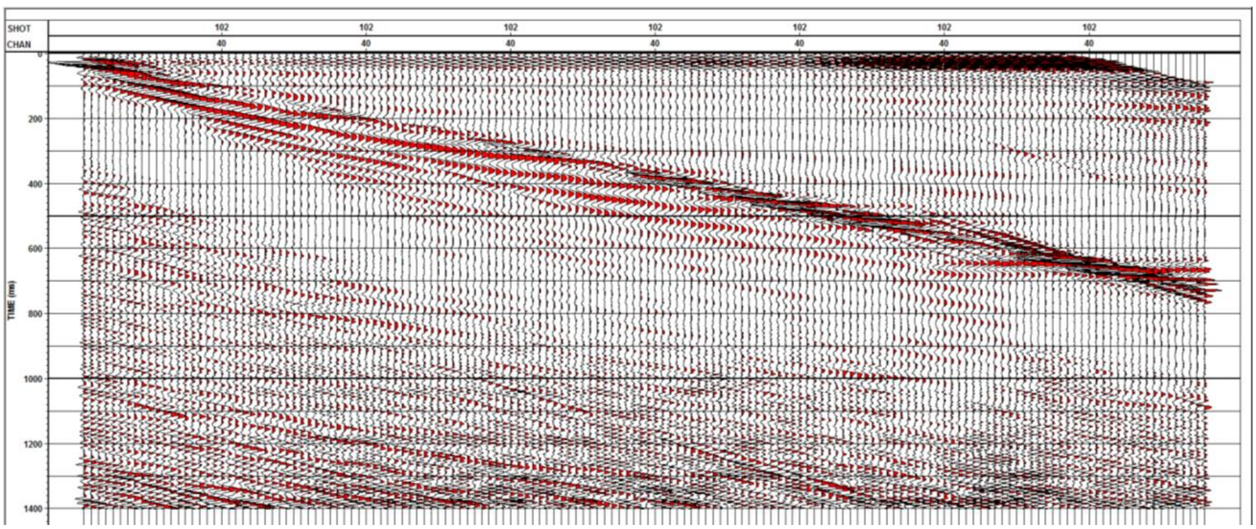

Figure 5-22 Source point 102 data interpolated to 1.25m receiver spacing. AGC applied. Generated in Vista.

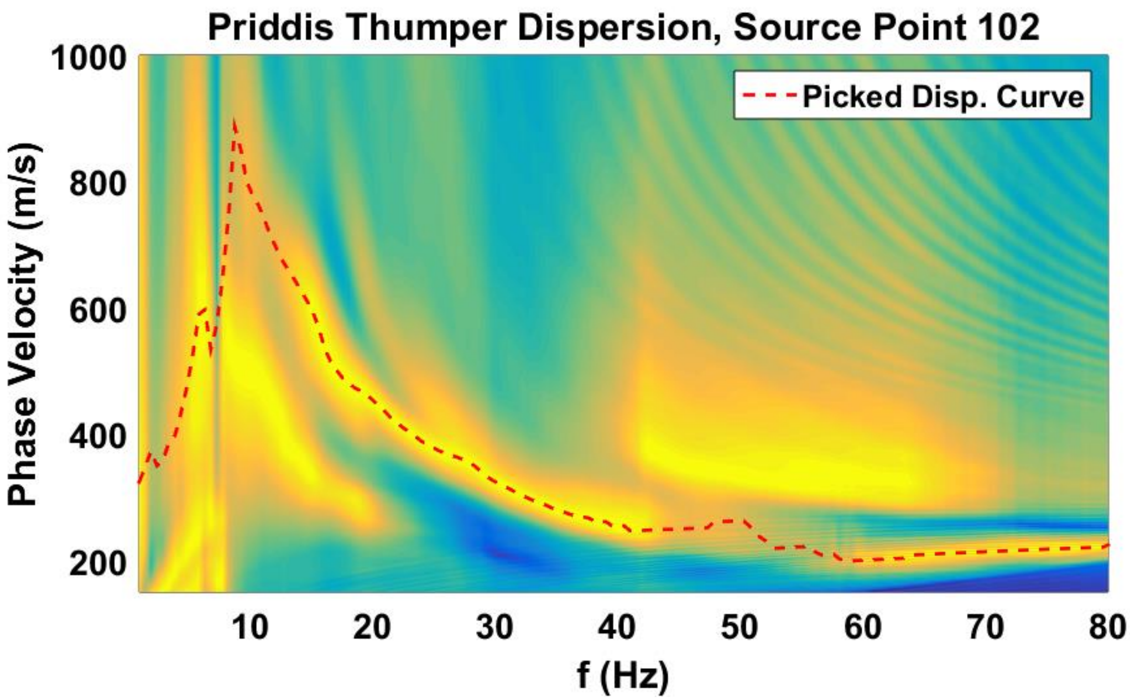

Figure 5-23 Dispersion spectra after processing. Picks below 10 Hz are erroneous.

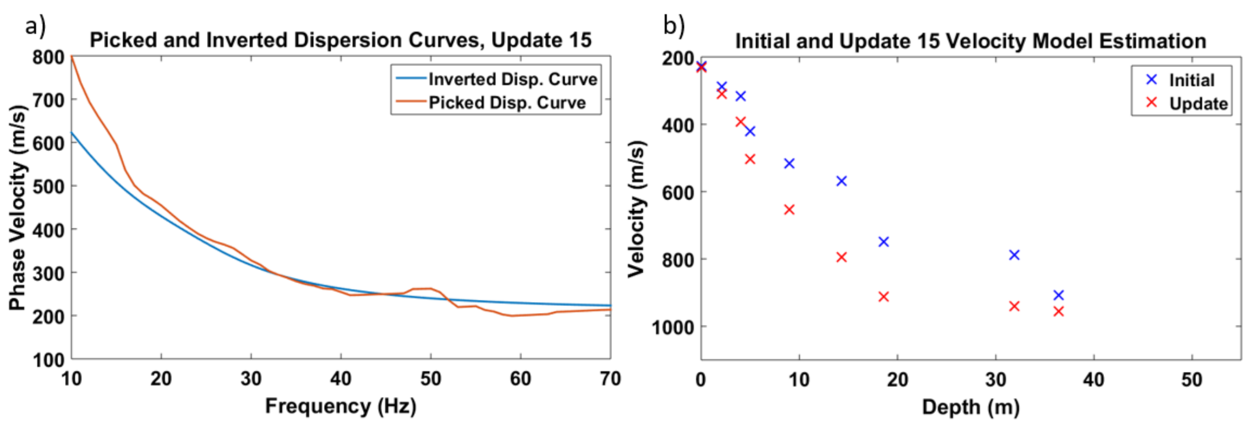

Figure 5-24 Inversion results for source point 102. a) Dispersion curve comparison. b) Shear wave velocity model.

5.4 2D velocity profile

Using the 1D velocity profiles generated at each source point, a 2D shear wave velocity profile can be built over the survey line. Inverted velocity values and depths are used as point velocities, and bilinear interpolation, linear interpolation in both depth and offset, is used to infill velocities between measurements. The 1D profiles are placed 15 m ahead of the source point they were generated from, to be more representative of the geology being sampled by each shot (Figure 5-25). The 15 m at each end of the survey line is extrapolated from the nearest 1D profile. The 2D shear wave velocity profile is shown in Figure 5-26, and a zoomed image showing the near surface above the bedrock is in Figure 5-27.

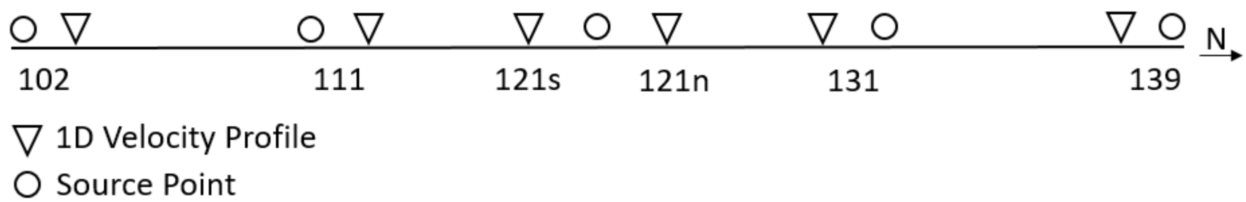

Figure 5-25 Survey geometry, with 1D velocity profile location. Source points and their associated 1D profile locations numbered.

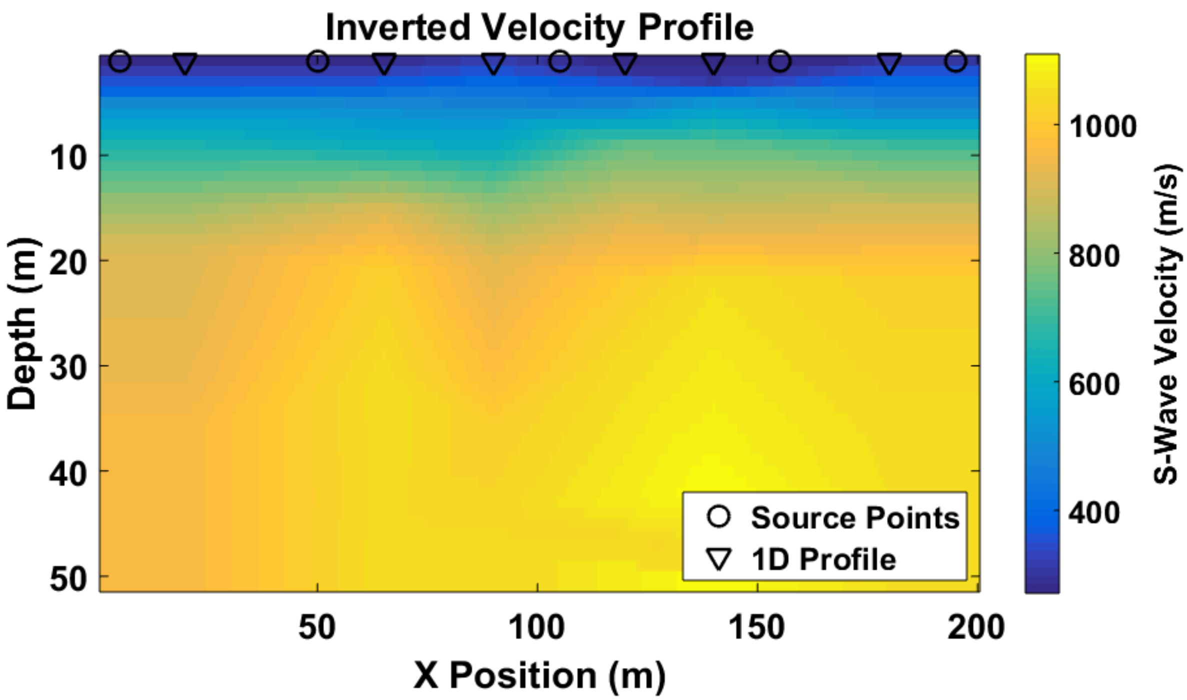

Figure 5-26 Inverted shear wave velocity profile, with source and 1D profile locations.

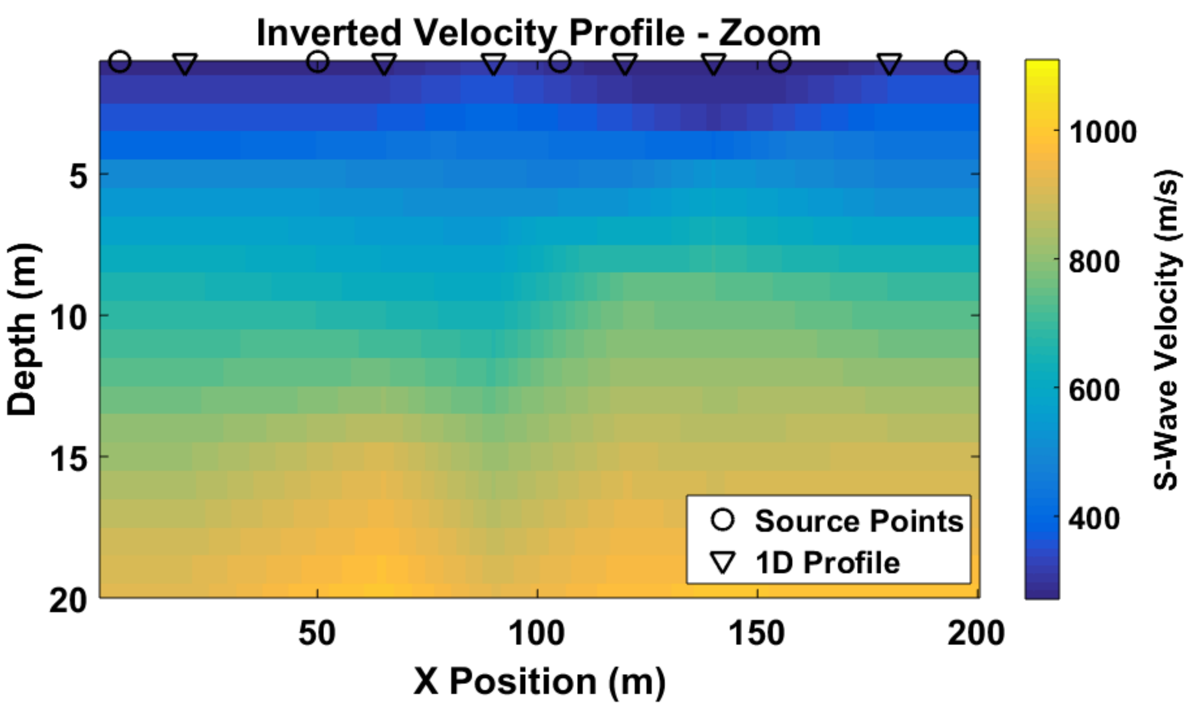

Figure 5-27 Unconsolidated near surface zoom of the above profile.

The above velocity profile shows very low shear velocities from 0 to 10 m, an increase in Vs from 10 to 20 m, and high velocities characteristic of bedrock below 20 m depth. This is reasonable for the study area, and is supported by cuttings from a shallow well on the same site (Dulaijan, 2008). The lithology from this well is displayed in Figure 5-28. At greater than 30 m depth, P-sonic logs from this well have an average velocity of 2600 m/s. With a Vp/Vs of 2.6, which is reasonable for sandstones (Rider and Kennedy, 2011), these velocities are consistent with the inverted Vs of ~1000 m/s at these depths.

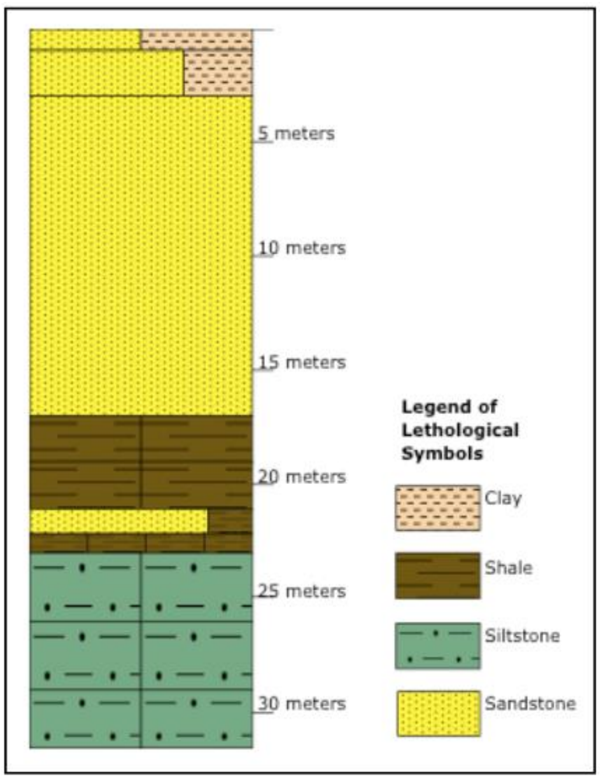

Figure 5-28 Lithology log from a shallow Priddis well. From Dulaijan, 2008.

5.5 Conclusion

In this chapter, MASW techniques were applied to a field data set acquired with non-ideal acquisition parameters to produce near surface shear wave velocity profiles. Shot records from the same source location were stacked, interpolated to 1.25 m receiver spacing, FK filtered, and inverted for 1D Vs profiles. These profiles were then interpolated in both depth and the offset direction to produce a 2D velocity profile over the survey line. This validates the effectiveness of the developed method on field data, and on data with non-ideal sampling.

Chapter Six: Case Study 2 – Hussar Low Frequency Experiment

6.1 Introduction

Now that MASW techniques have been successfully applied to field seismic data sampled at a greater than ideal interval, the methods developed will be tested on exploration scale seismic data. In 2011, CREWES, in collaboration with Geokinetics, INOVA, and Husky Energy, conducted an experiment to study the initiation and recording of low frequency seismic data (Margrave et al., 2011). This survey was conducted with 20 m receiver spacing, on the scale of most exploration seismic surveys. In this chapter, the processing workflow developed in previous sections will be applied to this data, near surface shear wave velocities will be estimated over a portion of this survey line.

6.2 Hussar low frequency experiment

In September 2011, CREWES, INOVA, Geokinetics, and Husky Energy collaborated to plan, design, and conduct a low frequency seismic experiment, to extend the bandwidth of seismic data as far into low frequencies as possible. The objective was to provide low frequency information for inversion methods, including pre-and post-stack inversion, and full-waveform inversion, from seismic data, rather than from sparsely located well logs. The survey was conducted on Husky operated land, located approximately 100 km East of Calgary.

Four sources were used at each source point in the survey. Dynamite charges (2 kg) were used, due to its propensity to radiate energy at all frequencies. Two Vibroseis sources were used; a specially designed low-frequency INOVA vibrator, using a low-dwell sweep (shown in Figure 6-1), and linear sweep, and a standard vibrator with a low-dwell sweep. In the low-dwell sweeps, a longer time is spent oscillating below 8 Hz, at reduced power (amplitude). A longer time is spent at these frequencies to compensate for the reduced power, which is necessary to protect the physical integrity of the Vibroseis truck. The INOVA low-dwell vibrator source is the source which will be used in this study. Source points are every 20 m, collocated with receiver points.

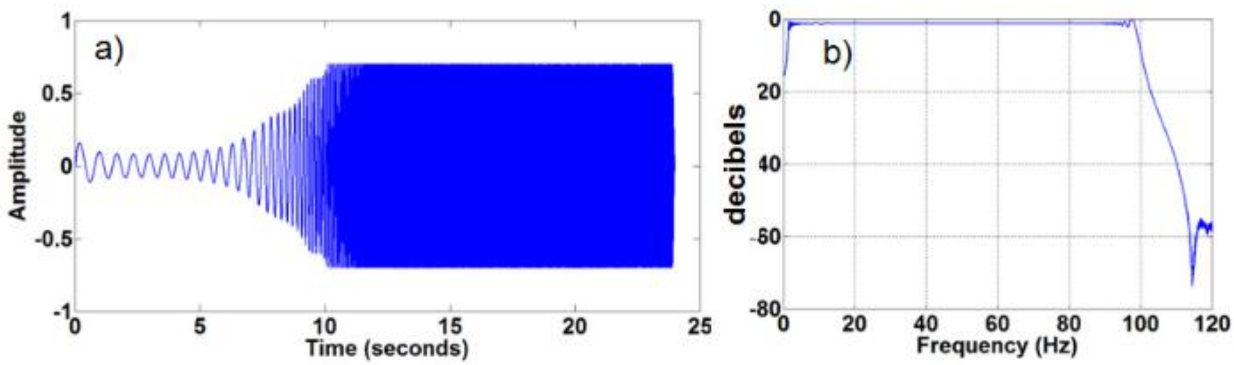

Figure 6-1 Low-dwell sweep designed for the INVOA low-frequency vibrator. a) The sweep in the time domain, showing reduced amplitude (and thus power) at times below 10 seconds. b) Amplitude spectrum of the sweep in a), With a flat response from 1-100 Hz. Adapted from Margrave et al., 2011.

Four receiver lines, spaced 1 m apart and equipped with different receivers, were used in the survey. Line 1 had 3C accelerometers, spaced at 10 m. Line 2 had 3C 10 Hz geophones, spaced at 10 m. Line 3 had 1C 4.5 Hz geophones, spaced at 20 m, Line 4 had a mixture of sensors, mainly broadband seismometers, spaced at 200 m, and high sensitivity 1C geophones spaced at 20 m around one of the wells. The data acquired on line 3, from the 4.5 Hz geophones at 20 m intervals, will be used for this study, due to the lower frequencies recorded from these sensors.

Five wells are located on or near the survey line, however none of them are logged in the near surface, which would allow confirmation of inverted shear velocities. The field layout is shown in Figure 6-2. The survey line is in blue, and the 1 km line over which the velocity profile will be estimated is in red. This line is bounded by source point 387 in the SW, and source point

287 in the NE. In the SW, the line crosses a flat farmer's field, and crosses into wild bluffs to the NE. The elevation profile of the survey and profile line is shown in Figure 6-3.

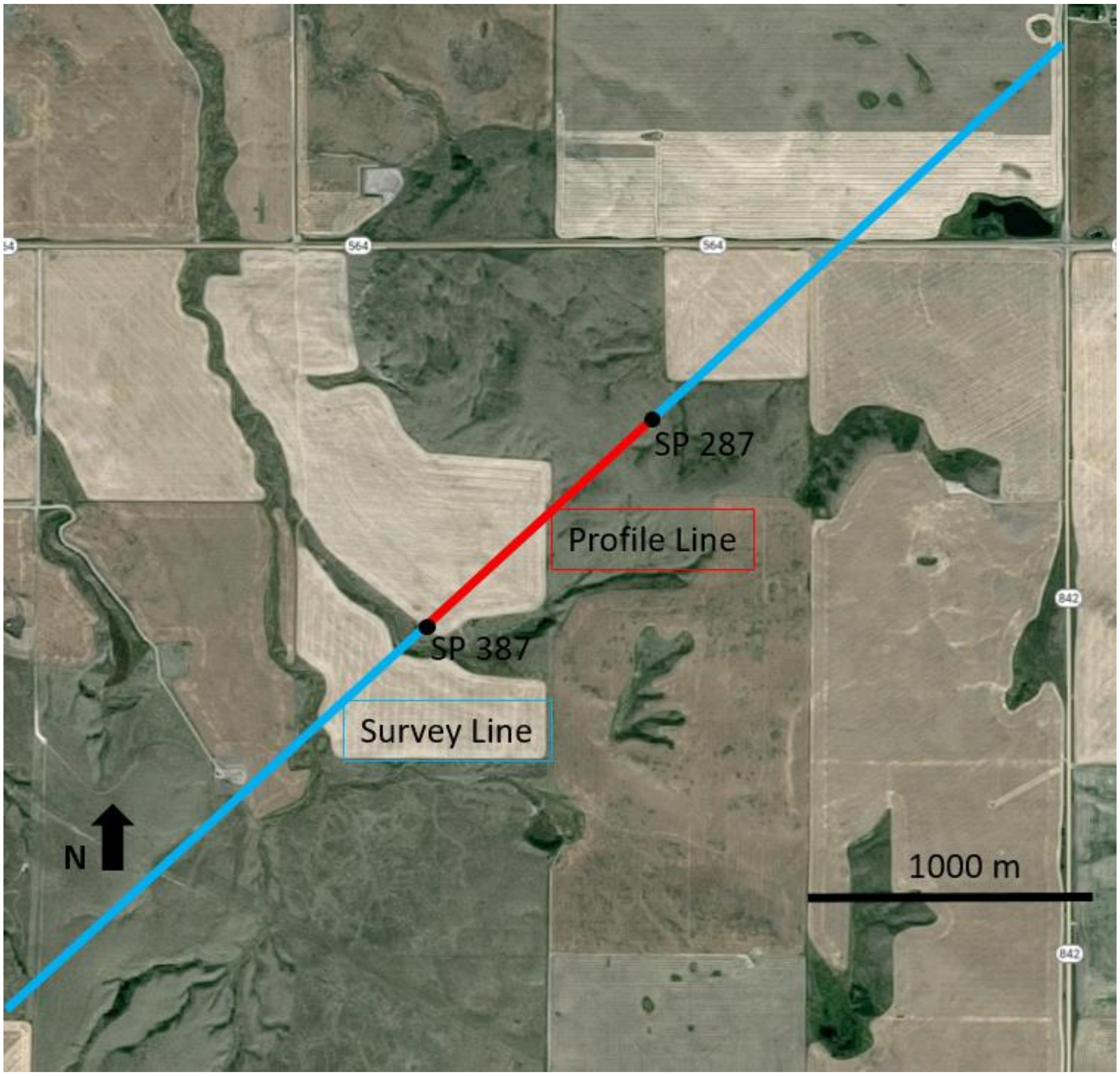

Figure 6-2 Field location map, showing the survey line, velocity profile line, and profile line end source points for the velocity inversion.

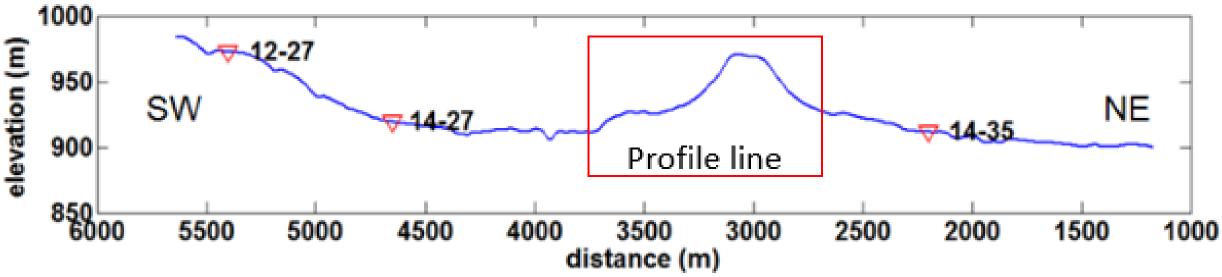

Figure 6-3 Elevation profile of the survey line, with the velocity profile location outlined.

As a test, the dispersion spectrum of a raw shot record can be generated. This is shown in Figure 6-4. Almost no dispersion is resolvable, except a curve visible at the lower left corner of this plot. This could be manually picked, but it is unclear what is causing this curve.

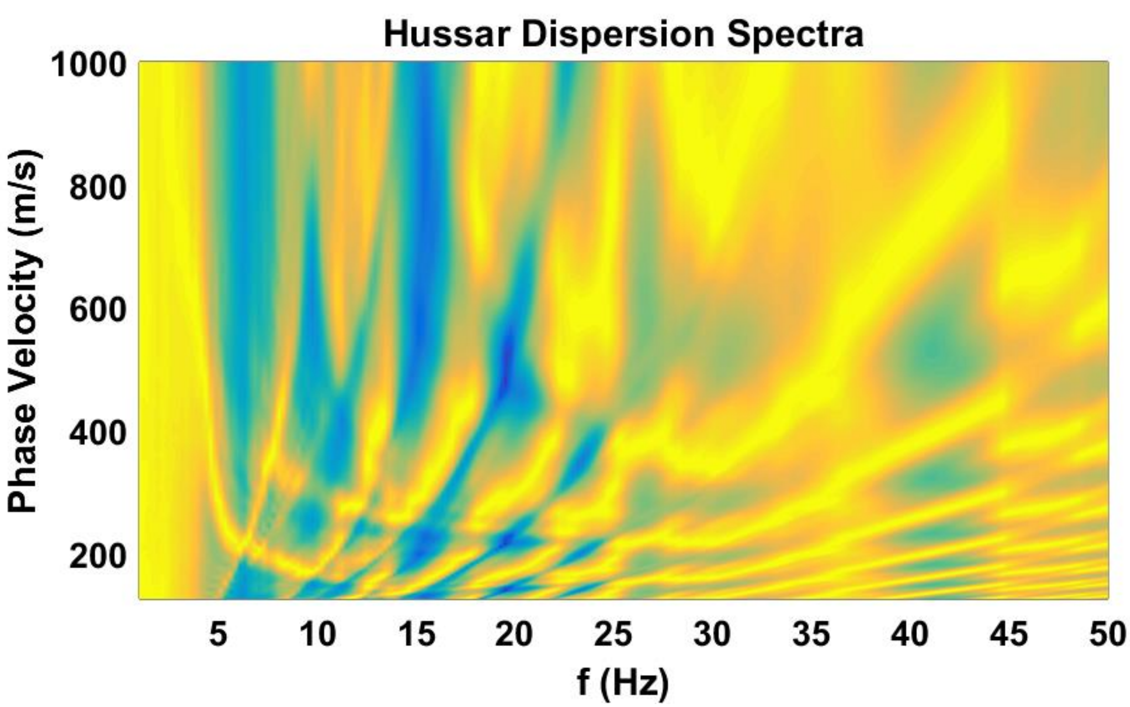

Figure 6-4 Dispersion spectrum generated from a raw Hussar shot record. Fundamental mode dispersion curve is slightly visible in the lower left corner.

6.3 Data processing, dispersion analysis, and velocity inversion

While the survey line is 4.5 km long, only a 1 km portion of the line will be analyzed, processed, and used for building the velocity profile. This portion of the line was selected because of good data quality, and that it traverses varied terrain. 11 shot points in total will be used to build the velocity profile. Offsets for each shot record will be limited to 200 m, to limit the far offset effects observed in the Priddis analysis. The traces nearest the source are muted due to being excessively noisy, leaving the shot record with offsets from 40-200 m. Every fifth source point, each 100 m apart, will be used to generate a 1D Vs profile representative of the subsurface geology adjacent to that source point.

The processing workflow followed is similar to those followed in previous sections. For this profile inversion, only positive offsets (towards the NE) are considered, thus the shot records are muted outside the positive 40-200 m range. Then the record is LNMO corrected, flattening the ground roll, centered around the dominant amplitudes. The record is then interpolated from 20 m to 2.5 m receiver spacing, and the LNMO correction is reversed. FK filtering was found to have marginal effect on this data set, so this step is not included in this workflow.

Dispersion curves, shown in Figure 6-5, can be extracted from the shot records, and used to invert for 1D shear wave velocity profiles. The variation in dispersion spectra quality and resolution is clear. This is likely mainly due to variation in interpolation quality in the case of each individual shot record. In the dispersion spectra for source points 297-317, to the NE side of the line, there appears to be curve “ghosting” where there is potential for two unique curves to be picked. This indicates lateral variation in velocities sampled by the surface waves. In these cases, the highest amplitude events on the spectra are picked.

Several of these dispersion curves peak at 300-400 m/s, indicating lower maximum velocity, especially towards the SW end of the line. In the spectra for source points 307 and 297, the picked curve is not smooth, and has irregular jumps in velocity. This is due to the limited resolution of some of these plots. During the inversion, the estimated dispersion curve will match the average of these irregular curves, seen in Figure 6-6. Initial layer velocities, and layer depths will be reflective of these variations, if picked from points not along the trend of the curve. In these cases, the velocity will be corrected during the inversion, however, the depths will not be altered. This could lead to some erroneous depth estimates in profiles generated from these curves. One such case is source point 387, where three depth-velocity points are predicted around 10 m depth, with different velocities (in Figure 6-7). The velocities are within 30 m/s, so will not greatly affect the 2D velocity profile.

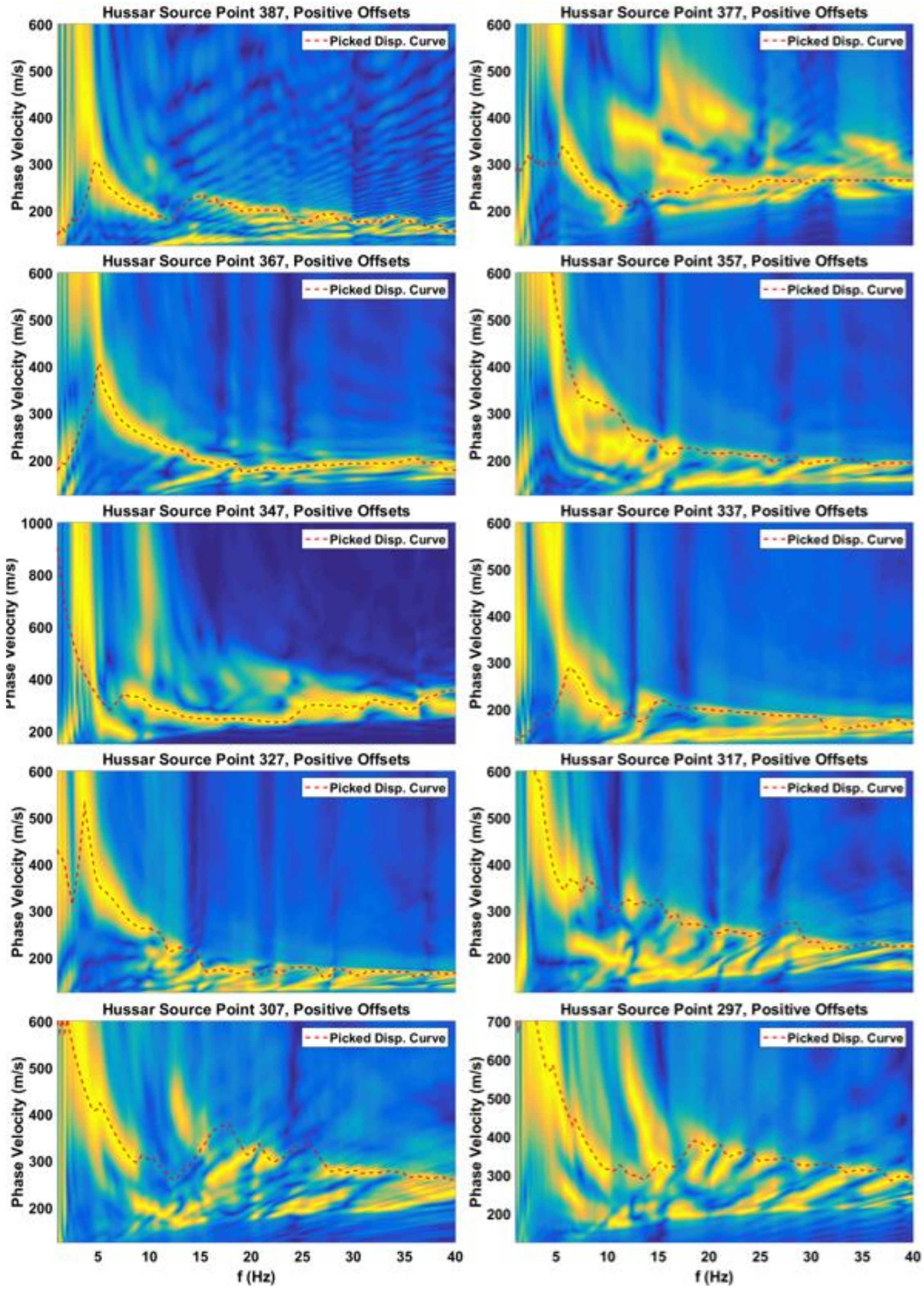

Figure 6-5 Picked dispersion curves for 10 of the shot records used.

The low frequency cut-off point for most of the source points is 5 Hz, below which the curve trends vertically, or is unresolvable, but varies from 4-6 Hz. When limited to frequencies above 6 Hz, velocities at greater depths are not predicted, which is reflected in higher numbered source points to the SW. At source points to the NE, the dispersion curve is smoother, higher velocity, and traceable to lower frequencies than in the SW. This, along with lower peak velocity in the SW, suggests that velocities increase to the NE. This is also where the profile line is sampling the wild bluffs, sitting above the farmer's field. It is reasonable to presume that the bluffs sitting higher in elevation than the field could be composed of different materials.

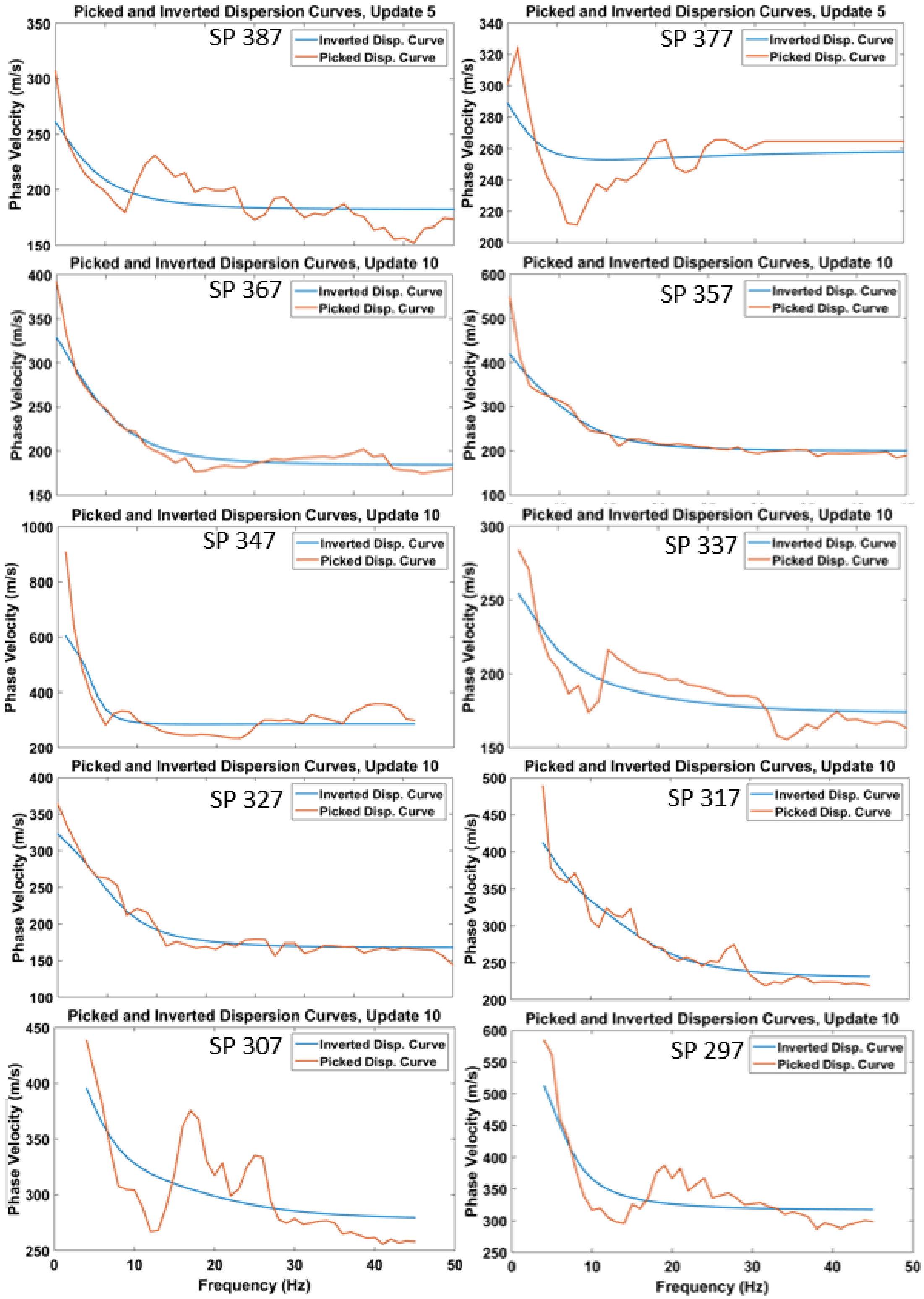

Figure 6-6 Picked and inverted dispersion curves for source points 297-387.

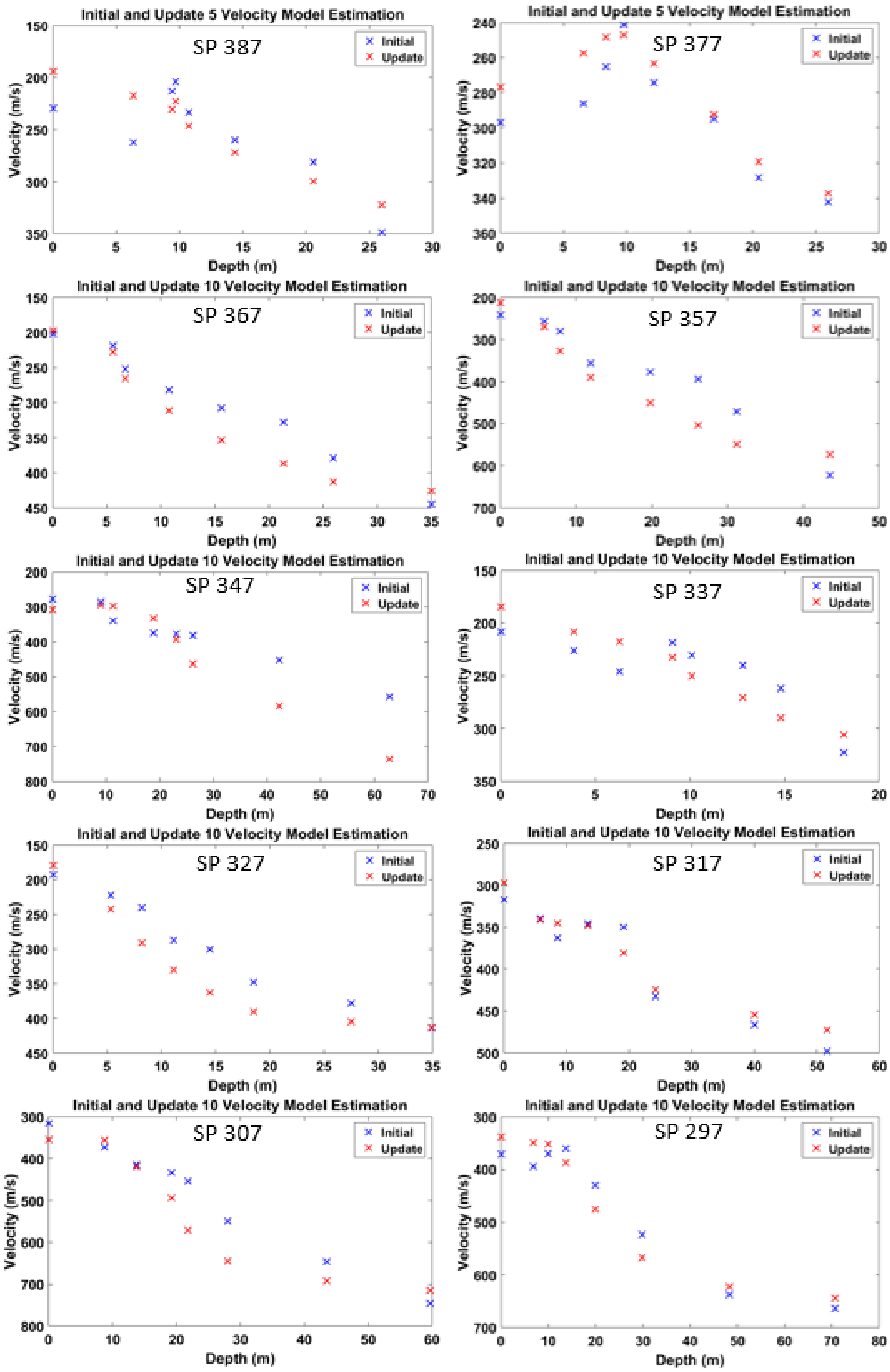

Figure 6-7 Initial and inverted 1D velocity models for source points 297-387.

Since the source points are evenly spaced at 100 m, and are sampling the near surface for just 200 m laterally from them, the 1D profiles will be placed at 100 m offset from their source point. They will be located at the adjacent source point. Proceeding with the bilinear interpolation used previously, a 2D velocity profile is calculated, shown in Figure 6-8. This profile shows a bedrock depth of approximately 60 m over the central portion of the line, with shallower depths to the NE.

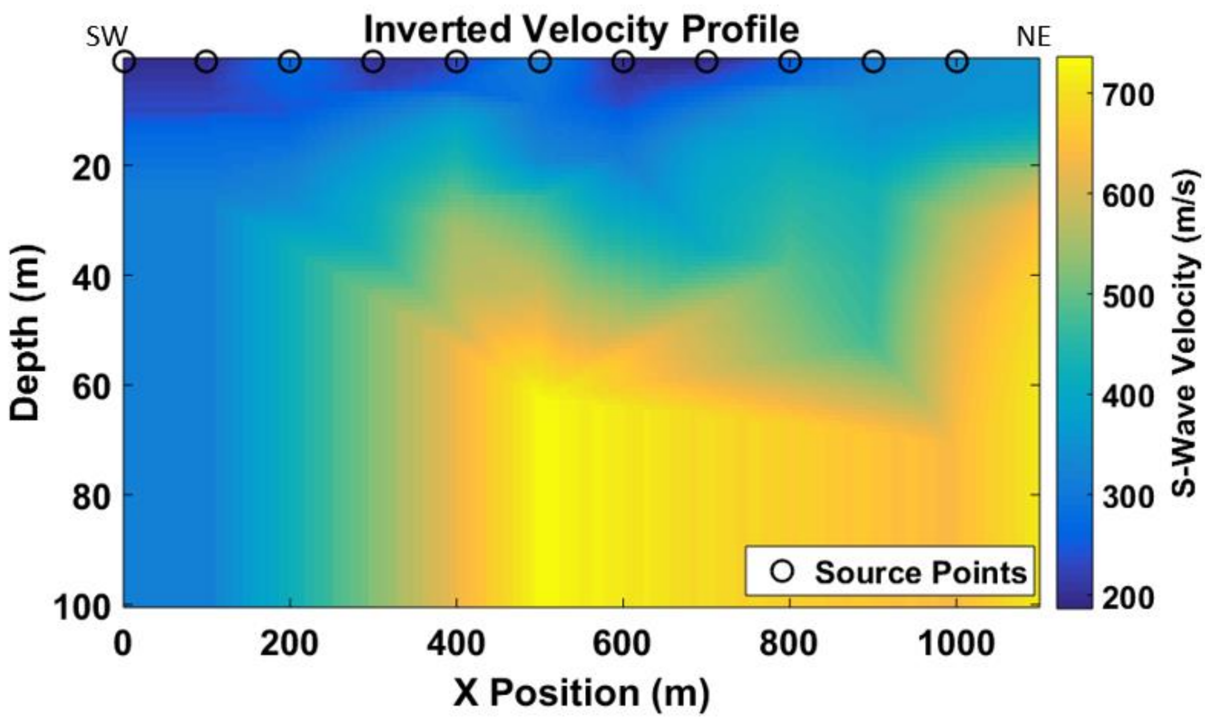

Figure 6-8 Inverted 2D shear wave velocity profile. 1D profiles are placed 100m to the right (NE) of the source point they were generated from. The first 100m are extrapolated from the first source point 1D profile.

6.4 Discussion and conclusions

The Hussar low frequency experiment was a good candidate for application of MASW techniques due to the low frequency sources and receivers used. The 4.5 Hz geophones are the same as what would be used in a near surface MASW study, and the low frequency vibrator source allows generation of low frequency ground roll. While the survey line was 4.5 km long, offsets of the shot records were limited to 40-200 m, due to far offset body wave interference and near offset source noise. The remaining traces were interpolated to 2.5 m receiver spacing, from which dispersion curves could be generated. The resolution of these curves is poor compared to curves generated from data with better sampling, however, they are clear enough to pick the fundamental mode of dispersion, or the trend of the curve at the very least. More densely sampled data would allow for more accurate velocity profile inversions; however, it is not always available.

In this chapter, following the processing steps developed in earlier chapters, primarily interpolation, MASW techniques were successfully applied to field data sampled with 20 m receiver spacing. This experiment has shown that with interpolation and selective muting, near surface velocity profiles can be estimated from exploration scale reflection seismic data.

Chapter Seven: Conclusions

7.1 Conclusions

The near surface of the Earth is typically composed of unconsolidated, poorly sorted mixtures of rock types, with different properties that affect the propagation of seismic energy. Since both source and receiver are placed above or within this layer, all recorded seismic energy has propagated through this layer, and has been influenced by its properties. Recorded seismic reflections have travelled through this layer at least twice, typically at different locations with unique near surface properties, and so can have been greatly affected. These effects generally manifest as travel time delays at receivers located over a slower or thicker near surface. Ground roll, the recorded surface waves, have travelled solely through the near surface layers, so will contain information about their properties in its amplitudes.

Multichannel analysis of surface waves (MASW) techniques have been developed and utilized for nearly two decades, to characterize the near surface from specifically designed surveys. This method exploits the dispersive nature of surface waves to estimate near surface shear wave velocities. Ground roll signals, which are filtered and discarded from reflection surveys, are interrogated for the information they can contain about the near surface. Applications have primarily been in geotechnical studies; however, potential exists for MASW use in exploration seismic surveying and processing. The work in this thesis has applied MASW techniques to synthetic and field data sets with parameters that differ from a typical MASW survey in purpose, equipment used, and the layout and survey design.

Should near-surface studies be desired from data acquired during exploration seismic surveys, especially FWI applications, some considerations of survey parameters should be made during the design phase. First, receivers should be single channel, as receiver groups would attenuate some ground roll energy. Where possible, low frequency (4.5 Hz) geophones should be used, so that low frequencies may be recorded, increasing the depth of investigation of surface wave analysis. Low frequencies should also be generated by the source, so low frequency vibrators, or dynamite should be used in these cases.

In Chapter 2, I reviewed the state-of-the-art in near surface characterization methods, outlining the process of MASW, and the theory behind the steps within. This included dispersion curves and their generation, as well as limitations to the MASW method. The theory behind the processing flow used in later chapters was discussed, including LNMO corrections, interpolation, and FK filtering.

In Chapter 3, I introduced the forward modelling methods used, including the building of geological velocity models, and finite-difference modelling of wavefield propagation through them. An inversion workflow and method were presented, which utilized least-squares inversion to invert for a shear wave velocity model from the extracted dispersion curves. Modelling error was discussed, and illustrated with a simple two-layer model example. Modelling error must be taken into consideration in all inversion results, since it is impossible to produce exactly the same dispersion curve in the inversion, given the same model parameters, as one extracted from field or synthetic data.

In Chapter 4, the developed shear wave velocity inversion is tested on synthetic datasets. A horizontally layered, laterally homogeneous model proves the inversion is accurate for 1D cases. A laterally heterogeneous model inversion extends this success to two dimensions, allowing accurate estimation of shear velocities in geological conditions. The processing workflow was tested on a synthetic dataset, and proven to improve the resolution of dispersion curves when data are acquired with larger than ideal (>2m) receiver spacing.

In Chapter 5, I applied the processing workflow and velocity inversion to the Priddis thumper experiment dataset. This data was acquired with 5 m receiver spacing, over a 200 m survey line using a thumper source. Collocated shot records were stacked, interpolated, and FK filtered prior to dispersion curve generation. Near surface shear velocities were then inverted from these curves, and a 2D velocity profile, consistent with shear velocity of well cuttings from a nearby well was generated. This demonstrated the success of the developed methods on field data, and encouraged the application on even more poorly sampled data.

In Chapter 6, I applied the same procedure to the low frequency Hussar experiment dataset. Produced dispersion curves have much lower resolution than those generated from more densely sampled data, but allow for inversion of shallow shear wave velocity profiles. The lower resolution of these curves is due to the original sampling of the data, which is difficult to overcome with basic interpolation methods. These curves are resolved enough to estimate the depth to bedrock beneath the source points.

Bibliography

Bertram, M.B., and Margrave, G.F., 2010, Recovery of low frequency data from 10Hz geophones, CREWES Research Reports, Volume 22.

Bohlen, T., D. De Nil, D. Kohn and Jetschny S., 2016, - SOFI2D - seismic modeling with finite differences 2D - elastic and viscoelastic version. Karlsruhe Institute of Technology, used under GNU General Public License, Free Software Foundation.

Cova, R., 2017, Near-surface S-wave traveltime corrections and inversion: a raypath-consistent and interferometric approach, (PhD thesis), University of Calgary.

Cox, M., 1999, Static corrections for seismic reflection surveys, Geophysical references, No. **9**, Society of Exploration Geophysicists.

Dou, S., Lindsey, N., Wagner, A.M., Daley, T.M., Freifeld, B., Robertson, M., Peterson, J., Ulrich, C., Martin, E.R., and Ajo-Franklin, J.B., 2017, *in* Nature Scientific Reports, **7**, Article 11620.

Dulaijan, K.A., 2008, Near-surface characterization using seismic refraction and surface-wave methods, MSc thesis, University of Calgary.

GEDCO, 2013, 2D trace interpolation, GEDCO Vista program documentation, Version 2013.0.0.

Harrison, C.B, G.F. Margrave, M. Lamoureux, A. Siewart, and Barrett, A., 2011, Harmonic decomposition of a Vibroseis sweep using Gabor analysis, CREWES Research Reports, Volume 23.

Komatitsch, D., & Martin, R., 2007, An unsplit convolutional perfectly matched layer improved at grazing incidence for the seismic wave equation. Geophysics, **72**, No. 5, 155-167.

Lawton, D.C., Gallant, E.V., Bertram, M.B., Hall, K.W., and Bertram, K.L., 2013, A new S-wave seismic source, CREWES Research Reports, Volume 25.

Levander, A.R., 1988, Fourth-order finite-difference P-SV seismograms, Geophysics, **53**, No. 11, 1425-1436.

Levenberg, K., 1944, A method for the solution of certain nonlinear problems in least squares, Quarterly of Applied Mathematics, **2**, 512-540.

Li, P., Zhang, K., and Yan, Z., 2016, Near-surface shear-wave velocity estimation based on surface-wave inversion, The Leading Edge, **35**, No. 11, 940-945.

Lines, L.R., and Treitel, S., 1984, Tutorial: A review of least-squares inversion and its application to geophysical problems, Geophysical Prospecting, **32**, 159-186.

Long, M., and Donohue, S., 2007, In situ shear wave velocity from multichannel analysis of surface waves (MASW) tests at eight Norwegian research sites, Canadian Geotechnical Journal, **44**, 533-544.

Margrave, G.F., 2006, Methods of Seismic Data Processing, CREWES, Department of Geology and Geophysics, University of Calgary.

Margrave, G.F., Mewhort, L., Phillips, T., Hall, M., Bertram, M.B., Lawton, D.C., Innanen, K., Hall, K.W., and Bertram, K., 2011, The Hussar low-frequency experiment, CREWES research reports, Volume 23.

Mills, A., Cova, R., and Innanen, K., 2016, Surface wave modelling and near surface characterization background, CREWES Research Reports, Volume 28.

Mills, A., and Innanen, K., 2016a, Brute force analysis of residuals arising from the near surface, CREWES Research Reports, Volume 28.

Mills, A., and Innanen, K., 2016b, Processing of ground roll for the study of near-surface Rayleigh wave dispersion, CREWES Research Reports, Volume 28.

Mills, A., Keating, S., Sun, J, and Innanen, K., 2016, The effect of the near surface of internal multiples: a test of 1.5D prediction on synthetic examples, CREWES Research Reports, Volume 28.

Nazarian, S. K.H. Stokoe, and Hudson, W.R., 1983, Use of spectral analysis of surface waves method for determination of moduli and thicknesses of pavement systems, Transportation Res. Record, 930, 38-45.

Park, C.B, Miller, R.D., and Xia, J., 1998, Imaging dispersion curves of surface waves on multi-channel record, *in* 1998 SEG Annual Meeting Expanded Abstracts.

Park, C.B, Miller, R.D., and Xia, J., 1999, Multichannel analysis of surface waves, Geophysics, **64**, No. 3, 800-808.

Park, C.B, Miller, R.D., and Xia, J., 2000, Detection of higher mode surface waves over unconsolidated sediments by the MASW method, *in* Proceedings of the Symposium on the Application of Geophysics to Engineering and Environmental Problems.

Park, C.B., Miller, D.M., and Miura, H., 2002, Optimum field parameters of an MASW survey, SEG-J Expanded Abstracts.

Perez Solano, C.A., D. Donno, and Chauris, H., 2014, Alternative waveform inversion for surface wave analysis in 2-D media, Geophysical Journal International, 198, 1359-1372.

Phillips, C., G. Cascante, and Hutchinson, D.J., 2004, Evaluation of horizontal homogeneity of geomaterials with the distance analysis of surface waves, Canadian Geotechnical Journal, 41, 212-226.

Richart, F.E., J.R. Hall, and Woods, R.D., 1970, Vibrations of soils and foundations, Prentice-Hall, Inc.

Rider, M., and Kennedy, M., 2011, The geological interpretation of well logs, Rier-French Consulting.

Rix, J., and Lai, C.G., 2003, mat_disperse.m Matlab code, used under GNU General Public License, Free Software Foundation.

Sears, T.J., Singh, S.C., and Barton, P.J., 2008, Elastic full waveform inversion of multi-component OBC seismic data, Geophysical Prospecting, **56**, 843-862.

Stokoe II, K.H., Wright, G.W., Bay, J.A., and Roesset, J.M., 1994, Characterization of geotechnical sites by SASW method, *in* Woods, R.D., Ed., Geophysical characterization of sites: Oxford Publishers.

Tarantola, A., 1986, A strategy for nonlinear inversion of seismic reflection data, Geophysics, **51**, 1893-1903.

Turner, G., 1990, Aliasing in the tau-p transform and the removal of spatially aliased coherent noise, Geophysics, **55**, No. 11, 1496-1503.

Udias, A., 1999, Principles of seismology, Cambridge University Press.

Virieux, J., 1986, P-SV wave propagation in heterogeneous media: velocity-stress finite-difference method, Geophysics, **51**, No. 4, 889-901.

Virieux, J., and Operto, S., 2009, An overview of full-waveform inversion in exploration geophysics, Geophysics, **74**, No. 6, WCC1-WCC26.

Xia, J., Miller, R.D., and Park, C.B., 1999, Estimation of near-surface shear-wave velocity by inversion of Rayleigh waves, Geophysics, **64**, 691-700.

Xia, J., Xu, Y., Luo, Y., Miller, R.D., Cakir, R., and Zeng, G., 2012, Advantages of using multichannel analysis of Love waves (MALW) to estimate near-surface shear-wave velocity, Survey in Geophysics, **33**, 841-860, Springer.

Xu, S., Zhang, Y., Pham, D., and Lambaré, G., 2005, Antileakage Fourier transform for seismic data regularization, Geophysics, **70**, No. 4, V87-V95.

Yilmaz, O., 2001, Seismic data analysis: Processing, inversion, and interpretation of seismic data, Volume 1, Society of Exploration Geophysicists.

Yilmaz, O. 2015, Engineering seismology with applications to geotechnical engineering, Society of Exploration Geophysicists.